CYRIC

ANNUAL REPORT

2004

(January 2004 - December 2004)

CYCLOTRON AND RADIOISOTOPE CENTER
TOHOKU UNIVERSITY
http://www.cyric.tohoku.ac.jp/

PREFACE

In this twenty-fifth issue of the CYRIC Annual Report, we summarize the activities in research and development, and in training of radioisotope safe-treatment at the Cyclotron and Radioisotope Center (CYRIC) during the calendar year 2004.

Research at CYRIC was carried out in the fields of nuclear physics, nuclear chemistry, material sciences, nuclear medicine using PET (oncology, brain study, pharmacology), radiopharmaceutical chemistry, health physics, nuclear instrumentation, nuclear medical engineering (diagnosis and therapy technology), nuclear engineering and elemental analysis using PIXE.

Developments and improvements on nuclear instruments and techniques have progressed; the highlights are the construction of high-intensity neutron-beam course and the success of extraction of the negatively charged hydrogen beam, which are combined to extend the research with neutron beams. Also the beam attenuator device and the acceleration of C-O-Ne cocktail beam are introduced for testing semiconductor devices. A total of 2613 hours of beam-time was delivered by the K=110MeV cyclotron for scheduled operation in research work.

[^{18}F]FDG, [^{11}C]methionine, [^{11}C]doxepin, [^{11}C]raclopride, [^{11}C]donepezil and [^{18}O]water were routinely prepared and supplied to clinical PET studies. In October 2004, a clinical PET study using [^{18}F]FRP-170, a new hypoxia imaging agent, was started in vertue of the successful development of an automated synthesis module.

With [^{11}C]donepezil, research programs for Alzheimer's dementia are under way. Beta amyloid imaging will be expected to initiate non-invasive diagnosis of dementia The first patients will be studied before this report is issued. Histamine receptor imaging and dopamine receptor imaging have seen steady-progress this year. Brain imaging of BBB transport of several anti-histamine pharmaceuticals is one example of clinically oriented application of receptor studies. Whole-body oncology studies for cancers not reimbursed by insurance and metabolic imaging for sport science are still going on.

The research program on PIXE analysis has been carried out by using an electrostatic accelerator (4.5 MV Dynamitron) at the Fast Neutron Laboratory (FNL), Graduate School

of Engineering, Tohoku University, under the scientific tie up between CYRIC and FNL. A total of 350 hours beam-time was served to this program.

The training for radioisotope safe-treatment was carried out as usual. In 2004, totally 1122 staff members and students of Tohoku University received the training in three courses: 1) Radioisotopes and radiation generators (623 trainees), 2) X-ray machines and electron microscope (410), and 3) Synchrotron Radiation (89). The number of trainee increased by about ten % than 2003 (1008). The English classes were practiced too for each course, and totally 80 foreign students and scientists attended.

We are most grateful to Tohoku University and to the Ministry of Education, Sports, Culture, Science and Technology for continuous support.

January 2005

Keizo ISHII
Director
Cyclotron and Radioisotope Center, Tohoku University

EDITORS:

Keizo	*ISHII*
Masatoshi	*ITOH*
Mamoru	*BABA*
Ren	*IWATA*
Hiroyuki	*OKAMURA*
Tsutomu	*SHINOZUKA*

WORD PROCESSED BY

Yu-ko YAMASHITA

CONTENTS

I. NUCLEAR PHYSICS

II. NUCLEAR INSTRUMENTATION

III. NUCLEAR ENGINEERING

VI. RADIOCHEMISRTY AND NUCLEAR CHEMISTRY

VII. RADIOPHARMACEUTICAL CHEMISTRY AND BIOLOGY

VIII. NUCLEAR MEDICINE

IX. RADIATION PROTECTION AND TRAINING OF SAFETY HANDLING

I. NUCLEAR PHYSICS

I. 1. $^{13}C(\alpha, n)^{16}O$ Reaction at E_α = 50 MeV

Orihara H., Hirasaki S.[*], Miura K., Terakawa A.*[**], Ishii K.*[**], and Jon G. C.*[***]

Department of Electronics, Tohoku Institute of Technology
[*]Cyclotron and Radioisotope Center, Tohoku University
[**]Department of Quantum Science and Energy Engineering, Tohoku University
[***]Institute of Physics, Academia Sinica Nankang Taipei

Much attention is concentrated on the experimental studies for nuclear structure of ^{16}O. Among them, single- and multi-nucleon transfer reactions have been extensively investigated in order to make clear one particle one hole 1p-1h, 2p-2h, 3p-3h and cluster structures of this closed shell nucleus. The recent interest on the $^{13}C(\alpha, n)^{16}O$ reaction is related to the topics of nucleo synthesis in the universe. The $^{13}C(\alpha, n)^{16}O$ reaction is one of the main source reaction for the slow-process. Because of very low energy property of this story, The reaction might be influenced by the sub-threshold state at 6.356 MeV, which is only 2-keV below the α–threshold in ^{17}O. Since the resonance strength is proportional to the α-width of the sub-threshold state, the spectroscopic factor of α–transfer reaction e.g. $^{13}C(^6Li, d)^{17}O$ (6.356 MeV) has been studied[1].

In this report, experimental results of the $^{13}C(\alpha, n)^{16}O$ reaction carried out at E_α = 50 MeV by utilizing the fast neutron time of flight method. Measured q-dependency of differential cross sections is compared with finite-range DWBA predictions, where neutron knock-out process is dominant for transitions leading to low-lying state in ^{16}O, while ^3He pick-up process dominates for those to high-lying states in E_x~20MeV. By comparing the present $^{13}C(\alpha, n)^{16}O$ spectrum with those for$^{15}N(d, n)^{16}O$[Ref. 2], $^{14}N((\alpha, d)^{16}O$[Ref. 3], $^{12}C(^6Li, d)^{16}O$[1], $^{13}C(^6Li, t)^{16}O$[4] reactions, many-particle many-hole characters of the individual state are discussed.

The experiments were performed using a 50-MeV α-beam from the K=50 MeV AVF cyclotron at Cyclotron and Radioisotope Center (CYRIC), Tohoku University. Neutron energies were measured by the time of flight technique. Twelve neutron detectors containing totally 23 litter of liquid-scintillator NE213 were set at a flight path of 44 m from

the target, where the effective neutron detection solid angle was 0.23 msr. Angular distributions of neutrons were measured using a beam-swinger system. Detector efficiency for the most energetic neutrons was 3%, which was determined by the ^{7}Li(p, n)^{7}Be reaction through activation analysis. Details of the CYRIC TOF facility have been described elsewhere[5,6]. Metallic carbon enriched to 99% in ^{13}C with the thickness of 2.42 mg/cm^2 was used as the target. Overall energy resolution was 200 keV (FWHM) for the most energetic neutrons leading to the low-lying states in the residual nuclei. The target was prepared by the thermo-clacking of enriched acetylene gas on the tantrum plate heated to 1800°C in a 2.612x10^3 Pa atmosphere. The amount of the tantrum impurity was tested by the PIXE-method to be less than 0.08 μg/cm^2. Gamma-ray events have been rejected by pulse-shape-discrimination technique. Errors in the absolute magnitudes of cross section are estimated to be less than 12%, the dominant part of which is due to the uncertainty of the detector efficiency.

Figure 1 shows a neutron excitation energy spectrum taken at a laboratory angle of 40 degree for the^{13}C(α, n)^{16}O reaction. Due to angular momentum miss matching between entrance-alpha and exit-neutron channels, ground state transition is highly inhibited. A spectrum for the ^{12}C(^{6}Li, d)^{16}O reaction[1], which may exhibit typical α-transfer nature with ΔT=0, are also shown in Fig. 2 for comparison. Alpha transfer leading to the 0$^+$(0.0), 2$^+$ (6.1 MeV), 4$^+$ (10.35 MeV), and 6$^+$ (14.8 MeV) rotational states is clear in both reactions, though their intensities are less systematic for the case of the present ^{13}C(α, n)^{16}O reaction. The other peculiar feature of the (^{6}Li, d) spectrum is it's structure less aspect in the higher excitation energy region beyond ~16MeV as seen in Fig. 2, while many prominent peaks are observed in the (α, n) spectrum. The latter may be due to excitation of T=1, many-particle many-hole states including high-spin states.

Measured angular distributions of emitted neutrons are shown in Figs. 3 through 11 along with theoretical predictions. Theoretical cross sections have been calculated by the code TWOFNR[7], by which we are able to obtain finite-range form factors and multi-step reaction cross sections. Optical potential parameters for the entrance α-channel have been determined by the elastic scattering measurement on ^{13}C at 50 MeV by Watson et al[8]. Those for neutron are parameter set by Carlson et al[9]. Two kinds of reaction mechanism have been assumed. The first one is knock-on reaction, where the incident α-particle knock-out the target neutron forming 4p-4h states in the residual nucleus. The other one is stripping reaction, where three nucleons in the α-particle is stripped to form 3p-3h states

predominantly in the residual ^{16}O nucleus.

An experimental differential cross section is compared with theoretical one with the code TWOFNR by;

$$(\frac{d\sigma}{d\Omega})_{exp} = \varepsilon C^2 s(\frac{d\sigma}{d\Omega})_{TWOFNR}, \quad C = (T_i T_{iz} \Delta T \Delta T_z \mid T_f T_{fz})$$

,where C is Clebsh-Gordan coefficient for isospin not included in TWOFNR. In the present case, C = 1/2 for T=0 and T=1 of final state isospin. The factor s in the formula is the light particle spectroscopic factor and is 2 for the (a, n) reaction, while ε is the normalization factor introduced to fit theoretical cross sections to the data.

Comparing the present (α, n) data with those by (^{6}Li, d) reaction, we have identified the rotational band. Figures 3, 5 and 6 show q-dependency of differential cross sections exciting the 4p-4h states forming a rotational band consisting of the 0^+, 2^+, and 4^+ states at their excitation energy E_x equal to 0.0, 6.92 and 10.4 MeV, respectively. Curves are theoretical calculations obtained by the $(p_{1/2})^{-4}(sd)^4$ configuration. Theoretical cross sections are normalized to experimental results. An exception of these discussion is excitation of the second excited 3^- state at E_x = 6.13 MeV, which has been observed, for example, by the ^{15}N(d, n)^{16}O reaction as a prominent transition. Note that this state has been observed in the (^{6}Li, d) reaction as seen in Fig. 2. As such, pick-up process should be also taken into accounts in analysis for this transition as illustrated in Fig. 4. The prominent transition, q-dependency for which is illustrated in Fig. 7, has been predicted theoretically by Zuker et al[10]. to be a pure 2p-2h state.

A number of prominent peaks have been observed in higher excitation energy region E_x~20MeV, in contrast to the monotonous aspect of the (^{6}Li, d) spectrum in this region. Angular distributions of the differential cross section for these typical transitions to the 20.6- and 24.7-MeV states are illustrated in Figs. 10-11. In Fig. 10 for the 20.6-MeV transition, two possibilities of 5^+ with ΔL=5, $(p_{1/2})^{-2}(d_{5/2})^2$ configuration and 7^- with ΔL=6 $(p_{1/2})^{-3}(d_{5/2})^3$ configuration are shown for spin-parity assignment. In Fig. 11 for the 24.7-MeV transition, a possibility of 7^- with ΔL=6, $(p_{1/2})^{-3}(d_{5/2})^3$ configuration is shown for spin-parity assignment by the analog relation to the 11.78-MeV (7^-) state in ^{16}N. For these transitions, the normalization factors ε lay in the same order of magnitude.

In a summary, experimental study of the ^{13}C(α, n)^{16}O reaction was carried out at E_α = 50 MeV by utilizing the fast neutron time of flight method. Measured q-dependency of differential cross sections have been compared with finite range DWBA predictions,

where neutron knock-out process is dominant for transitions leading to low-lying state in ^{16}O, while ^{3}He pick-up process dominates for those to high-lying states in E_x~20MeV. By comparing the present $^{13}C(\alpha, n)^{16}O$ spectrum with those for $^{15}N(d, n)^{16}O$, $^{14}N(\alpha, d)^{16}O$, $^{12}C(^{6}Li, d)^{16}O$, $^{13}C(^{6}Li, t)^{16}O$ reactions, many-particle many-hole characters of the individual state were discussed. In particular, a number of 2p-2h and 3p-3h like high-spin states were located at higher excitation energy region.

References

1) Becchetti F. D. et al., Nucl. Phys. **A344** (1980) 336.
2) Kawamura T., PhD thesis Tohoku University (1986).
3) Zisman M. S. et al., Phys. Rev. **C2** (1970) 1271.
4) Kemper K. W. et al., Nucl. Phys. **A405** (1983) 348.
5) Orihara H. and Murakami T., Nucl. Instrum. Methods **181** (1981) 15.
6) Orihara H., et al., Nucl. Instrum. Methods **A257** (1987) 189.
7) Igarashi M., computor code TWOFNR, unpublished.
8) Watson B. A. et al., Phys. Rev. **182** (1969) 977.
9) Carlson J. D., Zafiratos C. D. and Lind D. A., Nucl. Phys. **A249** (1975) 29.
10) Zuker A. P., et al., Phys. Rev. Lett. **21** (1968) 39.

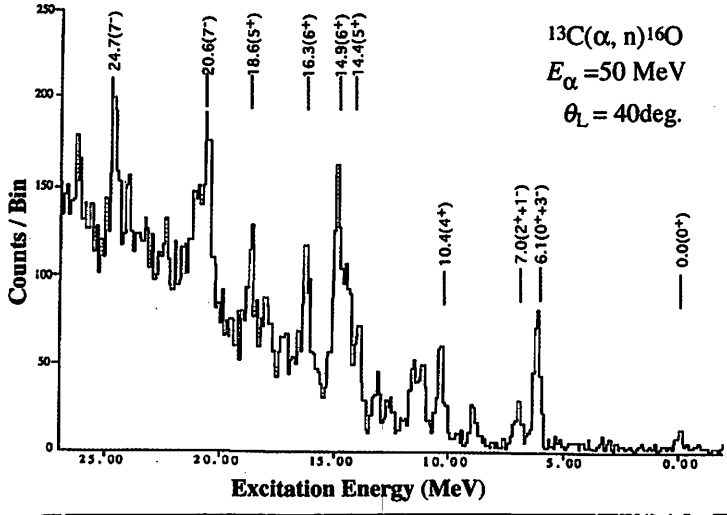

Figure 1. Energy spectrum of the $^{13}C(\alpha, n)^{16}O$ reaction at θ_{lab} = 40° with a flight path of 44.3 m. Energy per channel is 50 keV.

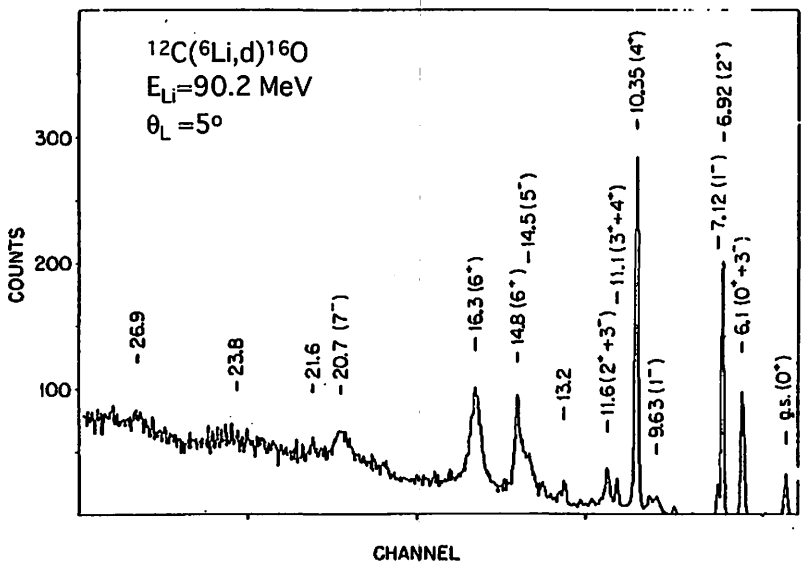

Figure 2. Energy spectrum of the $^{12}C(^{6}Li, d)^{16}O$ reaction at θ_{lab} = 5° by Becchetti et al[1]. Known levels are indicated by E_x (MeV) and J^π values while other groups are indicated by E_x only. Due to limited resolution, the spectrum in a composite of several overlapping spectra.

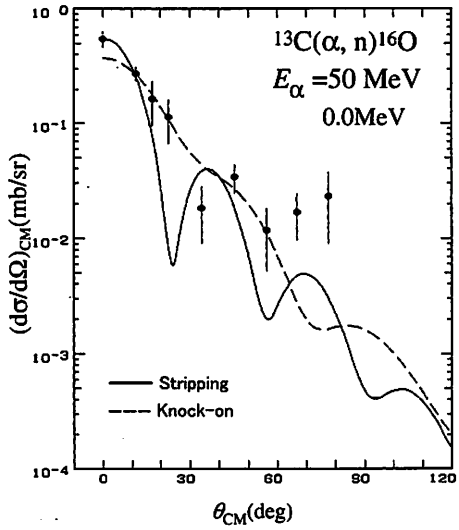

Figure 3. Differential cross sections for neutrons leading to the 0^+ ground state. The curves are theoretical predictions described in the text.

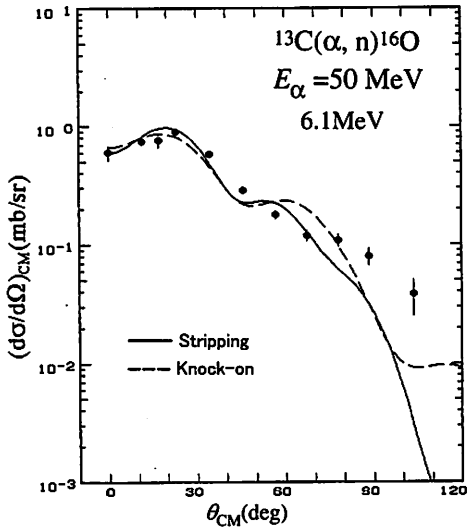

Figure 4. Same as Fig. 3 but for neutrons leading to the 3^-, 6.1-MeV state.

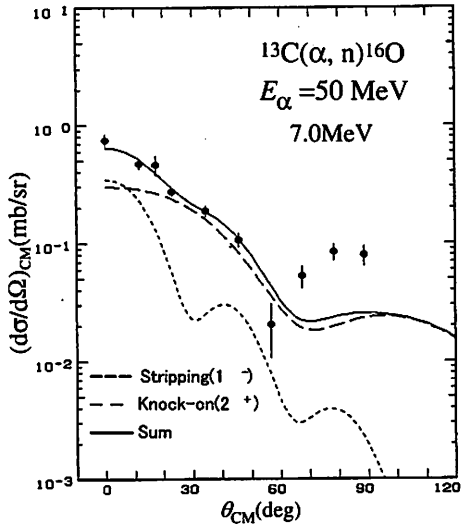

Figure. 5. Same as Fig. 3 but for neutrons leading to the 1^- and 2^+ sates at 7.0 MeV.

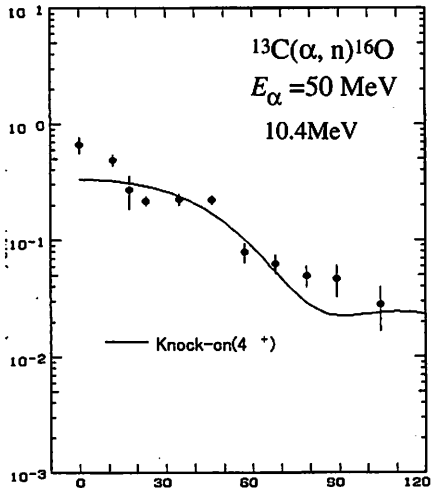

Figure 6. Same as Fig. 3 but for neutrons leading to the 4^+, 10.4-MeV state.

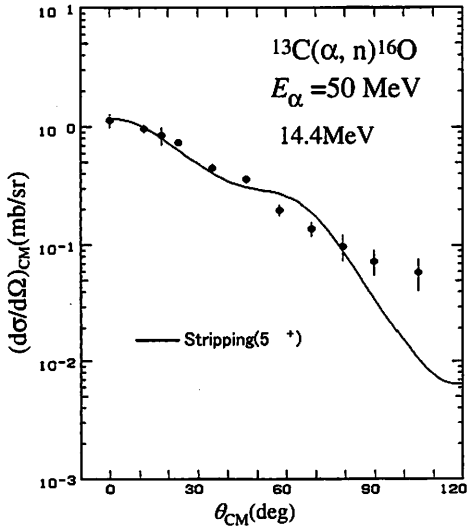

Figure. 7. Same as Fig. 3 but for neutrons leading to the 5^+, 14.4-MeV state.

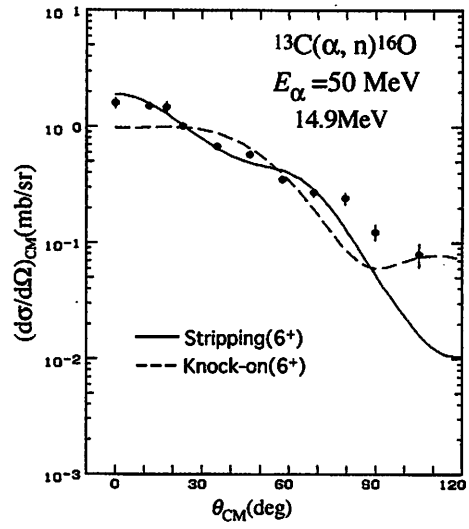

Figure 8. Same as Fig. 3 but for neutrons leading to the 6^+, 14.9-MeV state.

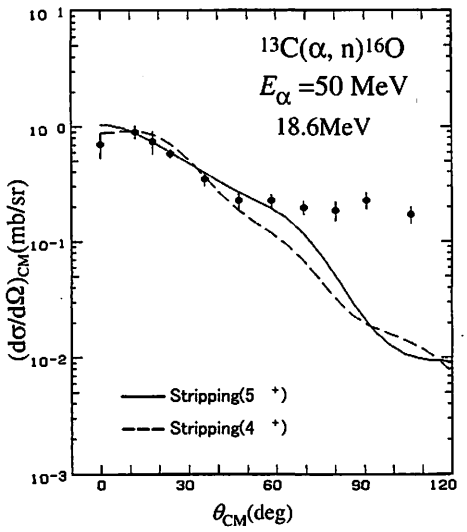

Figure 9. Same as Fig. 3 but for neutrons leading to the 5^+ ,18.6-MeV state.

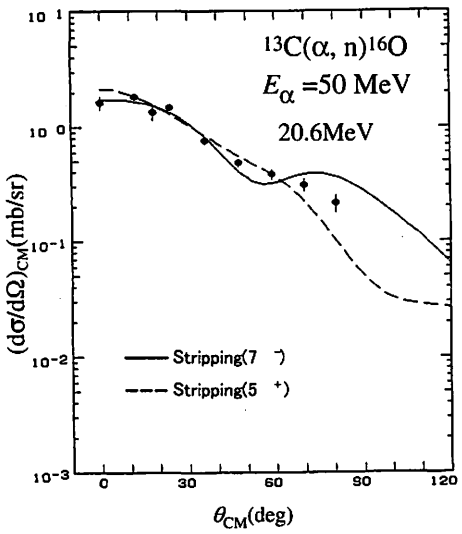

Figure 10. Same as Fig. 3 but for neutrons leading to the $7^-(5^+)$,20.6-MeV state.

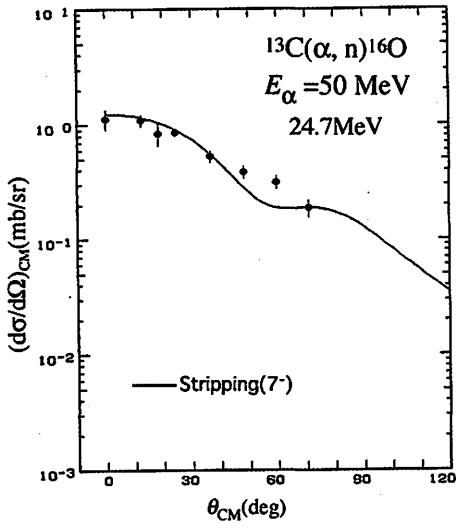

Figure 11. Same as Fig. 3 but for neutrons leading to the 7^-,24.7-MeV state.

I. 2. Gamow-Teller Strengths in the $^{14}N(p,n)^{14}O$ Reaction

Okamura H., Hasegawa T., Terakawa A., Sugimoto N., and Fukushima S.

Cyclotron and Radioisotope Center, Tohoku University

The old and well-known feature of the mass A=14 system is the anomalous hindrance of the transition between the ground state of ^{14}N (J^{π}=1$^+$, T=0) and the ground states of ^{14}O and ^{14}C (J^{π}=0$^+$, T=1). Although the quantum numbers involved would permit a Gamow-Teller decay, the log(ft) values are as large as 9.0 and 7.3 for ^{14}C and ^{14}O, respectively. A number of theoretical descriptions have been proposed, yet failed to explain this suppression satisfactorily. Recently it was suggested that the problem could be resolved if a tensor component of the residual interaction is considered in a large model space[1]. This calculation predicts the main part of the Gamow-Teller strength to be found at higher excitation energies, which, however, has not been established due to the lack of experimental data. Aiming at pursuing this problem, the $^{14}N(p,n)^{14}O$ reaction was measured at E_p=70 MeV and θ_n=0°–60° with small contaminants by using a gas target. Details of the experiment were reported previously. Figure 1 shows the angular distributions of the cross section leading to the 1^+_1 (ground), 2^+_1 (6.59 MeV), and 2^+_2 (7.77 MeV) states of ^{14}O, together with the results of DWBA calculations by using DW81[2] and OXBASH[3] with the conventional MK+CKPOT interaction in the *psdfp* model space. Indeed the transition to the 1^+_1 state is suppressed and dominated by Δl=2, while those to the 2^+_1 and 2^+_2 states are strong and dominated by Δl=0 as predicted. The enhancement factor of summed-2$^+$ strengths, however, is considerably smaller than that of the calculation in ref. 1). Further analysis is in progress.

References

1) Aroua S., Navratil P., Zamick L., Fayache M.S., Barrett B.R., Vary J.P., and Heyde K., Nucl. Phys. **A720** (2003) 71.
2) Program DWBA70, Schaeffer R. and Raynal J. (unpublished); Extended version DW81, Comfort J.R. (unpublished).

3) The shell model code OXBASH, Brown B.A. et al., *NSCL Report* **524** (1984).

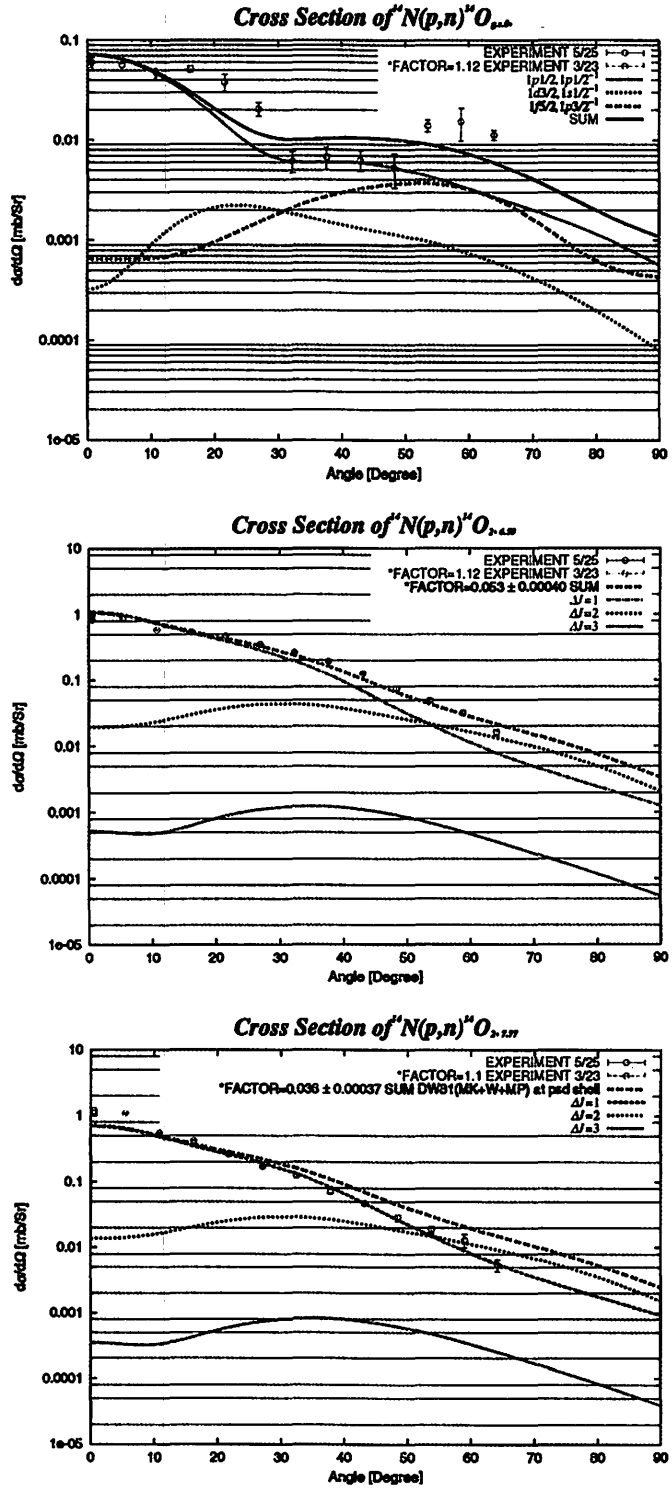

Figure 1. Angular distributions of the cross section for $^{14}N(p,n)^{14}O$ reaction at E_p=70 MeV leading to the 1^+_1 (ground), 2^+_1 (6.59 MeV), and 2^+_2 (7.77 MeV) states, together with the results of DWBA calculations.

I. 3. RI-production Experiment for "Basic Research in Physics" at Physics Department, Tohoku University

Kanda H., Hirose K., Maeda K., Miyase H., Ohtsuki T.[*], *Shinozuka T.*[**], *and Yuki H.*[*]

Physics Department, Graduate School of Science, Tohoku University
[*]*Laboratory of Nuclear Science, Tohoku University*
[**] *Cyclotron and Radioisotope Center, Tohoku University*

A course of "Basic Research in Physics *(Butsurigaku-kiso-kenkyu)*" is opened for third graders at Physics Department in Tohoku University. We carried out the production of radioactive isotopes (RI) at CYRIC, Tohoku University. In general, sealed RI sources were used in the educational experiments in the nuclear or particle physics because of safety and easiness in handling of them. However, there were some anxieties that easiness of their handling mislead students to regard the experiments as "well-made" and boring. By using an accelerator, we can demonstrate "on-going" experiments to the students. From many kinds of simple and educational experiments in the nuclear physics that can be done with use of the accelerator, we chose the production of RI in consideration of the impression to the students and the connection of the measuring techniques to other experiments. Ordinary metal plates turned to be radioactive after irradiation of proton beam. It is the transformation of the element that medieval alchemists could never accomplish. After the irradiation, the students tried to obtain the energy spectrum of the γ-rays for the identification of the produced RI in the irradiated target. In subsequent 4 weeks after the RI-production, they carried out 9 times of measurements of the intensity of the γ-rays. The measurement of half-life of the RI in four weeks requires short lifetime compared with the course period. It is one of the experiments that are made available only by use of the accelerator.

We chose usual carbon steel as the target. The fraction of the natural iron in the carbon steel is more than 98%. The iron has four natural stable isotopes (and the relative abundances): ^{54}Fe(5.8%), ^{56}Fe(91.72%), ^{57}Fe(2.2%), and ^{58}Fe(0.28%). The most abundant product of the (p, n) reaction with E_p < 20 MeV is ^{56}Co by considering the abundance of

isotopes in the natural iron, their cross sections of the reactions by incident proton of 20 MeV, and the half-lives of the radioactive products. It can be easily identified by the γ-rays with characteristic energies more than 3 MeV. The energy dependence of the cross section of $^{56}Fe(p, n)^{56}Co$ reaction is shown in Figure 1. With use of proton of 20 MeV and 1 μA incident on a steel target of 1 mm thick, the yield of ^{56}Co is estimated as 220 kBq after irradiation of 5 minutes. The half-life of ^{56}Co is 77.27 days[0]. After 4 weeks, the radioactivity of produced ^{56}Co decreases into 171 kBq, which is 78% of the original radioactivity. Measurements with accuracy less than 5% will reveal the exponential nature of the decay rate and the life of the ^{56}Co.

The irradiation of proton was performed in the first target room (TR-1) at CYRIC, Tohoku University. Proton beam of 20 MeV from the AVF-Cyclotron was incident on the target with use of the target conveyer system[0] for the RI production. Before irradiation, students participated in the guided tours through the AVF-Cyclotron room, ion-source room and TR-1. They seemed to be interested in the instruments and machines and asked some questions to the guides: Dr. Fujita M. for the AVF-Cyclotron and ion-source and Dr. Ohtsuki T. for TR-1. After the irradiation, the steel plate was conveyed from the TR-1 to the hot-lab-1. We monitored the radiation by a Geiger counter. It started to beep frequently as the steel plate approached us. It was the efficient occasion for the students to feel the radiation more realistic and consider the radiation protection more severely. The steel plate was packed and sealed in a plastic vessel for easy handling for the subsequent γ-ray measurements. The measurements were carried out in the measurement room in the RI-building. A radiation counter: RC-101A (OKEN) and a sodium iodide probe were used for the measurement. A discriminator in RC-101A can be used both as the leading-edge discriminator and the window discriminator that is also known as the single channel analyzer (SCA). Using the SCA and scanning the threshold, students were able to obtain the energy spectrum of the γ-ray. The energy calibration was done with ^{60}Co source. The obtained energy spectrum is shown in Figure 2. We could find the correspondence of the peaks to the known energies of γ-rays emitted from ^{56}Fe. For 4 weeks after the irradiation, we continued to count the γ-rays with energy threshold higher than 3 MeV in 10 minutes. The background in the same energy range was counted in 1 minute in each measurement. It was multiplied by 10 and subtracted from the count of the γ-ray. The result is shown in Figure 3. Only statistical error is shown in each data point, however, it is not as large as the size of the circles. From the attenuation of the counts

with respect to the time after irradiation, the half-life of the produced RI was obtained as 72.5±2.4 days, which was within 2σ errors from the known half-life of ^{56}Co. As can be seen in Figure 3, the data points deviate more significantly than its statistical error. We suspect some unknown conditions that we could not control in each measurement, affected the results. However, we consider that this kind of uncertainties is essential for the students to inspect the experimental methods and conditions by themselves.

We carried out RI-production experiments in the course of "Basic Research in Physics" for third graders. Teaching staffs and an assistant, planned and prepared the tools and instruments, however, the students arranged and carried out all these measurements by themselves. In the trials and errors to make the measurements as good as possible, the students understood the necessity of the energy calibration of the scintillation probes for the determination of the absolute energies of the γ-rays, the necessity of the identical conditions for each measurement in order to reduce the systematic errors, and the impacts of the errors and uncertainties to the interpretation of the results. All these considerations are required for all the experimental researches. They will be helpful not only for the students who major in the experimental nuclear physics but for all the students who major in other fields of science and technology.

References

1) Table of Isotopes, 8th Ed. (1996).
2) Ohtsuki T., CYRIC News No. **28** (2000) (in Japanese).
3) Experimental Nuclear Reaction Data. URL: http://www.nndc.bnl.gov/exfor/exfor00.htm.

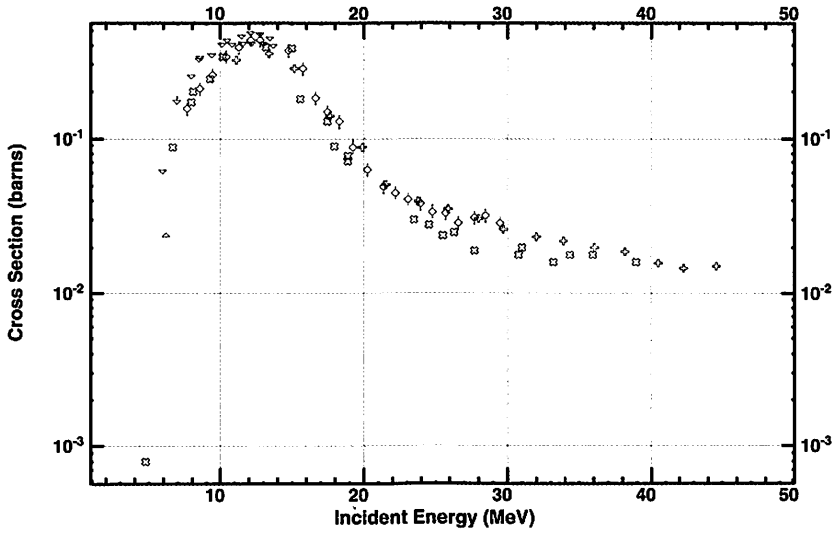

Figure 1. Total cross sections of ^{56}Fe(p, n)^{56}Co taken from Experimental Nuclear Reaction Data library in NNDC[3].

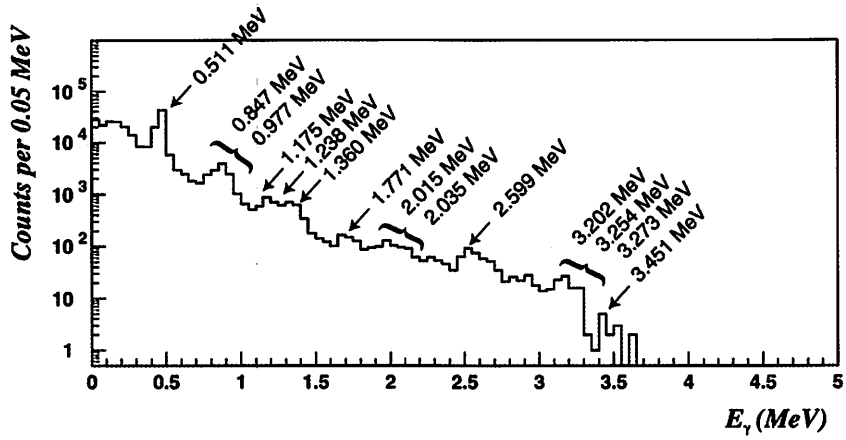

Figure 2. Energy spectrum of emitted γ-ray from the irradiated steel plate measured with the SCA of RC-101A. From the energies of the peaks, we were able to identify ^{56}Co. The energies assigned to the peaks are known energies of the γ-ray of $^{56}Fe^{0}$.

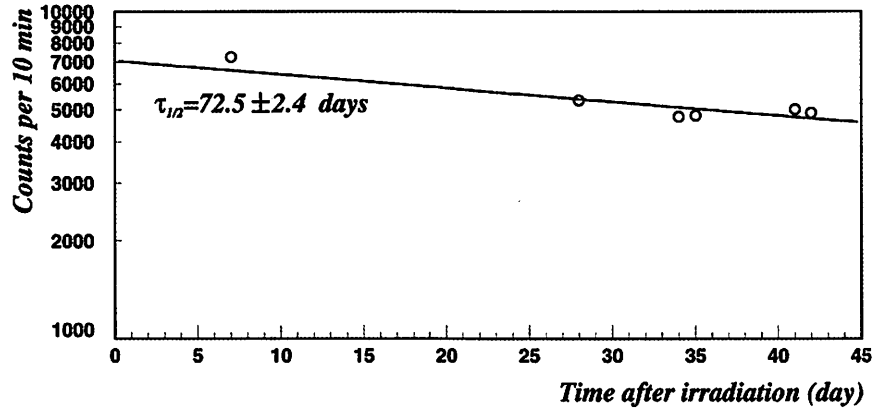

Figure 3. Counts of γ-ray with energy more than 3 MeV with respect to the time after irradiation. By fitting the exponential curve to the data points, half-life of 72.5±2.4 days was obtained.

II. NUCLEAR INSTRUMENTATION

II. 1. Development of the High-Intensity Fast Neutron Beam Facility

Okamura H., Baba M., Kamata S., Itoga T., Hagiwara M., Hasegawa T., Sugimoto N., and Maeda K.[*]

Cyclotron and Radioisotope Center, Tohoku University
[*]*Department of Physics, Tohoku University*

A facility for producing neutrons in the energy range of 20–90 MeV has been constructed at the straight beam-line from the 930 cyclotron (32-course), where intense beams of multi-μA are available. The schematic layout of the facility is shown in Figure 1. The primary beam is transported to bombard the water-cooled production target, bent in the clearing magnet by 25°, and stopped in the water-cooled beam dump, which consists of a carbon block shielded by copper and iron blocks. Using the ^{7}Li(p,n)^{7}Be reaction, quasi-monoenergetic neutron beams of an intensity approximately 10^{6} $n$cm^{-2}sec^{-1}μA^{-1} can be obtained at an energy spread of 1 MeV. The number is almost 10 times larger than those of similar facilities[1,2] owing to the short distance between the production target and the irradiator. Although the thickness of the iron collimator or the concrete shield is rather moderate, thus sacrificing the signal-to-background ratio to some extent, the measured background level is reasonably low. A detailed analysis of intensities of the neutron beam as well as those of background neutrons obtained by using a liquid scintillation counter and time-of-flight method can be found elsewhere in this report[3]. Also the flux distribution of thermal neutrons has been measured by the comparison of activation of Au foils with and without Cd covers, and found to be acceptable in the area around irradiators.

Several projects are being carried out using this facility; a study of three-nucleon force effects via the *n-d* elastic scattering, data accumulation for material activation by fast neutrons which will be used in designing reactors or accelerator facilities, and accelerated simulations of software error in large-scale semiconductor memory devices.

References

1) Vorobyev A.S. et al., Proceedings of the International Conference on Nuclear Data for Science & Technology, ND2004, Santa Fe, Sep. 26-Oct. 1 (2004).
2) Jungerman J.A. and Brady F.P., Nucl. Instr. and Meth. **89** (1970) 167.
3) Kamata S. et al., in this report.

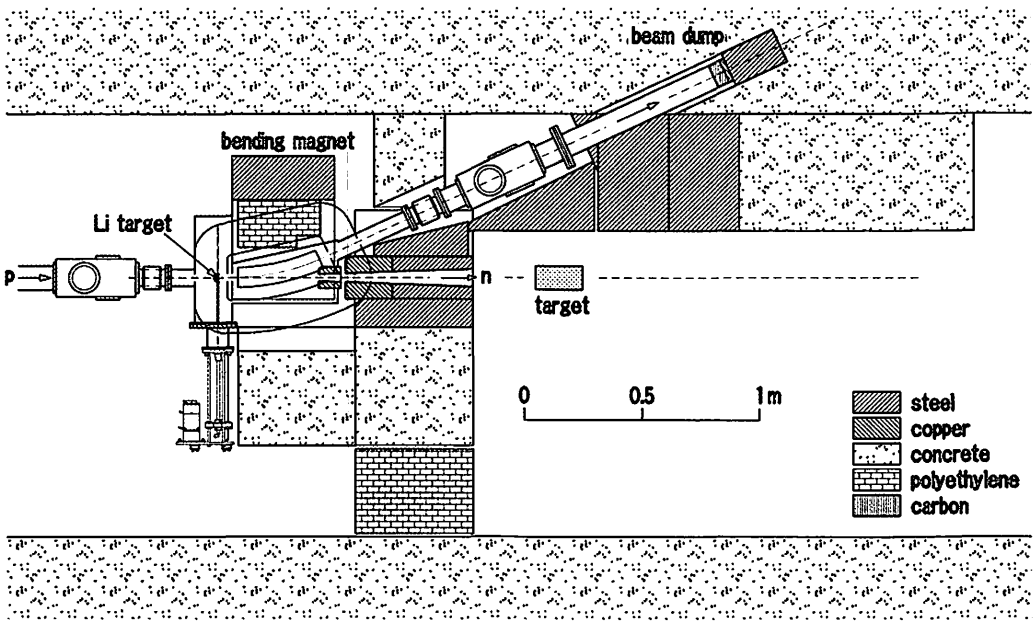

Figure 1. Schematic layout of the fast neutron beam facility constructed at 32-course.

II. 2. Characterization of New Intense ^{7}Li(p,n) Neutron Source at CYRIC

Kamata S., Hagiwara M., Itoga T., Baba M., and Okamura H.

Cyclotron and Radioisotope Center, Tohoku University

A new ^{7}Li(p,n) neutron source has been installed at The Cyclotron and Radioisotope center, Tohoku University. Figure1 shows a schematic view of the new neutron source. It was designed to provide intense neutron flux (> 10^{6}/(cm^{2}·s) at a sample position by enabling short target-sample distance. It will be used extensively for cross section measurement, nuclear physics, and testing of semiconductors for single-event effects, and dosimetry development. Prior to the experiment, it is necessary to confirm the property of the source intensity and background level, because of narrow experimental room, and relatively thin shielding for the lithium target and the beam dump.

For the reason, we have characterized the new neutron source for 3 aspects; 1) the neutron intensity and energy spectra, 2) backgrounds and 3) neutron beamprofile. We have measured the neutron intensity and energy spectra with a TOF (Time Of Flight) method having good energy resolution. These results have confirmed that the intensity of neutron flux is close to the design. Figure 2 shows the measured neutron energy spectra. Figure 2 indicates the energy spectra consist of intense peak component around 880 ch. and continuum spectrum as expected. The peak around 950 ch is attributed to the flame overlap. Table1 summarizes the main features of the measured spectra and the achieved neutron fluence, and shows the present source realizes the expected source intensity.

We have measured the fast neutron backgrounds from the lithium target and the beam dump, and the distribution of thermal neutrons in the room. The fast neutron backgrounds have been derived from the TOF spectrum with shadowing of primary neutron and in off-axis position. Figure 3 shows the measured TOF spectra which consist of foreground neutron, neutron spectrum shadowed of primary neutron, and neutron from the beam dump. These measurements proved that the TOF spectra of fast neutron backgrounds are flat and low (~10^{-3} relative to the peak).

The measurement of the thermal neutron distribution in the irradiation room has used foil activation method combined with imaging plate[1]. This method enables to measure the thermal neutron distribution without γ-rays backgrounds. We concluded that thermal neutron flux was low in the experimental region, while it was 1.0×10^5 /(cm^2s) around the Li-target. These results proved that the new neutron source can be used for practical applications.

The beam-profile was measured by a combination of foil activation and imaging plate[2]. We have measured the signal-to-noise ratio of collimated beam through the comparison between measurements in on-axis and off-axis position. The signal-to-noise ratio was 8:1 for a thin collimator(25 cm thick). It has been measured with TOF method in on-axis and in off-axis position. From these result, we have determined that the signal-to-noise ratio is about 100:1

References

1) Masumoto K., et al,. Rad. Safe. Manage, **1** (2002) 12.
2) Hagiwara M., et al., J. Nucl. Sci. Tech. **Sup. 4** (2004) 267.

Table 1. Summarizes the main features of the measured spectra and achieved neutron fluence.

target thickness [mm]	peak energy [MeV]	beam current [nA]	peak fluence [#/(MeV·Sr·μC)]
4.69	64	15	4.10×10^9

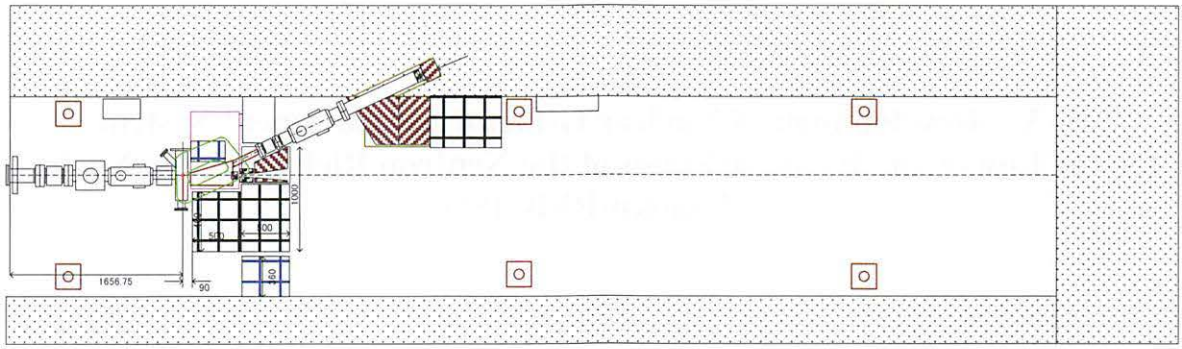

Fig. 1. Schematic view of new ^{7}Li(p,n) source.

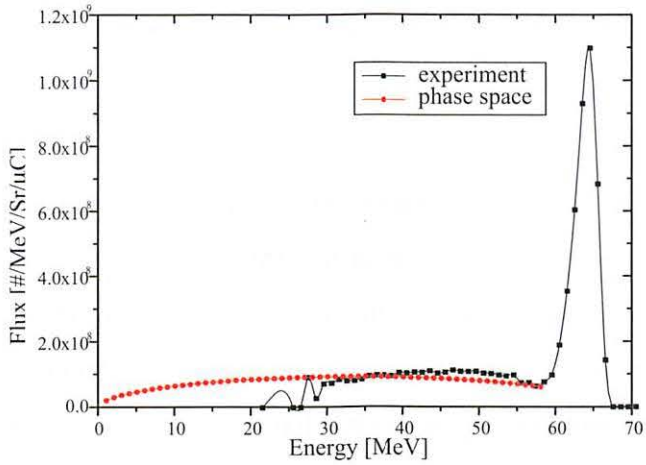

Fig. 2. Energy spectrum of new ^{7}Li(p,n) neutron source.

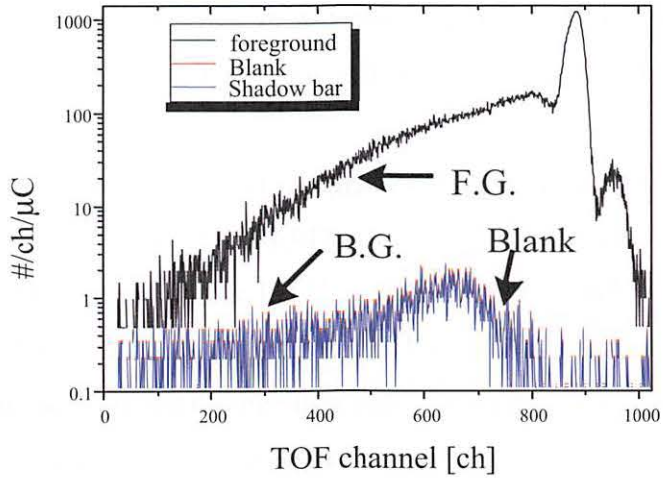

Fig. 3. Energy spectrum of new ^{7}Li(p,n) neutron source.

II. 3. Development of Nuclear G-factor Measurement System for the Low- lying Isomeric States of the Neutron Rich Unstable Nuclei at Tohoku-RFIGISOL

Miyashita Y., Fujita M., Endo T.*, Yamazaki A.*, Suzuki T., Sato N., Sonoda T.**, Tanigaki M.***, Kinoshita S., Koike T., Ma Y., Miura Y., Ukai M., Tamura H., and Shinozuka T.**

Department of Physics, Tohoku University
**Cyclotron and Radioisotope center, Tohoku University*
***Department of Physics, University of Jyvaskyla*
****Research Reactor Institute, Kyoto University*

A PAC (perturbed angular correlation) measurement system has been installed in combination with the RF ion guide system at the ISOL facility in April, 2004. RF ion guide system provides us more neutron rich nuclei produced by proton induced fission reaction with Uranium targets. At the region of neutron rich nuclei around mass ~100, the nuclear g-factor of ground and low-ling states has hardly ever been measured because of the small production cross section and the short half-lives[1]. Therefore, the development of the new system for nuclear g-factor measurement is one of the present main subjects for nuclear structure studies of neutron-rich unstable nuclei.

A new PAC system has been designed with a goniometer (1.6m dia.) and 6 sets of clover HPGe detectors and permanent magnet with magnetic flux density of 1.1 T. The mass separated unstable nuclei by RF-IGISOL, are transferred to the magnet position by the tape transport system[2].

The experiment using new PAC system has been done for the g-factor measurement of the 5/2+ isomer state of ^{113}Cd with TIPAC (Time Integral Perturbed Angular Correlation) method. The parent nuclei of ^{113}Cd and other A=113 isobars have been produced by 50 MeV proton induced Uranium fission reactions and mass separated by RF-IGISOL, then they are implanted onto collection tape of Aluminised Myler. The repeated time sequence for the collection and measurement is as follows; the first 180 sec. for collection with proton beam-on period, the second 1 sec. for tape moving away from the collection position to the detector position, the last 180 sec. for the measurement with

proton beam-off period. In this experiment, the mass-separated yield of ^{113}Ag with low-lying high-spin states was about 150 [atoms/sec] at the detector position.

At the test experiment for the A=113 mass-separated source, we have measured the gamma single spectra, beta gated gamma spectra and gamma-gamma coincidence spectra using the 3-clover Ge detectors and 3 single Ge detectors. Figure 1 shows the detector arrangement with Goniometer, which can set the angular position with 0.1 degree precision. The obtained typical spectrum of beta-gamma coincidence for A=113 is shown in Fig. 2. The whole system of the RF-IGISOL, tape transport system and detectors have been well functioned at this test trial. The nuclear g-factor, however, can not be extracted from the the perturbed angular correlation of the gamma-gamma coincidence spectra, since the statistics of the spectra are not sufficient because of the beam time restriction and relatively low yield from the RF-IGISOL. Presently, the upgrade development of RF-IGISOL system has been progressed on.

References

1) Stone N. J., Table of Nuclear Magnetic Dipole and Electric Quadrupole Moments (2001).
2) Fujita M., et al., CYRIC Annual Report (2002).
3) Benczer-Koller N., et al., Phy. Rev. C **40** (1989) 77.

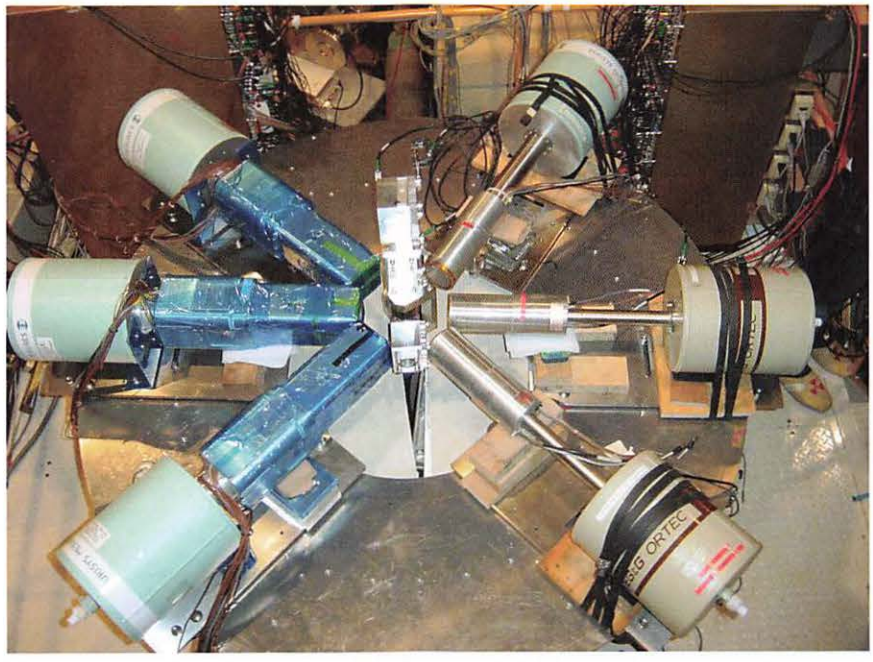

Figure 1. The detector system for the perturbed angular correlation measurement by gamma-gamma coincidence. This Goiniometer platform is located on the 2.5 m stage from the ground level which is 1.25 m higher level from the beam line. Presently, 3 clover Ge detectors and 3 single Ge detectors are used. The permanent magnet with 0.98 T of Nd magnet is installed at the source position for the PAC measurement (the center of Goniometer). The mass separated source is transferred from the beam line (1.25 m level) to the center of Goniometer (2.5 m level) by the tape transport system.

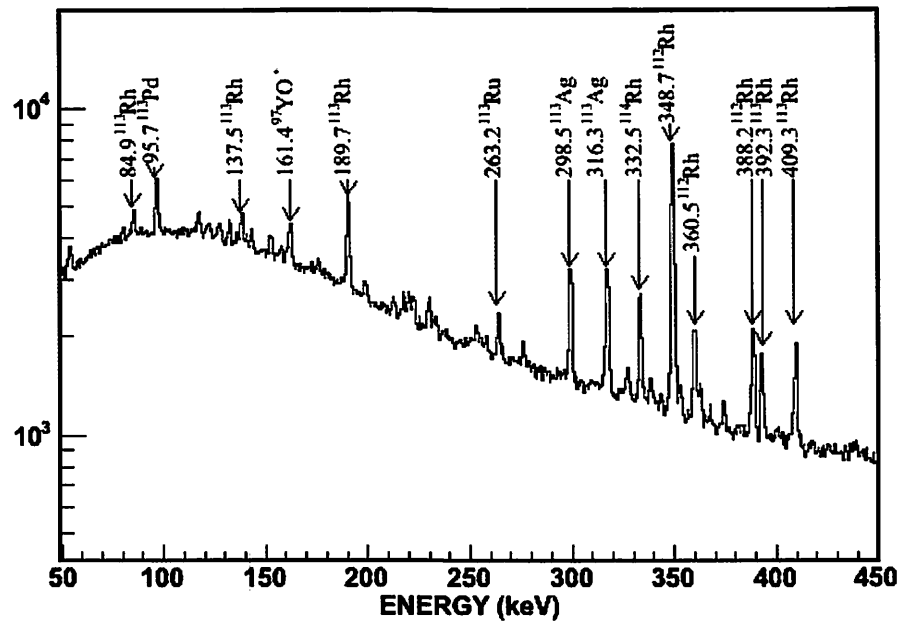

Figure 2. The low energy part of the beta coincident gamma-ray spectrum at the mass number A=113.

II. 4. Beam Spreading System Employing the Double-scattering Method for Proton-therapy Experiments at CYRIC

Terakawa A., Ishizaki A., Totsuka Y., Honda T., Miyashita T., Matsuyama S., Yamazaki H., Ishii K., Okamura H.[*]*, Baba M.*[*]*, Itoh M.*[*]*, and Orihara H.*[**]

Department of Quantum Science and Energy Engineering, Tohoku University
[*]*Cyclotron and Radioisotope Center, Tohoku University*
[**]*Department of Physics, Tohoku Institute of Technology*

The charged-particle beam has the characteristic advantage of depth dose distribution for radiation cancer therapy. We are planning to develop the advanced particle irradiation system and study superior therapeutic effects of proton therapy using small animals. Last year, the beam spreading system providing a broad beam with flat beam intensity was built to develop the devices, such as energy filters, dose and beam profile monitors, for the irradiation system. In this report the design of the beam spreading system and the result of the beam spreading experiments are described.

The setup of the beam spreading system based on the double scattering method[1] is shown in Fig. 1. The first and second scatterers were designed from the multiple-scattering theory for a 80-MeV pencil beam so that the flat beam-intensity field 60 mm in diameter could be obtained at the target located at a distance of 1700 mm from the first scatterer. The first scatterer is a 0.3 mm thick lead foil, while the second scatterer located at a distance of 350 mm from the first scatterer is a dual-ring disk which consists of a 0.5mm thick lead inner disk 17 mm in diameter and an 1.6 mm thick aluminum outer disk 120 mm in diameter. The present system has been installed at the end of the 52-beam line in the target room 5.

The beam spreading experiment with the present system was performed using a 76 MeV-proton beam from the AVF cyclotron at CYRIC. The proton energy was estimated from the range in water. The two-dimensional beam fluence at the target position was measured with an Imaging Plate (IP)[2]. Because of wide dynamic range for dose measurements the IP is a useful dose censer for charge particle beams as well[3]. The IP was irradiated for a few seconds with the proton beam whose intensity was decreased up to

the order of 10 pA using the beam attenuator installed in the beam injection line of the cyclotron. The observed fluence distribution shown in Fig. 2 indicates that a flat fluence field about 60 mm in diameter is obtained. The flatness of the field (the difference between the maximum and minimum intensities of the flat field) is less than 7 %.

The experimental result allows us to use the proton beam from the present system as a therapeutic beam for proton therapy experiments. If the beam energy and profile of the pencil beam from the cyclotron can be optimized, the flatness would be improved.

References

1) Dual-ring double scattering system at Proton Medical Research Center, Tsukuba University, http://www.pmrc.tsukuba.ac.jp/.
2) Fuji Photo film CO., LTD., http://www.fujifilm.co.jp/bio/si_imgplate/imgplate.html
3) Ohuchi H., Yamadera T., Baba M., Radiat. Port. Dosim. **107** (2003) 239.

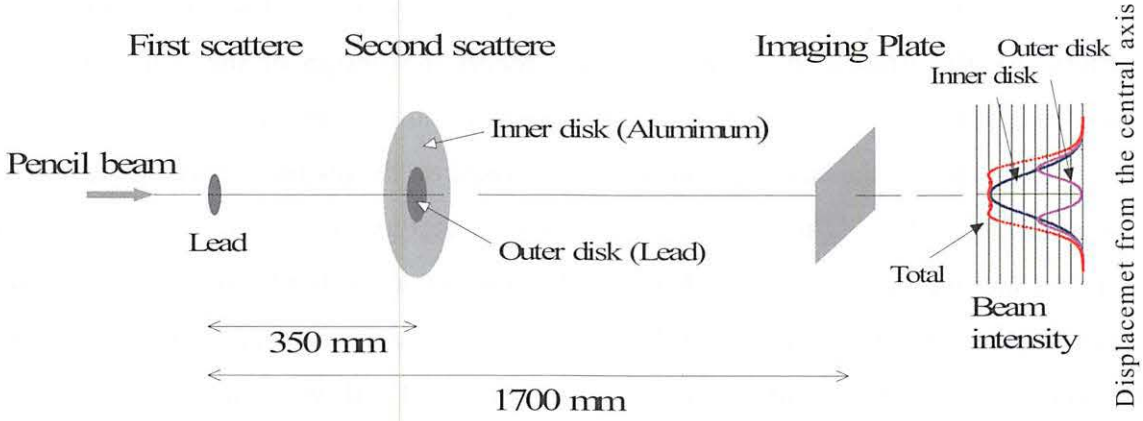

Figure 1. Schematic layout of the beam spreading system based on the double scattering method.

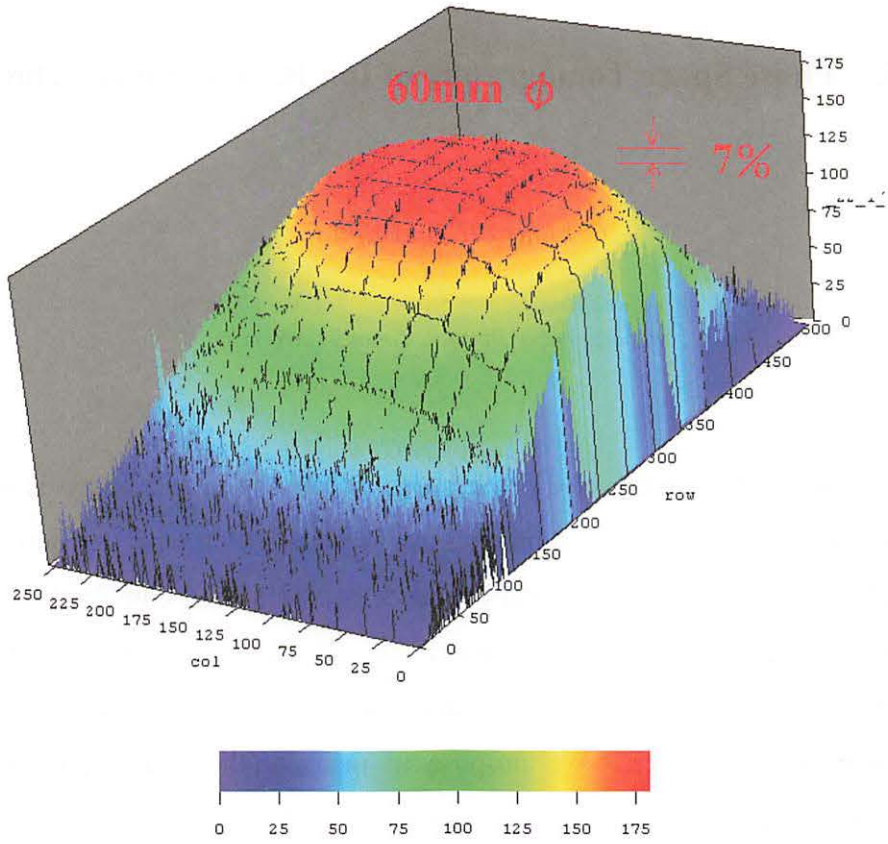

Figure 2. Measured fluence distribution of the proton beam from the beam spreading system.

II. 5. Phase Space Tomography of Ion Beams from Cyclotron

Okamura H. and Kou E.[*]

Cyclotron and Radioisotope Center, Tohoku University
[*]*Department of Physics, Tohoku University*

Measurement of the transverse phase space distribution of the beams is important to the understanding of the particle dynamics as well as to the beam transportation to experimental areas. For low energy ion beams, it is common to employ the combination of a moving slit and a beam profile monitor, but such a mechanical apparatus is rather complicated thus expensive, moreover the edge scattering at the slit becomes troublesome as the beam energy increases. We propose to measure the phase space distribution, $f(x,x')$ in (x,x') plane for example, by using the spatial projections of the beam $p(x,I)$ given as a function of the quadrupole excitation (or magnet current I) and employing the reconstruction techniques used in Computer Assisted Tomography (CAT). This procedure makes no assumption on the phase space distribution such as a two dimensional Gaussian ellipse, unlike the conventional Q-scan method, and is very cost effective because it requires no extra apparatus other than a quadrupole magnet and a beam profile monitor.

Figure 1 shows the presently used configuration of transport elements downstream of the first bending magnet (B1) at the exit of the CYRIC 930 cyclotron. By using the first-order matrices for a drift space and a quadrupole magnet,

$$M_D(\ell)=\begin{pmatrix}1 & \ell\\ 0 & 1\end{pmatrix} \text{ and}$$

$$M_Q(k,d)=\begin{pmatrix}\cos\varphi & {}^{1}\!/\!_{\sqrt{k}}\sin\varphi\\ -\sqrt{k}\sin\varphi & \cos\varphi\end{pmatrix} \text{(focus) or} \begin{pmatrix}\cosh\varphi & {}^{1}\!/\!_{\sqrt{|k|}}\sinh\varphi\\ \sqrt{|k|}\sinh\varphi & \cosh\varphi\end{pmatrix} \text{(defocus)},$$

respectively, where $\varphi=\sqrt{k}d$ and $kx=eB/p$, the transport matrix in (x,x') or (y,y') plane can be expressed as

$$M_D(\ell_6)M_Q(k_6,d)M_D(\ell_5)M_Q(k_5,d)M_D(\ell_4)M_Q(k_4,d)M_D(\ell_3) = A\begin{pmatrix}\cos\theta & \sin\theta\\ \cdots & \cdots\end{pmatrix},$$

which, concerning the spatial projection, can be regarded as the combination of a rotation in the phase space by θ and a magnification by A. In the present configuration, θ and A are related to the excitation current I of the QP5 quadrupole magnet as shown in Figure 2.

Figure 3 shows the measured beam profile of a 40-MeV α beam for various excitation currents I. They are projected onto x and then converted to $p(u,\theta)$ by using the above relation, where $u = x\cos\theta + x'\sin\theta$. According to the Filtered Back-Projection (FBP) method, which is a commonly used technique in the tomography, the phase space distribution $f(x,x')$ is obtained by the following successive Fourier transformations:

$$G(\rho,\theta) = \int_{-\infty}^{\infty} p(u,\theta)\exp(-2\pi i\rho u)\,du,$$

$$Q(x\cos\theta + x'\sin\theta,\theta) = \int_{-\infty}^{\infty} G(\rho,\theta)\exp[2\pi i\rho(x\cos\theta + x'\sin\theta)]|\rho|\,d\rho, \text{ and}$$

$$f(x,x') = \int_0^{\pi} Q(x\cos\theta + x'\sin\theta,\theta)\,d\theta.$$

The resulting distribution is displayed in Figure 4. The overall distribution appears physically reasonable, but some spurious oscillatory structure is observed, presumably caused by the limitation in θ-range, which is 1.6π instead of 2π.

References

1) McKee C.B., O'Shea P.G., Madey J.M.J., Nucl. Instr. and Meth. A **358** (1995) 264.

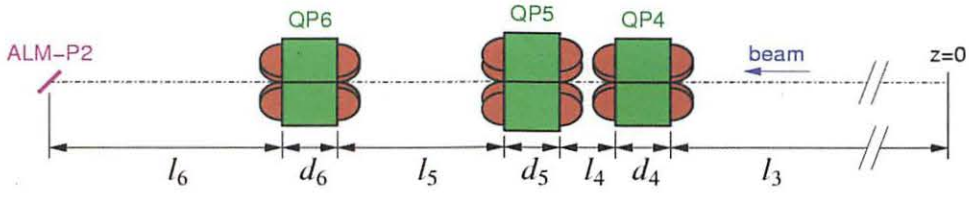

Figure 1. Configuration of the transport elements downstream of the first dipole magnet at the exit of the CYRIC 930 cyclotron. d_4=d_5=d_6=0.24 [m], l_4=0.21 [m], l_5=0.82 [m], and l_6=1.055 [m].

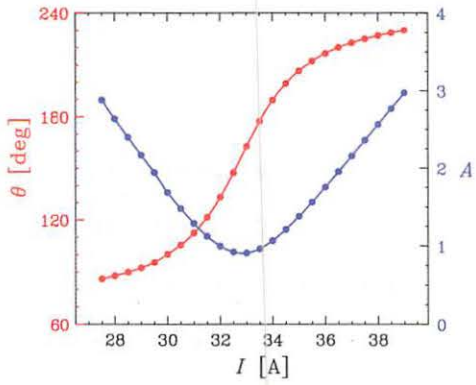

Figure 2. Phase space rotation angle θ and the magnification factor A as a function of the excitation current I of the QP5 quadrupole magnet. The drift length l_3 is chosen to 2 m.

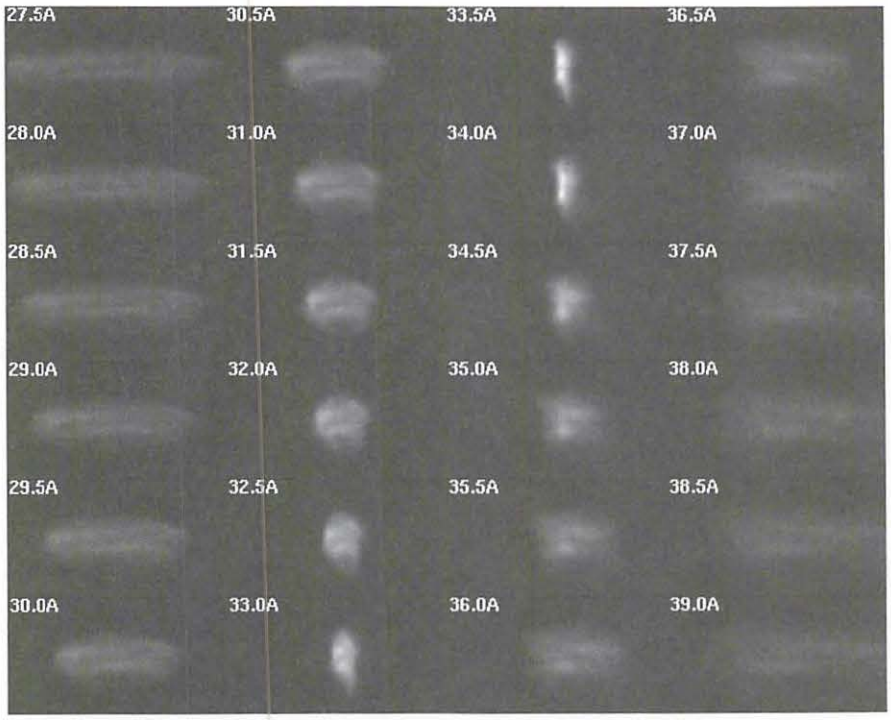

Figure 3. Measured beam profile of a 40-MeV α beam for various excitation currents I of QP5.

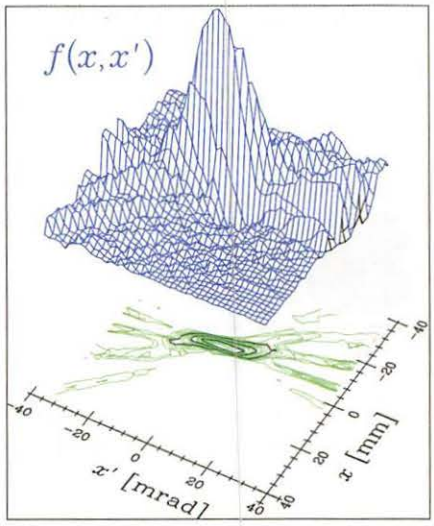

Figure 4. Resulting phase space distribution obtained by the FBP method.

III. NUCLEAR ENGINEERING

III. 1. Effects of Helium-implantation on Fracture Behavior of Reduced Activation Martensitic Steel F82H

Hasegawa A., Suzuki A., Tanaka K., Satou M., Abe K., and Jitsukawa S.[*]

Department of Quantum Science and Energy Engineering, Tohoku University
[*]*Japan Atomic Energy Research Institute, Tokai Lab.*

Introduction

Reduced activation ferritic/martensitic steels are candidate structural materials for fusion reactor. In the fusion reactor environment, 14 MeV neutron irradiation will produce large amount of displacement damage and helium in structural materials. For instance, displacement damage will be 100 dpa and helium concentration will be 1000 appm in ferritic/martensitic steels after 10 MW/m^2 neutron wall loading. The irradiation caused an increase of strength (hardening) at temperature below 400°C and the hardening reduces facture toughness, which includes a DBTT (Ductile Brittle Transition Temperature) shift to higher temperatures. It is one of important material issues for component design. Previous works showed that the ferritic/martensitic steels had enough resistance to microstructural changes by irradiation and DBTT shift caused by the irradiation mainly depended on the irradiation hardening below 400°C[1,2].

It is well known that helium stabilizes point defect cluster and causes additional hardening at lower temperature region or increases swelling at higher temperature region. To study the helium effects of ferritic/martensitic steels, helium doping experiment using neutron irradiation with B- or Ni-doped specimen have been used, and these results show that helium doping tends to be accompanied by additional hardening, and the increased effect of helium seems to be about one third or smaller than has been indicated previously with He levels less than 400 appm irradiated below 400°C[2]. On the other hand, helium atoms in the materials diffused to form bubbles at preexisting grain boundaries during irradiation at a high temperature. The bubble formation at grain boundary tends to change the fracture mode from transgranular to intergranular cracking. It was reported that the martensitic steels were highly resistant to helium bubble-induced grain boundary

embrittlement at high temperatures by tensile test[3-5] but the effect on fracture behavior by impact test after higher helium concentration had not been performed yet.

Helium implantation technique is more effective to evaluate helium effects directly and many investigations have been performed for the martensitic steels. Since the range of the implantation is usually smaller than 0.2 mm, the experiments have been often limited to microstructural observation, hardness measurement and tensile test with thin specimens. We had already reported the He effect of DBTT of martensitic steels JLF-1 using 650 appm He implanted TEM disks by means of small punch test[6]. Increase of DBTT caused by irradiation hardening was observed, however, grainboundary embrittlement was not observed. It is well known that charpy impact test is more appropriate to estimate DBTT behavior, but relatively larger specimen volume is needed for charpy impact test.

In this work, to study the He effects on fracture behavior of reduced activation steels by impact test after higher temperature irradiation, He-ion implantation at around 550°C was performed and small size charpy impact test of the He implanted specimens was conducted.

Experimental

He-ion implantation was carried using an irradiation chamber of target course 4. Detail of the irradiation apparatus and post irradiation experiments were already shown in elsewhere[7]. Mini size charpy specimens (1.5 CVN) were prepared from a F82H IEA heat. Helium implantation was performed by a cyclotron of Tohoku University with a beam of 50MeV α-particles at temperature around 550°C. A tandem-type energy degrader system was used to implant helium into the specimen homogeneously from the surface to the implanted range of 50MeV α-particles, which was about 380 μm. Calculated implanted He concentration was about 1000 appm. Charpy impact test was performed using an instrumented impact test apparatus of Oarai branch of IMR, Tohoku University. Analyses of absorbed energy change and fracture surface were carried out. Vickers hardness test was also carried out on the He implanted area of the 1.5 CVN specimen to estimate irradiation hardening.

Results

Figure 1 shows result of DBTT curves of F82H before and after He-implantation. The DBTT of unimplanted specimen was about -110°C and that of helium implanted specimen was about -40°C. Analysis of absorbed energy showed that DBTT increase by

the 1000 appm He implantation at around 550°C was about 70°C.

Figures 2 to 4 show typical fracture surface observation result of unimplanted and helium implanted specimen using a scanning electron microscope. Figure 2 and 3 show the results of unimplanted specimen tested at -80°C and -140°C, respectively. Figure 2 shows typical results of ductile ruptured specimens. It shows a reduction of area at the cross section of ruptured area, and dimple pattern which correspond to plastic deformation.

Figure 3 shows result of brittle ruptured unimplanted specimen tested at -140°C. Ruptured surface is covered by cleavage surface and the reduction of area at a ruptured surface was not observed. This is typical ruptured surface of transgranular fracture mode.

Figure 4 shows result of He implanted specimen ruptured in brittle manner. Tested temperature of this specimen was -60°C. Grain boundary surface was observed from the specimen surface to about 400 μm depth region. It corresponds to helium implanted region. The grain boundary ruptured surface was not observed in helium implanted specimens ruptured in a ductile manner. Microstructural observation of the helium implanted specimen had not been carried out yet, but previous works showed that helium bubble formed in ferritic/martensitic steels around 500 to 600°C[5,6]. Therefore, it may be considered that the grainboundary fracture probably caused by crack initiation from helium bubble at grain boundary during deformation and decreased the absorbed energy. Microstructural observation will be performed near future and the helium effect on the fracture behavior will be discussed based on these experimental results.

Summary

Helium implantation up to about 1000 appm at 550°C was performed to reduced activation ferritic/martensitic steel F82H. Small size charpy impact test was conducted to the He implanted specimens. The following results were obtained.

(1) Increase of DBTT by the He implantation was about 70°C.

(2) Grain boundary ruptured surface was only observed He implanted region of specimens ruptured in brittle manner.

Acknowledgements

The authors are grateful to the staffs in the CYRIC of Tohoku University relating to beam transport and irradiation experiments. The authors are also grateful to Mr.

T.Takahashi, Mr. K.Komatsu and Mr. Nagaya of machine shop of Dep. of Quantum Science and Energy Engineering, Tohoku University for fabrication of specimen loading system and energy degrader system.

References

1) Jitsukawa S., Tamura M., van der Schaaf B., Klueh R.L., Alamo A.,Petersen C., Schirra M., Spaetig P., Odette G.R., Tavassoli A.A., Shiba K., Kohyama A., and Kimura A., J. Nucl. Mater. **307-311** (2002) 179.
2) Jitsukawa S., Kimura A., Kohyama A., Klueh R.L., Tavassoli A.A., van der Schaaf B., Odette G.R., Rensman J.W., Victoria M., and Petersen C., J. Nucle. Mater. **329-333** (2004) 49.
3) Stamm U., and Schroeder H., J. Nucl. Mater. **155-157** (1988) 1059.
4) Moslang A., and Preininger D., J. Nucl. Mater. **155-157** (1988) 1064.
5) Hasegawa A., and Shiraishi H., J. Nucl. Mater. **191-194** (1992) 910.
6) Kimura A., Morimura T., Kasada R., Matsui H., Hasegawa A., and Abe K., Effects of Radiation on Materials, 19th International Symposium, ASTM STP 1366, M.L. Hamilton, A.S. Kumar, S.T. Rosinski and M.L. Grossbeck, Eds., American Society for Testing and Materials, 1999.
7) Hasegawa A., Wakabayashi E., Tanaka K., Abe K., and Jitsukawa S., CYRIC Annual Report **2002** (2003) 34.

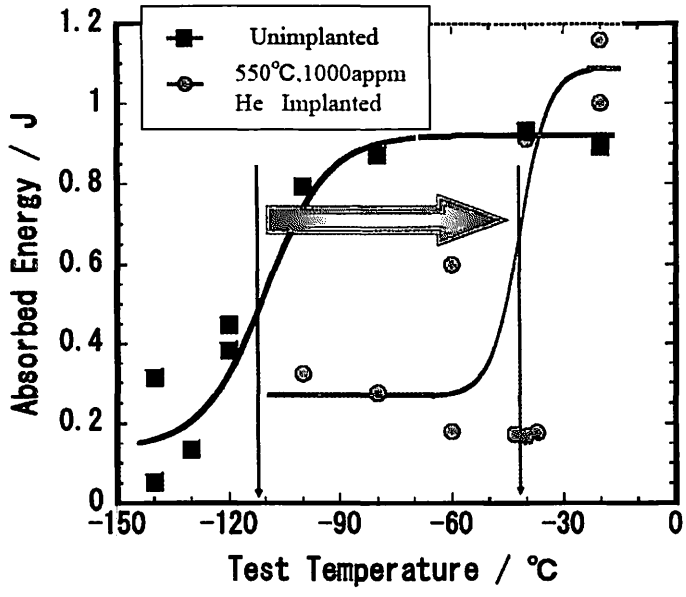

Figure 1. Absorbed energy vs. test temperature curves of helium implanted/unimplanted samples.

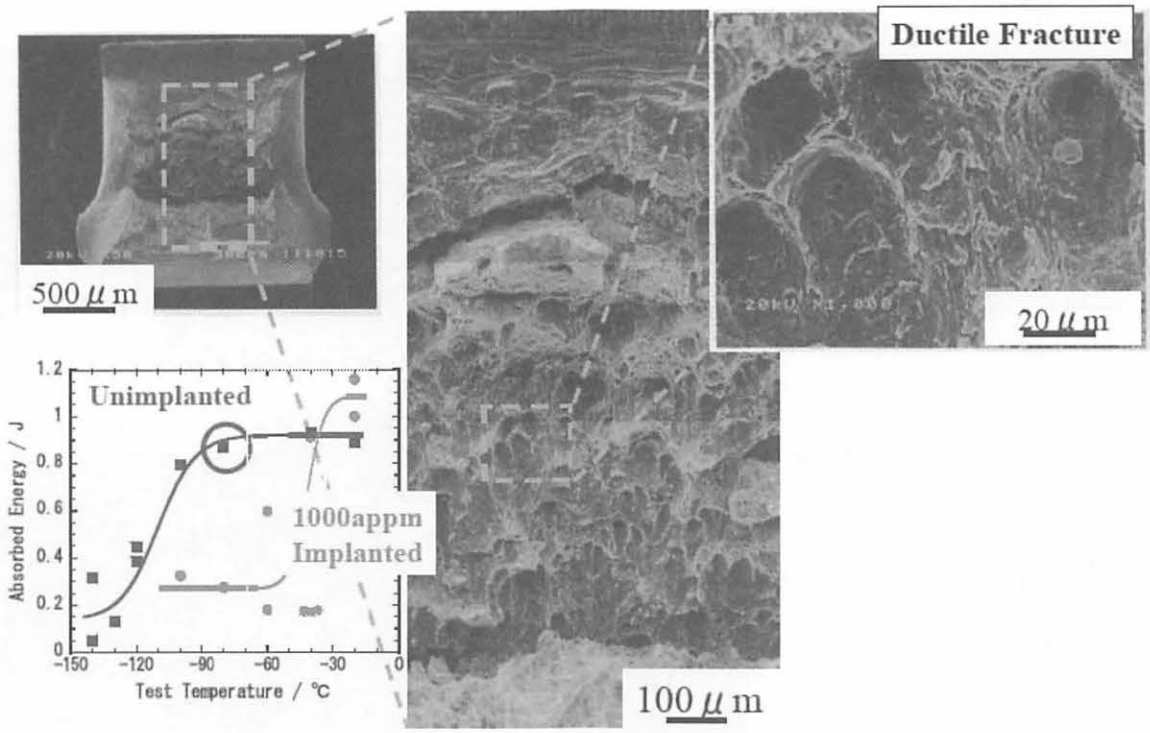

Figure 2. Fracture surface observation results of unimplanted specimen. Test temperature: -80°C.

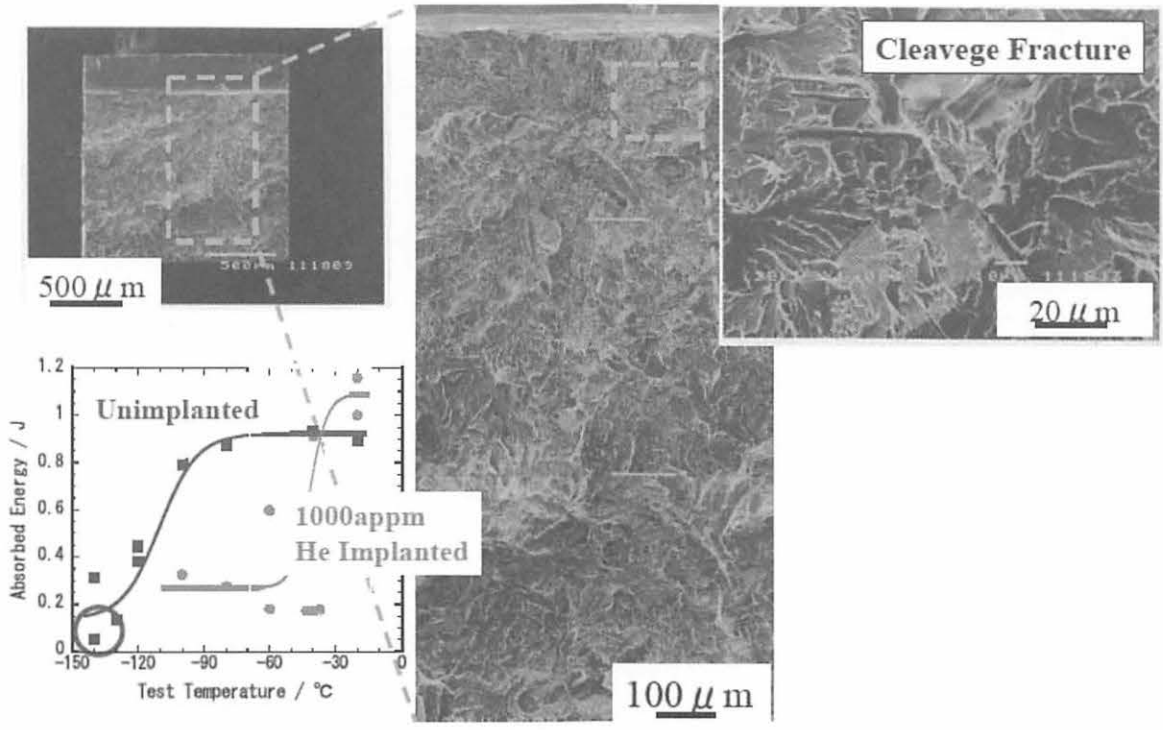

Figure 3. Fracture surface observation results of unimplanted specimen. Test temperature: -140°C.

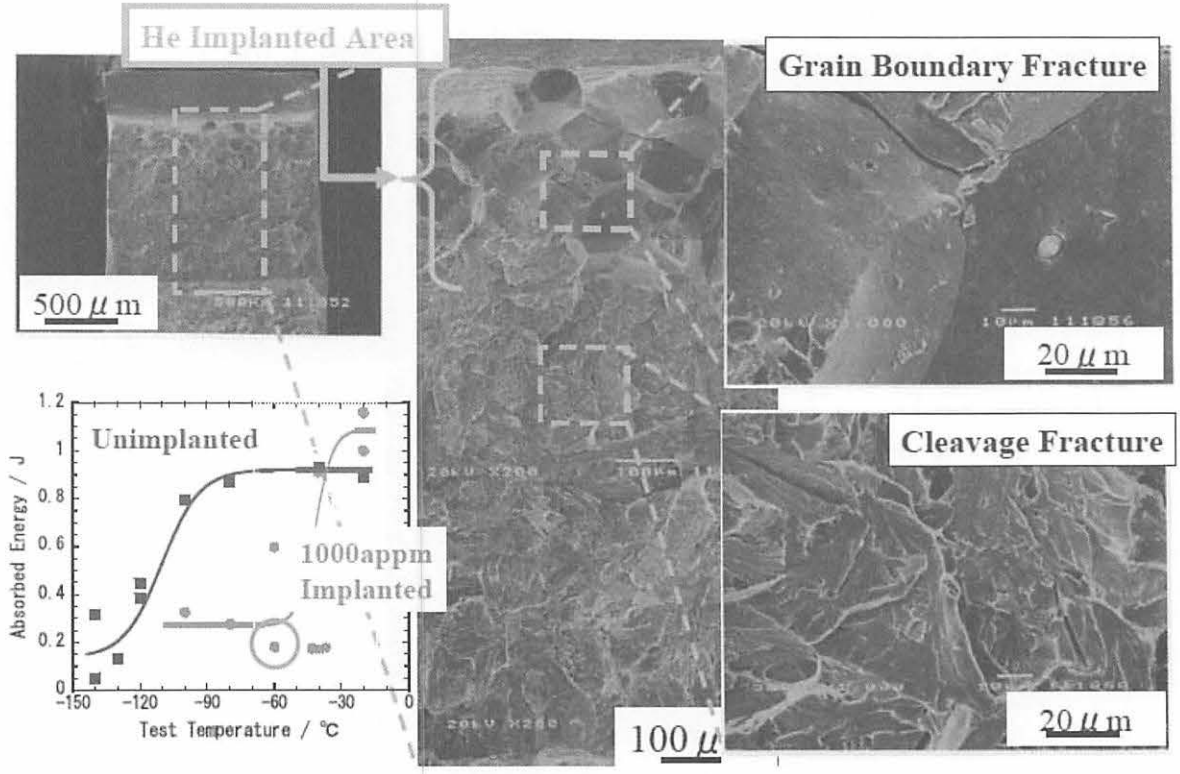

Figure 4. Fracture surface observation results of helium implanted specimen. Test temperature: -60°C.

III. 2. Measurement of Neutron Emission Spectrum and Activation Cross-section on Fe and Ta for 40 MeV Deuteron Induced Reaction

Itoga T., Hagiwara M., Oishi T., Kamada S., and Baba M.

Cyclotron and Radioisotope Center, Tohoku University

The International Fusion Materials Irradiation Facility (IFMIF) project has been proposed to establish an accelerator-based D-Li neutron source designed to produce an intense fast neutron field for high fluence irradiation test of the fusion reactor candidate materials[1].

To establish the database required for the design and post-analysis of IFMIF, we have been conducting systematic experiments on the neutron emission spectrum and radioactivity accumulation in IFMIF structural elements from 2001[2-6]. In the previous reports (2001, 2002, 2003), the results on lithium target for 25, 40 MeV deuterons and on carbon and aluminum targets for 40 MeV deuterons were reported. The experiments were carried out at the No.5 target room in CYRIC using the AVF cyclotron (K=110 MeV), a beam swinger system, the TOF method[7] employed stack target[5] was used to enable measurements of neutron spectrum and activation cross section concurrently.

In the last year, we have carried out new experiments for 40 MeV deuterons with extended techniques and obtained new results for

1) neutron emission spectrum from a thick Fe, Ta target and
2) activation cross-sections of the ^{nat}Fe(d, x)^{51}Cr, ^{52}Mn, $^{56, 57, 58}$Co reactions.

The experimental method was almost the same with these in previous experiments[5]. Twenty thin targets of iron (2.0 mm thicknesses) and thirty thin targets of tantalum (1.5 mm thicknesses) with natural composition were prepared and stacked to stop the incident beam in the targets to measure not only neutron spectra from a thick Fe and Ta target but also excitation functions of the ^{nat}Fe(d, x)^{51}Cr, ^{52}Mn, $^{56, 57, 58}$Co reactions concurrently.

The neutron spectra were measured for almost entire range (0.5-50 MeV) of secondary neutrons at seven laboratory angles between 0- and 110-deg with the two-gain

time-of-flight (TOF) method[7] using a beam swinger system. The results are shown in Fig.1. Figure 2 shows the comparison with the results of previous experiments[2-6]. The data clarified secondary neutron production spectra for the whole energy range. The lower energy limit is approximately 0.5 MeV and both spectra show almost same features. Such data are very few and will be useful for the model development of the neutron emission. The main peaks due to deuteron break-up reaction are observed around 15 MeV having strong angular dependence similar with previous results of Li(d,xn) reactions[2-6]. This yield of the main peak is decreasing with the increasing mass of target. On the other hands, the yield of neutrons emitted from the evaporation process is increasing with the mass of target. Figure 3 shows the comparison between the present data and MCNPX calculation[8]. The results of calculation significantly underestimate experimental data.

The number of radioactive nuclides accumulated in the stacked targets was measured by counting the γ-rays from the nuclides of ^{51}Cr, ^{52}Mn, $^{56, 57, 58}$Co using a pure Ge detector. In Figs.4, 5, the results of the activation cross-sections are shown, together with other experiments[9], recommended data by the IAEA group[10] and TALYS calculation[11]. The present values for iron are consistent with other data. TALYS calculation shows fairy good agreement with the present data except for higher energy region. To estimate the radioactivity induced by deuterons with TALYS, nevertheless, improvements will be required for cross-section calculation models. Present experimental results will be used as the basic data to check the accuracy of the Monte Carlo simulation and for the shielding design of a medium energy accelerator facility such as IFMIF.

*In collaboration with National Institute for Fusion Science (NIFS).

References

1) IFMIF CDA TEAM, IFMIF Conceptual Design Activity Final Report edited by Marcello Martone, Report 96.11, Enea, Dipartimento Energia, Frascati (1996).
2) CYRIC Annual Report 2001, p. 170; 2002, p. 141; 2003, p. 43.
3) Baba M., Aoki T., Hagiwara M., et al., J. Nucl. Materials **307-311** (2002) 1715.
4) Aoki T., Hagiwara M., Baba M., et al., J. Nucl. Sci. Tech. **41** (2004) 399.
5) Hagiwara M., Itoga T., Baba M., et al., J. Nucl. Materials **329-333** (2004) 218.
6) Hagiwara M., et al., J. Fusion Sci. Tech., in press.
7) Ibaraki M., et al., Nucl. Sci. Technol. **35** (1998) 843.
8) Waters L.S. (Ed.), MCNPX User's Manual version 2.4.0, LA-CP-02-408, Los Alamos National Laboratory, Los Alamos, New Mexico, 2002.
9) EXFOR system: OECD/NEA http://www.nea.fr
10) IAEA, Charged-particle cross section database for medical radioisotope production_ http://www-nds.iaea.org/medical/.
11) Koning A.J., et al., TALYS: Comprehensive nuclear reaction modeling, Conf. on Nucl. Data for Sci. and Technol., Santa Fe, 2005.

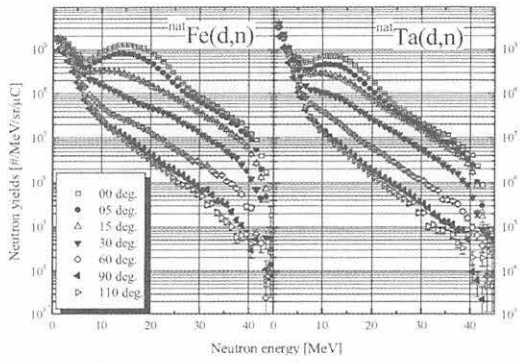

Fig. 1. Neutron spectrum for Fe and Ta .

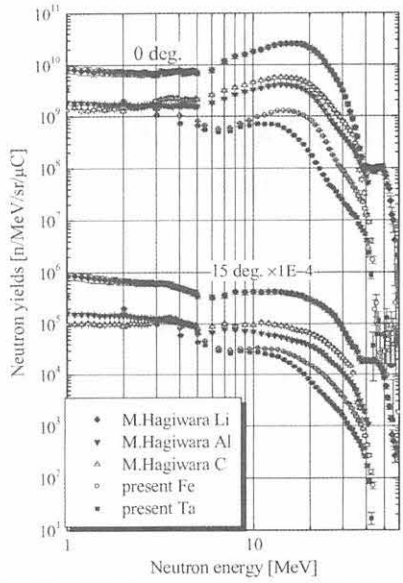

Fig.. 2. Neutron spectrum for (d,n) reactions at 40 MeV.

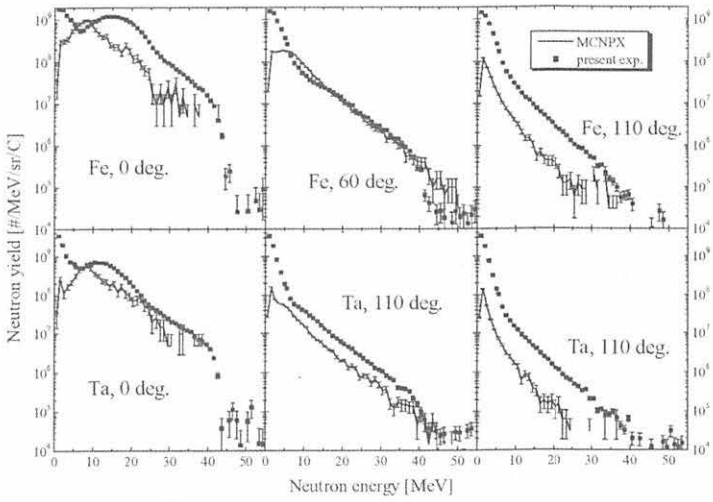

Fig. 3. Comparison with MCNPX.

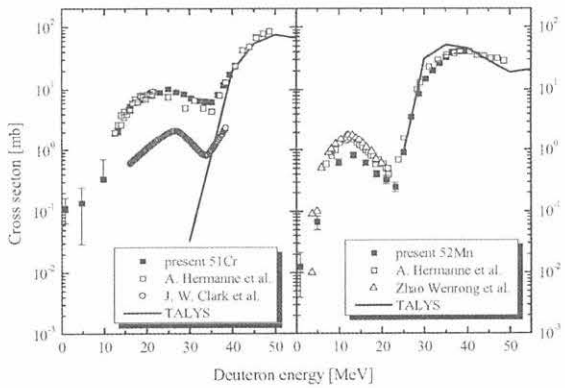

Fig. 4. Activation cross-section for ^{nat}Fe(d, x)^{51}Cr, ^{52}Mn.

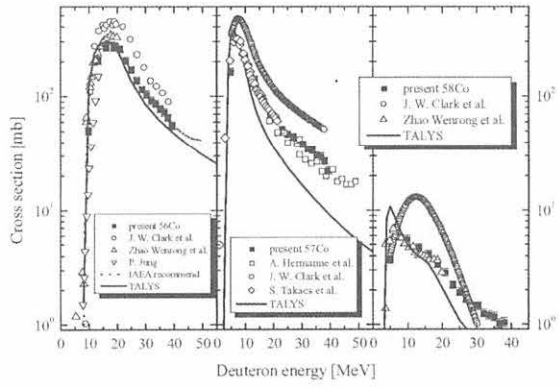

Fig. 5. Activation cross-section for ^{nat}Fe(d, x)^{56}Co, ^{57}Co and ^{58}Co.

III. 3. Application of Digital Signal Processing to Bragg Curve Spectrometer Using Digital Storage Oscilloscope

Oishi T., Sanami T., Hagiwara M., Itoga T., Yamauchi T., and Baba M.*

Cyclotron and Radioisotope Center, Tohoku University
**High energy accelerator research organization*

Digital signal processing technique is a data handling method in which each signal waveform from a detector is acquired as digital data, and the information of the radiation, for example energy and time, can be derived through the analysis of the signal waveform using computers. Although this method has been carried out for more than ten years, it has not been always useful because of slow performance of ADCs and computers. Recently, the signal waveform acquisition becomes possible in a acceptable counting rate with a relatively simple way owing to the speedup of ADCs and computers. Therefore it becomes possible to apply the DSP technique to the practical radiation detection.

The most significant advantage of DSP technique is the possibility of flexible signal analysis which is difficult with the analog circuits. In this work, we intend to extract the fission fragment's events from signals overlapped with noise taking this advantage of the DSP technique. In addition, the DSP technique has more advantage for example, reduction of load for preparation of experiments owing to very few analog circuits required, and the possibility of high quality reanalysis owing to computing analysis.

In this study, this method was adopted to the measurement of fragments from neutron induced reaction for Bragg carve spectrometer (BCS). Figure 1 shows a schematic view of the BCS which is a cylindrical gridded ionization chamber[1,2]. A target was set up in the center of a scattering chamber and irradiated by protons. Fragments from the target produced by proton induced reaction enter the BCS through the window and ionize the gas in the BCS. Electrons drift toward the anode by the electric field keeping a shape of ionization distribution Bragg curve. Therefore, the time distribution of the anode signal corresponds to just the reversed. Thus, the fast part of anode signal is proportional to the Bragg peak that provides the information on the atomic number of the fragment. The

integration of the whole anode signal represents the total charge that is proportional to the fragment energy. By using the anode signal, we distinguish the energy and the charge of fragments event by event.

Signals from the BCS were digitized a Lecroy WAVEPRO7000 digital storage oscilloscope (DSO) with a sampling frequency of 100 MHz after charge sensitive preamplifier. Digitized signal data were stored in HDD of DSO and real time analysis was carried out by a computer with Ethernet connection.

Figure 2 (blue line) shows a typical signal data which is integrated Bragg curve by a preamplifier. Signal acquisition without preamplifier is difficult because of low SN ratio. In order to obtain the Bragg curve, it is needed to differentiate the signal. High frequency noise disturbs the differentiation. Accordingly, smoothing spline method was applied to suppress the noise, and signal waveform after applying shows in Fig. 2 (red line). The Bragg curve was obtained by differentiation of the applied signal waveform as shown in Fig. 3. Information of the Bragg peak, delta E and energy are obtained from Bragg curve. Bragg peak is defined as the peak of the Bragg curve and delta E is obtained from the Bragg curve's pulse height at constant time from particle injection. Energy is equal to pulse height of preamplifier out. Using this method, mass of fragments can be distinguished by delta E-E method with only one detector.

Figure 4 shows a scatter plot of Bragg peak and energy. Figure 5 shows a scatter plot of delta E and energy. In Fig. 4, we can recognize the separation of fragments in each atomic number, from bottom to top, helium, lithium, beryllium, boron, carbon. Moreover, it is clear that each mass is separated in Fig. 5.

In the future, proton induced reaction double differential fragment produce cross-section in each mass will be available using this method. DSP method has much possibility. Application and improvement of this technique for various detectors is in progress[3].

References

1) Ito N., Baba M., et al., Nucl.Instrum.Meth. **A337** (1994) 474.
2) Hagiwara M., et al., CYRIC Annual Report 2004 to be published.
3) Oishi T., et al, J. Rad.. Prot. Bulletins (submitted).

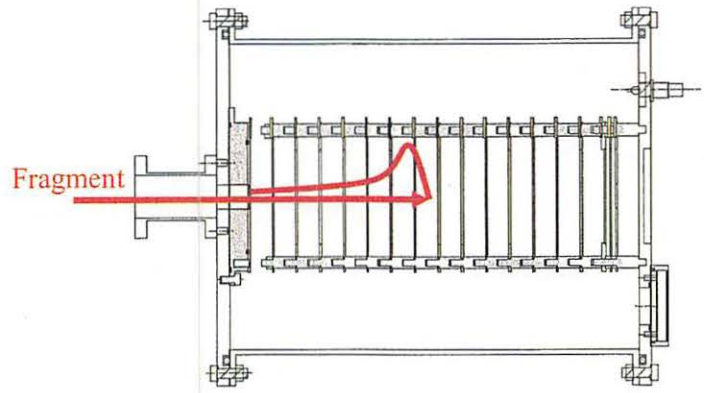

Fig. 1. Schematic view of the Bragg curve spectrometer.

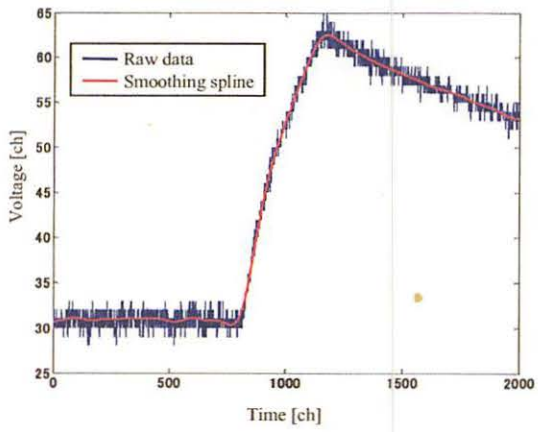

Fig. 2. Typical signnal data and smoothing spline.

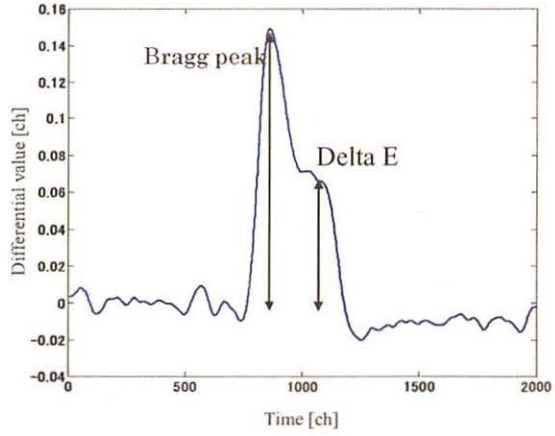

Fig. 3. Bragg curve.

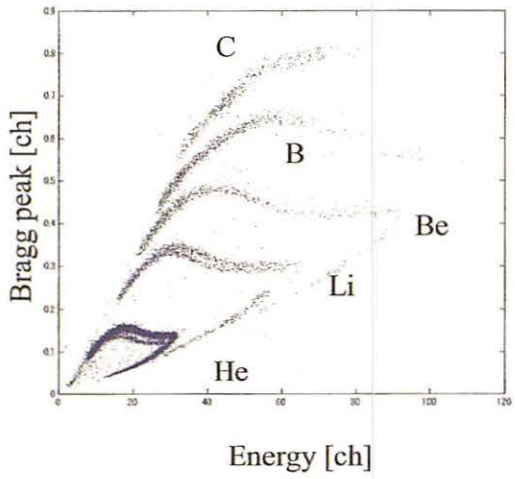

Fig. 4. Bragg peak vs. Energy.

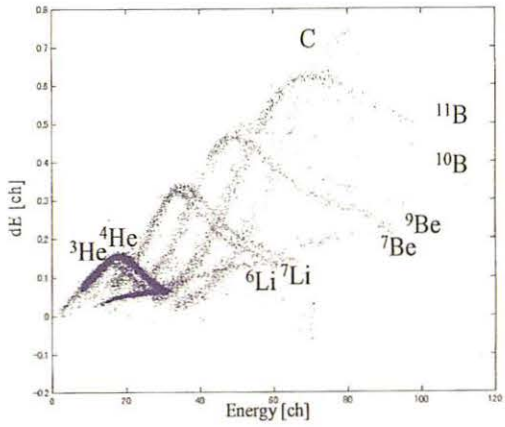

Fig. 5. Delta E vs. Energy.

III. 4. Upgrade of Ion Irradiation Apparatus for Semiconductor Devises

Makino T., Hagiwara M., Itoga T., Hirabayashi N., and Baba M.*

Cyclotron and Radioisotope Center, Tohoku University
**Tokyo Electric Power Company*

As reported in 2002 Annual report, we installed an ion irradiation apparatus to test radiation resistivity of semiconductors for use in the space exploration with protons and heavy ions, at the 33 course in Tohoku University k=110 AVF cyclotron (Fig. 1)[1,2]. The apparatus was designed to meet the required 1) beam fluxes of ~10^7 #/cm^2•s (~ pA) for protons and ~10^4#/cm^2•s for heavy ions, and 2) the flat beam profile over the devices (~ a few cm), for simulating the space environment. In addition, 3) a beam with various energies is required for study of the energy dependence of the resitivity. The system performed fairly satisfactory, but has a room for improvement: 1) beam uniformity, and 2) energy dependence of the SEM sensitivity.

To improve the performance we modified the arrangement, we moved the diffuser to 1.5m upstream along the beam line. A beam from the cyclotron is diffused and made flat with a gold diffuser. After that, the beam is led into SEM (secondary emission monitor) for the measurement of beam intensity in real time. Then, the beam energy is changed with copper degraders for the case of protons, and a cocktail beam (mixture of ions with the same M/Z where M is mass of the accelerated ion, and Z is charge of the ion) for heavy ions. Finally, the beam is extracted to the air through a Kapton foil which separates the beam line from air. Further, an external Faraday cup was prepared at devise position, and we can measure the absolute value of beam current at the device position by means of the Faraday cup. Newly installed beam attenuator in the incident line is also very helpful for control of beam intensity.

The beam profile and beam flux are important on the irradiation test. Therefore, we developed the measurement method of the beam profile at devise position by using IP (imaging plate: high sensitive two-dimensional imaging sheet)[3,4]. We can measure the

beam profile with good spatial resolution from directly irradiated IP by applying special readout technique with filter sheets (Fig. 2)[5]. The beam flux can be measured reliably using SEM. The apparatus is stably running on proton irradiation test.

We are implementing S-SEM (Segmented-SEM) for all ions and a position-sensitive gas counter to measure the beam flux and profile concurrently.

References

1) Bisello D., et al., Nucl. Instrum. Methods B **181** (2001) 254.
2) Virtanen A., et al., Nucl. Instrum. Methods A **426** (1999) 68.
3) Sanami T., et al., Nucl. Instrum. Methods A **440** (2000) 403.
4) Miura T., et al., Nucl Instrum. Methods A **476** (2002) 337.
5) Ohuchi H., et al., Nucl. Sci. Technol. (Suppl.) **4** (2004).

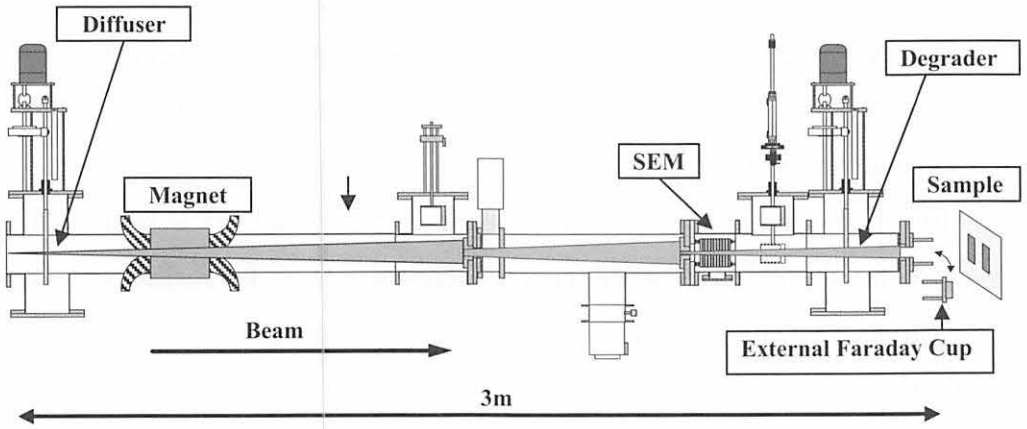

Figure 1. Ion irradiation apparatus.

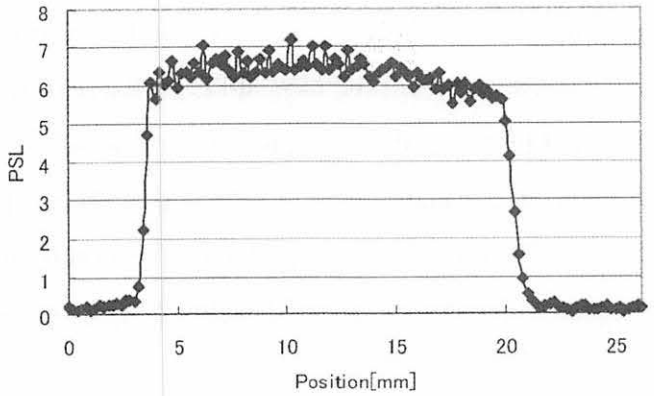

Figure 2. intensity distribution by using IP, Ne 131 MeV.

III. 5. Measurement of Secondary Heavy Charged Particle Spectrum by Tens of MeV Nucleons

Hagiwara M., Sanami T., Oishi T., Kamada S., Okuji T., and Baba M.*

Cyclotron Radioisotope Center, Tohoku University
**Radiation Science Center, High Energy Accelerator Research Organization (KEK)*

We have continued the development of experimental techniques for fragment detection. Spectrum data of fragments (charged particles heavier than helium) induced by tens of MeV nucleon are important in the field of the space technology and radiation dosimetry because of the high LET. The data of the fragment production, however, are very scarce except for the integral data by activation method because of the experimental difficulties for direct fragment detection, i.e., low yield, large energy loss in samples. Therefore, it is important to develop an experimental method suitable for the fragment measurement and to accumulate reliable experimental data.

For detection of fragment, we adopted 1) a Bragg curve spectrometer (BCS)[1,2] providing almost all information on the fragment with a single counter and 2) an energy-time of fight (E-TOF) method[3] having the capability of mass identification in almost whole energy region for fragments.

For proton induced reaction, BCS was improved at the part of entrance window to decrease the lower limit of the detection energy. We use an aluminized Mylar film (2.5 μm thick) supported by tungsten wire to act as not only entrance window but also as a cathode electrode simultaneously. With the BCS developed, the new measurements of proton-induced reaction were performed using 70 MeV protons at 31-1 course of CYRIC. For samples, foils of aluminum 2 μm thick and polypropylene 4 μm thick were employed. Figures 1 and 2 show the measured two-dimensional spectra on the energy *vs.* Bragg peak of fragments from 4 μm thick polypropylene and 2 μm thick aluminum, respectively. Excellent separation of each fragment and S/N ratio are confirmed up to Z = 6 (Carbon), 9 (Fluorine) for polypropylene and aluminum sample, respectively. In the method 2), the energy and TOF of the fragment is measured by SSD (silicon solid state detector) and Ultra

thin plastic scintillator (5 μm thick), respectively, and the mass number is derived by combing the energy, TOF and the energy loss information. The energy spectra of fragment heavier than alpha particle were obtained by both methods of BCS and E-TOF. Figure 3 shows the energy spectra of α-particle emitted to 30 degree from carbon and aluminum which were obtained with the BCS and E-TOF method. As shown in Fig.3, the data obtained with BCS and E-TOF method are consistent with each other in the overlapping region. The result of α-particle shows good agreements with LA150[4] except for the case of aluminum above 10 MeV. Figure 4 shows the energy spectra of fragments with mass number 6 obtained with E-TOF method. The present data for the mass number 6 agree with PHITS code[5], but not with LA150. Figure 5 and 6 show the energy spectra of beryllium from carbon and aluminum, respectively, at 30, 60 and 90 degree obtained with BCS. The present data show high angular dependence.

For neutron induced reaction, we designed a BCS[6] with special care to apply to neutron beam in the previous study and resulted in success first in the world to identify the fragments by neutron-induced reactions. Neutron data, however, was inferior to proton data because of mixing of particles with different directions from the sample on the cathode. In this study, an anode electrode with a segment pattern was newly adopted to the BCS as shown in Fig 7 to overcome the problem for inferior separation limit and uncertainty of the detector solid angle. The BCS was tested using a mixed α-source and fragments produced by 65 MeV quasi-monoenergitc neutron source[7] at 32-1 course of CYRIC. Besides, the solid angle obtained with the segmented anode was compared with calculation based on energy-range relationship. Using a calibrated α-source, good agreement among experimental and calculation for the detector efficiency was confirmed in Fig. 9. The signal selection with the segmented anode improves particle separation in lower energy region as shown in Fig.8 and Fig. 10.

References

1) Gruhn G.R. et.al., Nucl. Instrm. Meth. **196** (1982) 33.
2) Shenhav N.J. and Stelzer H., Nucl. Instrm. Meth., **228** (1985) 359.
3) Roche C.T. et al., Phys. Rev. C **14** (1976) 410.
4) Cadwick M. B. et al., Nucl. Sci. Eng., **1331** (1999) 293.
5) Iwase H. et al., J. Nucl. Sci. and Tech., **39** (2002) 1142.
6) Sanami T., Baba M., Saito K.and Hirakawa N., Nucl. Instrm. Meth., **A440** (2000) 403.
7) Okamura H. et al., this annual report.

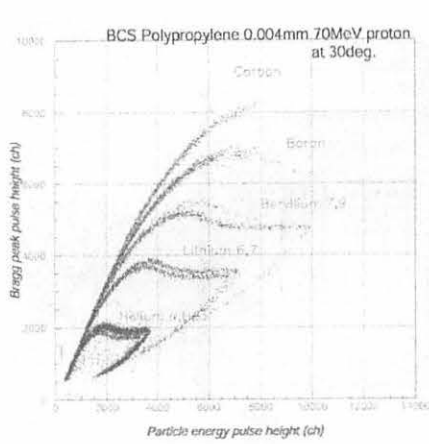

Fig. 1. energy *vs* Bragg peak two-dimensional spectra for polypropylene 4 μm thick sample.

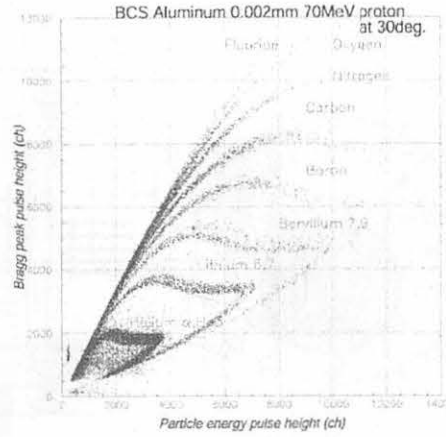

Fig. 2. energy *vs* Bragg peak two-dimensional spectra for aluminum 2 μm thick sample.

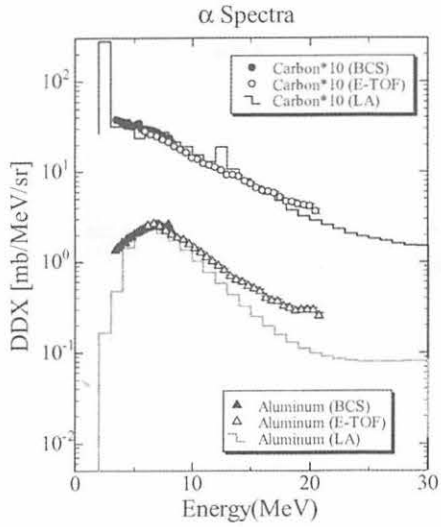

Fig. 3. DDX (alpha) at 30 degree compared with BCS and E-TOF method.

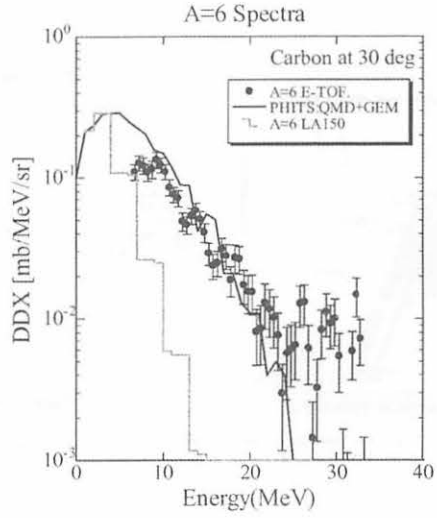

Fig. 4. DDX (mass 6) of p-C reaction at 30 degree compared with calculations.

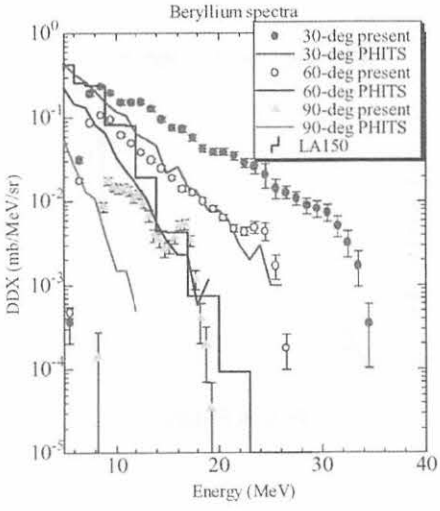

Fig. 5. C(p,x)Be DDX at 30, 60 90 degree compared with calculations.

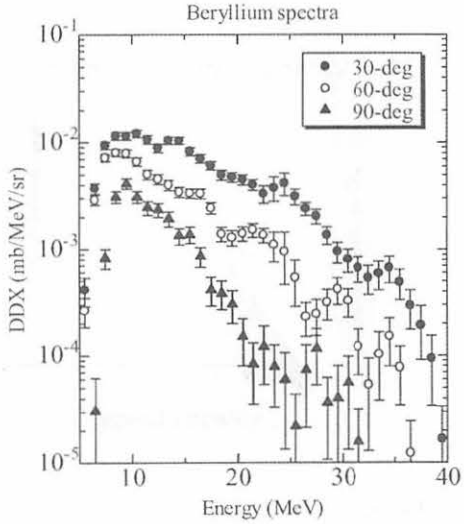

Fig. 6. Al(p,x)Be DDX at 30, 60 90 degree obtained with BCS.

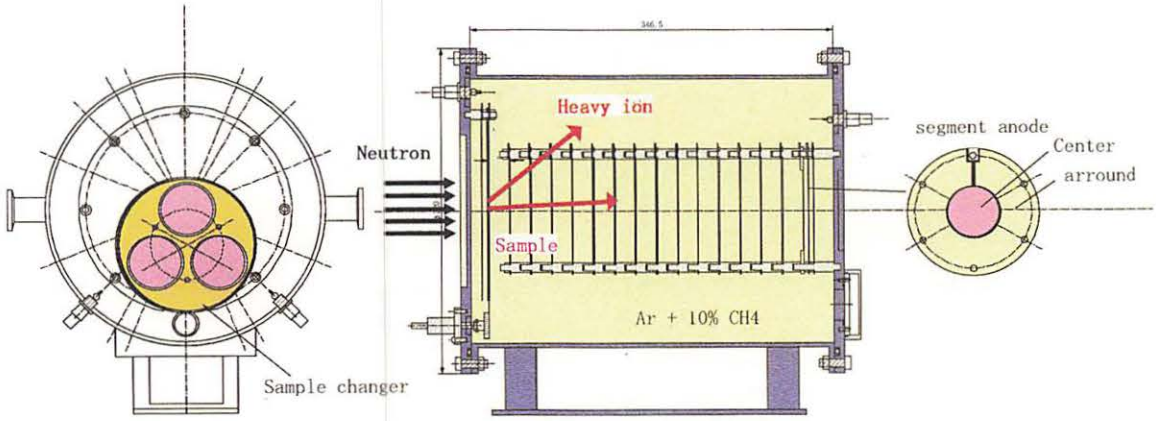

Fig. 7. Schematic view of Bragg curve spectrometer, segment anode electrode and sample changer.

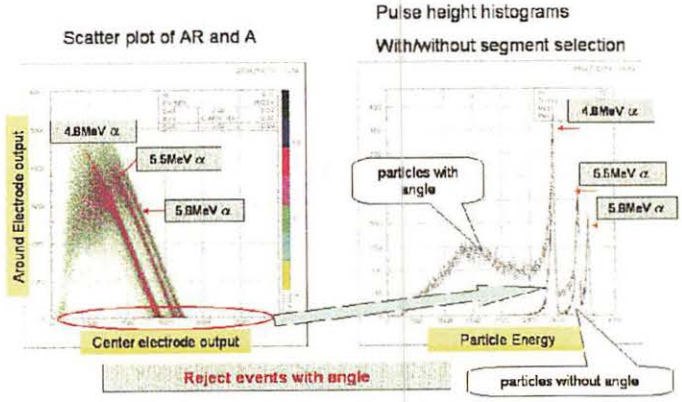

Fig. 8. Scatter plot of signals from center and around electrodes, and energy spectrum with and without rejection for mixed α-source.

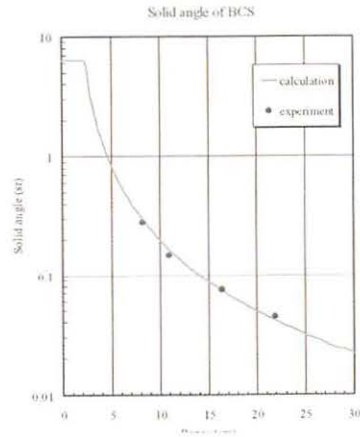

Fig. 9. Results of solid angle as a function of fragment range.

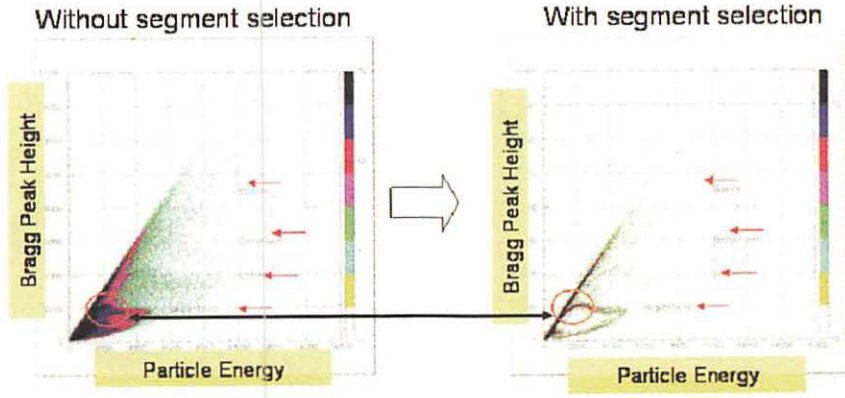

Fig. 10. Demonstration of improvement for secondary fragment identification by event rejection with segmented electrode.

III. 6. Experimental Studies on Particles-induced Activation

Uddin M.S., Baba M. and Hagiwara M.

Cyclotron and Radioisotope Center, Tohoku University

We have been conducting the experimental study on the production of radio isotopes useful for medical application, development of nuclear facility, wear study by thin layer activation (TLA) analysis, and also radionuclide production which results in the production of radioactive wastes. The measurements of *p*- and *d*-induced activation cross-sections on silver and yttrium were carried out in the frame of systematic investigation[1-7] of particles induced nuclear reactions on metals.

With review of the reported data, few problems have been picked up, which should be solved or upgraded the previous method to obtain higher precision experimental data. Experimental technique was reviewed and refined to improve the data accuracy. Then the method was applied to obtain systematic experimental data.

The independent and "cumulative cross-sections" of the *p*- and *d*-induced activation reactions on silver and yttrium were measured by using a conventional stacked foil activation technique. The silver and yttrium containing stacks were irradiated with 50, 70, 80 MeV protons and 40 MeV deuterons using a k=110 AVF cyclotron, Cyclotron and Radioisotope Center, Tohoku University, Sendai, Japan. The activities of the residual nuclides were measured nondestructively using HPGe gamma-ray spectroscopy.

Few results of cross-sections and thick target integral yields deduced from the present cross-section data are shown in Figs.1-4. The present data as shown in Fig.1 are for the production of medically used ^{103}Pd by direct reaction and *via* the decay of ^{103}Ag and ^{103}Cd of γ-ray measurement. The production cross-sections for ^{101}Pd and ^{100}Pd from ^{nat}Ag(p,x) at 70 MeV are larger than that of proton-induced activation on ^{103}Rh target[8] <20 MeV. The separation of these nuclides from ^{103}Pd is very difficult by chemical treatment. ^{101}Pd ($T_{1/2}$ = 8.47 h) decays out within few days of cooling time. The ^{100}Pd and ^{101}Pd production cross-sections are not so large. Thus, the ^{103}Pd production process *via* silver

involves a slightly higher impurity level of γ-ray emitting radionuclides than ^{103}Rh. The present data are useful for the optimization of the ^{103}Pd production with minimum radionuclidic impurity. The ^{nat}Ag(p,x) route seems to be profitable for the ^{103}Pd production.

The maximum ^{103}Ag production cross-section is about 2.5 times as low as the cumulative production of ^{103}Pd. The use of the short-lived ^{103}Ag as a precursor of the widely used ^{103}Pd in brachytherapy of prostate cancer is not a real alternative in comparison with the cumulative ^{103}Pd production from proton-induced activation on natural silver. In some special cases this route should be an option.

The half-life of ^{109}Cd ($T_{1/2}$=1.267 y) is significantly longer compared with other neutron deficient radioisotopes of this element, therefore the effects of the simultaneously produced radionuclides are not critical. The ^{109}Cd nuclide can be obtained in pure form only by maintaining few days cooling time. As shown in Fig.2 the cross-sections for the productions of ^{109}Cd is large and the ^{nat}Ag+d process can be a significant route for a large-scale production using accelerator.

As shown in Figs.3&4, the direct production of the ^{88}Y is low compared to ^{88}Zr for both *p*- and *d*-induced activation on yttrium target. Significant amount of ^{88}Zr can be produced at low energy accelerators by using yttrium target. The measured nuclear data can be effectively used for selection of optimal production routes. The expected thick target yields for the production of ^{88}Zr and ^{88}Y by proton and deuteron bombardment on yttrium target are very much higher than the Mo, Nb and Zr targets. Therefore, Y+p and Y+d are the efficient route to give large scale production of ^{88}Zr and ^{88}Y at low energy accelerator.

References

1) Uddin M.S., Hagiwara M., Tarkanyi F., Ditroi F., and Baba M., Appl. Radiat. and Isot. **60** (2004) 911.
2) Uddin M.S., Hagiwara M., Kawata N., Itoga T., Hirabayashi N., Baba M., Tarkanyi F., Ditroi F., and Csikai J., J. Nucl. Sci. Tech. Suppl. **4**, (2004) 160.
3) Uddin M.S., Hagiwara M., Baba M., Tarkanyi F., and Ditroi F.; Appl. Radiat. and Isot. (in press).
4) Uddin M.S., Hagiwara M., Baba M., Tarkanyi F., and Ditroi F.; Appl. Radiat. and Isot. (in press).
5) Tarkanyi F., Ditroi F., Takacs J., Csikai J., Mahunka I., Uddin M.S., Hagiwara M., Baba M., et al., ND2004, AIP Conference Proceedings (in press).
6) Uddin M.S., Hagiwara M., Tarkanyi F., Ditroi F., and M.Baba; JAERI-Conf 2004-005 (2004).
7) Uddin M.S., Hagiwara M., Baba M., Tarkanyi F., and Ditroi F; JAERI-Conf 2005-003 (in press).
8) Sudar S., Cserpak F., and Qaim S.M., Appl. Radiat. and Isot. **56** (2002) 821.

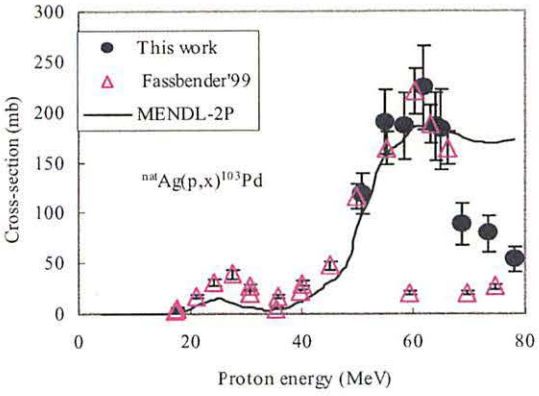

Figure 1. Excitation function of the $^{nat}Ag(p,x)^{103}Pd$ reaction.

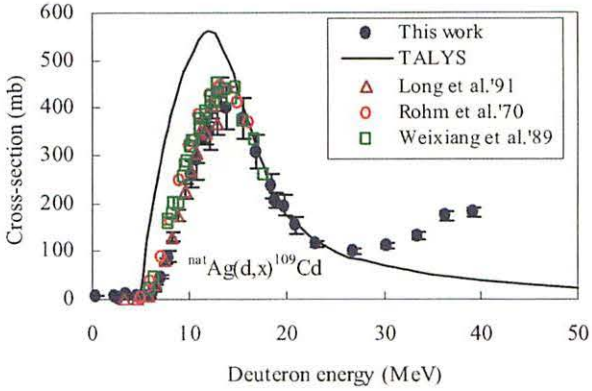

Figure 2. Excitation function of the $^{nat}Ag(d,x)^{109}Cd$ reaction.

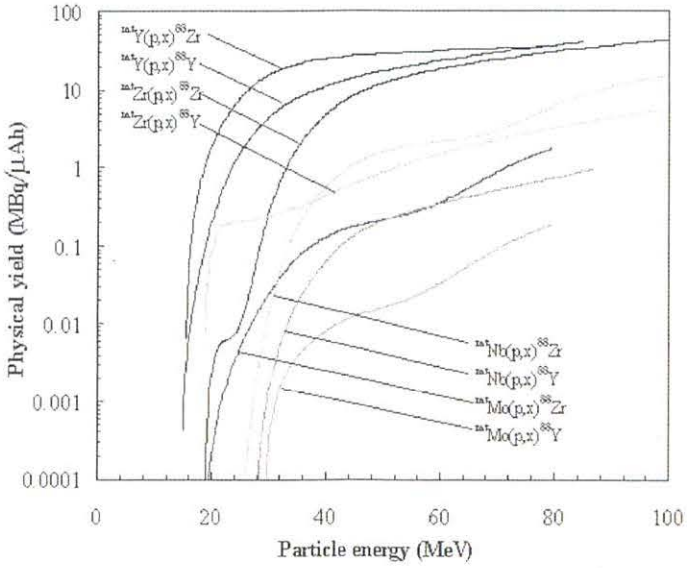

Figure 3. Physical yield of ^{88}Zr and ^{88}Y by *p*-induced activation on Y, Zr, Mo and Nb.

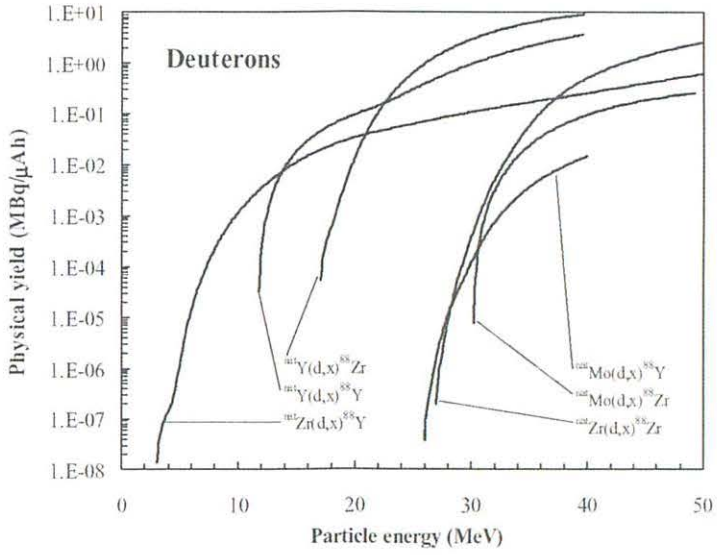

Figure 4. Physical yield of ^{88}Zr and ^{88}Y by *d*-induced activation on Y, Zr, Mo and Nb.

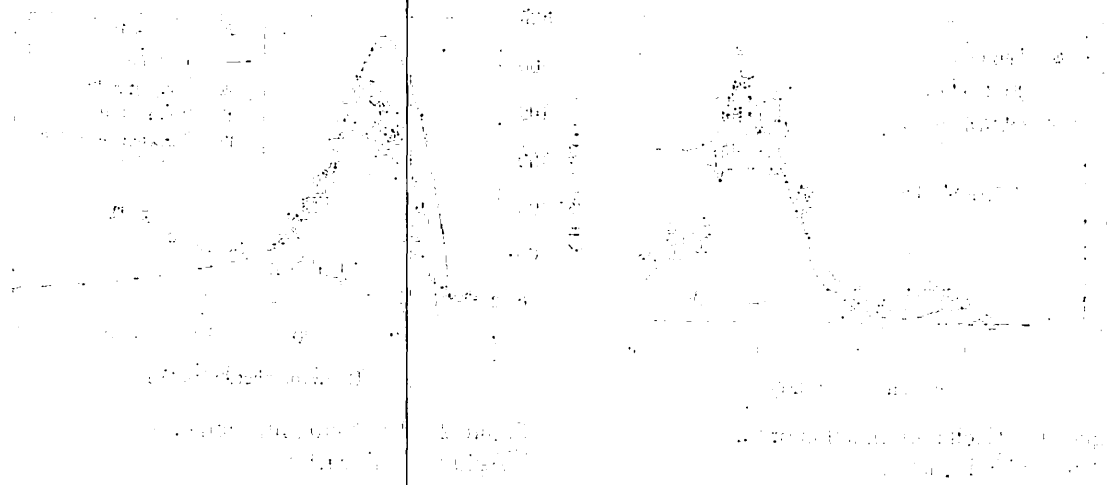

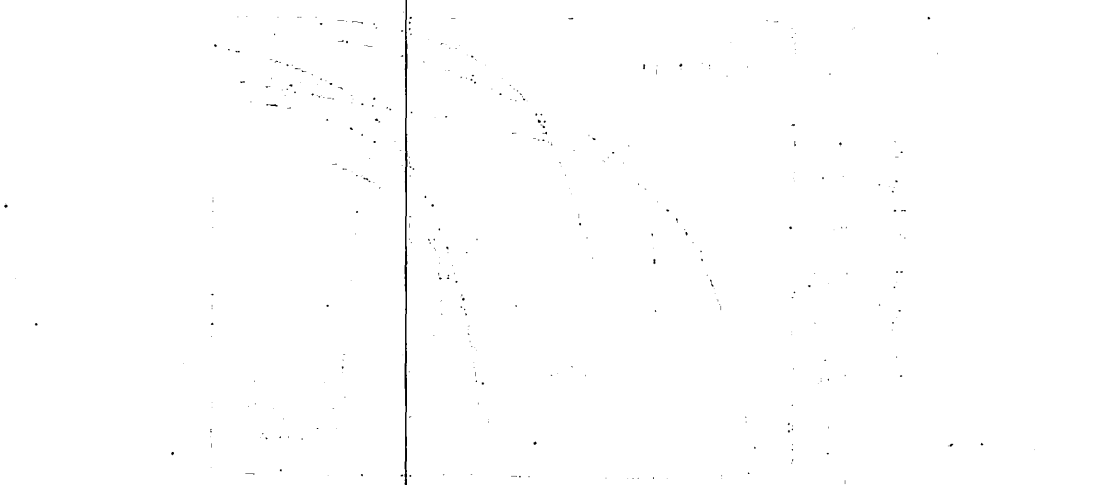

IV. NUCLEAR MEDICAL ENGINEERING

IV. 1. Skin Dose Measurement for Patients Using Imaging Plates in Interventional Radiology Procedures

Ohuchi H., Satoh T., Eguchi Y.*, and Mori K.***

Graduate School of Pharmaceutical Sciences, Tohoku University
**Department of Radiology, Yamagata University Hospital*
***Fuji Photo Film Co., Ltd.*

Introduction

Interventional radiology (fluoroscopically-guided) techniques comprisguided therapeutic and diagnostic interventions, by percutaneous or other access, usually performed with fluoroscopic imaging used to localize the lesion/treatment site, monitor the procedure, and control and document the therapy. The use of interventional radiology (IR) has greatly increased in recent years, because it offers several significant benefits[1]. However, prolonged fluoroscopy times and the cumulative X-ray doses delivered when making large numbers of radiographs of limited areas of the patient can cause deterministic effects ranging from transient erythema and dermatitis to skin necrosis[2,3].

Since most installations avoid high dose rates in the vicinity of the patient and staff by using fluoroscopy equipment configured with an over-table image intensifier and an under-table X-ray tube, the patient's skin dose can be mapped by placing a large piece of films on the tabletop immediately under the patient. Mapping skin doses using two-dimensional radiation sensors such as films is critical way to detect overlap areas between irradiation fields and determine the most-exposed patient skin areas and the probability of injury in complex fluoroscopy interventions. Kodak EDR2 film and new radiochromic film, GAFCHROMIC-XR can be used this way. However, their dynamic ranges are not adequate to fulfill the range of interest during IR procedures, from 10 mGy to over 10 Gy. Furthermore, films like EDR2 and radiochromic films cannot be reused.

We therefore propose to use imaging plates (IPs) for mapping skin doses of patients in IR procedures. An IP made of europium-doped BaFBr, a photostimulated luminescence (PSL) material, is a highly sensitive two-dimensional radiation sensor. It

has a wide dynamic range and high spatial resolution, and can be used repeatedly by irradiating them with visible light between uses. BAS-TR type IP can accurately measure X-ray doses ranging from 1 μGy to 100 Gy and the dose-response is linear up to about 10 Gy[4]. IPs show the same response in the range between 100 μGy/min and 3.73 Gy/min without a counting loss[5] and can thus be useful in IR procedures using high dose rates, such as digital subtraction angiography (DSA). Because the energy dependence of IPs is rather high, the IPs were characterized to have a sensitivity variation of about 13% was observed for effective energies of 32.7 to 44.7 keV[6], which are used in IR procedures. Simulation of actual interventional cardiology procedures showed that the variation of sensitivity was within 5%, meaning that IPs are practical for measuring skin doses during IR procedures[6].

In this work, the entrance skin dose (ESD) was measured in two clinical studies of transcatheter arterial embolization by fitting a large sheet of IPs around a patient's back using a corset, which was used to avoid a geometric discrepancy in dose estimate between IP and the patient body. The ESD obtained by IPs was compared with the results obtained by Dose Ace, which was commercially available a photoluminescent glass dosemeter.

Methods

Imaging plate and readout technique

The 20 cm x 40 cm BAS-TR type IP, manufactured by Fuji Photo Film Co., Ltd. was used. It has a 50 μm-thick photostimulable phosphor ($BaBrF:Eu^{2+}$) and has no protective surface layer. For measuring the ESD in patient, two IP sheets with closely matched sensitivities (within 5%) were coupled to make a 40 cm x 40 cm sheet for covering whole area of a patient's back. The IPs were wrapped in black polyethylene to shield them from sunlight during irradiation and put inside a corset to make IPs fit to the patient's back. The IPs were scanned within a few hours after irradiation, using a colored-cellophane technique[4,5] and a 200 μm x 200 μm BAS-1000 readout system (Fuji Photo Film Co., Ltd.), and were rescanned after annealing at 100°C for 70 hours.

Dose Ace

The GD-302M Dose Ace (Asahi Techno Glass Co., Japan) consists of a silver-activated photoluminescence glass dosemeter (PLD) chip. Each PLD chip was encapsulated within glass and was cylindrical, 1.5 mm in diameter and 12 mm in length. For each IR procedure, 10 points in the patient's back were selected for dose monitoring.

For each point, five PLD chips were used and placed inside the 13 mm x 14 mm holes that are present in the corset. The PL data from pulsed UV laser stimulation was read out from the chips with an FGD-1000 Dose Ace reader.

Corset

The corset consists of four 450 mm x 600 mm polyurethane sheets, three are 2-mm thick and one is 4-mm-thick. The 4-mm-thick sheet has 13 mm x 14 mm holes at 5-cm intervals in an 11 x 8 grid for placing the PLD chips inside. For measuring each patient's ESD, the IP was placed between two 2-mm-thick sheets and 50 PLD chips placed in the holes of the 4-mm-thick sheet on the reverse of the IP sheet. The structure of the corset and an arrangement of the IP sheet and PLD chips are shown in Fig. 1(a). The corset has three sets of Velcro bands on both sides to hold patient's body by fastening the ends of bands together. It can be easily worn and fit to the body as shown in Fig. 1(b).

X-ray irradiation

The IPs were irradiated by beams from the X-ray generator (KXO-2050, Toshiba Medical Co.,) at Yamagata University Hospital. The reference dosemeter was an ionization chamber (6 ml effective volume, model 1015, RADCAL Co.,), which is traceable to the Japanese national standard maintained by the JQA. The filters for the X-ray generator were 1.1-mm-thick Al plus 0.03-mm-thick Ta. The effective energies varied between 32.7 and 44.7 keV when the tube voltage was varied between 60 and 120 kV. The dose-response of PLD chips in the range from 1 mGy to 2 Gy was evaluated by placing four PLD chips at every irradiation on the tabletop immediately under an acrylic phantom (i.e., entrance skin location) and providing the X-ray beam from under the table with using tube voltages of 60, 80, 100, and 120 kV. The acrylic phantom was 20-cm-thick and had a 33 cm x 33 cm front face. Each exposure was determined with the RADCAL ionization chamber model 1015 by placing chamber in the center of IPs and PLD chips.

Results and discussion

The variation of the measured values among four PLD chips at each irradiated dose or tube voltage was within about 5%. The PLD chip dose–response relations are shown in Fig. 2 for each tube voltage. The linearity was observed for all the doses at all tube voltages, and the response of the PLD was equal from 80 kV to 120 kV although sensitivity

at 60 kV was about 10% less than that at other voltages.

Case 1 and 2 were 68 and 77-year-old female patients each with Hepatocellular Carcinoma (HCC), which were treated by Transcatheter arterial embolization (TAE). Fluorocsopy times were about 1 hr and 2 hr, individually and tube voltages were recorded at 3 min intervals during fluoroscopy. A contour dose map of patient 2 obtained by scanning of IPs with the annealing technique is shown in Fig. 3(a). Ten measuring points where PLD chips were placed were shown in Fig.3(b). An example of ESD monitoring of patient 2 obtained by the PLD chips and IPs at the same point is given in Table 1. Although the variation among PLD chips was within about 5%, the estimated dose by PLD chips at points 4, 8, and 9 showed 2.5, 1.6, and 1.9 times variation among 5 chips. IP's dose distributions in Fig.3(b) clearly showed that these points were located just on the places where the dose changed sharply. Overall, both doses in Table 1 show agreement, however, the doses obtained with the PLD chips were consistently lower than those obtained with the IPs. The highest dose among ten points was observed at point 7 and the difference between the dose obtained with the PLD chips and that with IPs was more than 40%. This discrepancy partly comes from the absorption of the X-rays by the IPs, which was estimated to be 7.7% at a tube voltage of 80 kV, since the PLD chips were placed on the reverse side of the IP sheet against the X-ray generator. It also comes from a variation of sensitivity of the PLD chip, whose sensitivity depends on the direction from which the X-rays are incident on a PLD chip. The X-rays come from the direction along a long axis of a PLD chip have about 60% of the sensitivity of those come from the direction along a short axis[7,8] when tube voltages are 50, 80, 100, and 140 kV. An area including peak skin dose (PSD) can be easily recognized visually by variations of PSL density in Fig. 3(a), however, the PSD area cannot be recognized from the results obtained by discrete numbers of PLD chips.

References

1) Society of Interventional Radiology. *What are the advantages of interventional radiology?* Available at://www.sirweb.org/patPub/whatIsAnIR.s.html. Accessed May.7 (2005).
2) Vano E., Arranz L., Sastre J.M., Moro C., Ledo A., Garate M.T., and Minguez I., Br. J. Radiol. **71** (1998) 510.
3) Faulkner K. and Vano E., Radiat. Prot. Dosim. **94** (2001) 95.
4) Ohuchi H. and Yamadera A., Nucl. Sci. Technol. **Suppl. 4** (2004) 140.
5) Ohuchi H. and Yamadera A., Hokenbutsuri **39** (2005) 198.
6) Ohuchi H., Satoh T., Eguchi Y., and Mori K., Radiat. Prot. Dosim. (in press)
7) Komiya I., Shirasaka T., umezu Y., Tachibana M., and Izumi T., Nippon Hoshasen Gijutsu Gakkai Zasshi **60** (2004) 270.
8) Technical Information from ASAHI TECHNO GLASS CORPORATION (2000).

Table 1. Comparison of entrance skin dose, ESD (mGy) of patient 2 at the same point obtained by the PLD chips and the IPs.

Measuring Points	ESD obtained by 5 PLD chips (mGy)	ESD obtained by IPs (mGy)
1	16.66 ~ 21.23	19.99 ~ 22.51
2	14.87 ~ 17.85	18.49 ~ 19.79
3	5.37 ~ 6.41	10.29 ~ 10.86
4	389.91 ~ 992.88	398.12 ~ 1,124.83
5	113.50 ~ 134.96	94.43 ~ 192.01
6	12.99 ~ 13.68	19.01 ~ 21.23
7	990.29 ~ 1,029.60	1,099.08 ~ 1,602.81
8	265.54 ~ 429.47	444.75 ~ 679.27
9	113.89 ~ 216.8	115.46 ~ 260.57
10	12.46 ~ 13.22	17.56 ~ 19.27

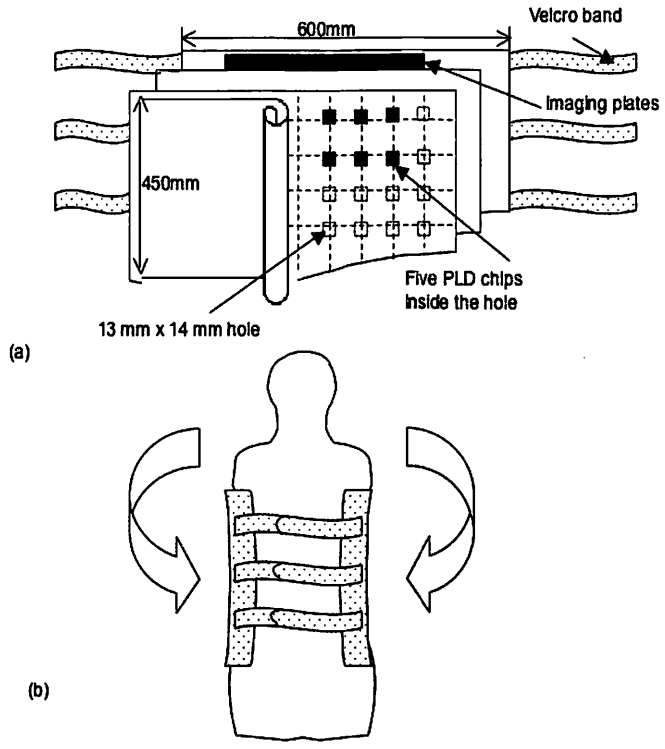

Figure 1. (a) Structure of the corset and an arrangement of IP sheet and Photoluminescence glass dosemeter (PLD) chips. (b) Patient's body are held by fastening the ends of Velcro bands together. It can be easily worn and fit to the body.

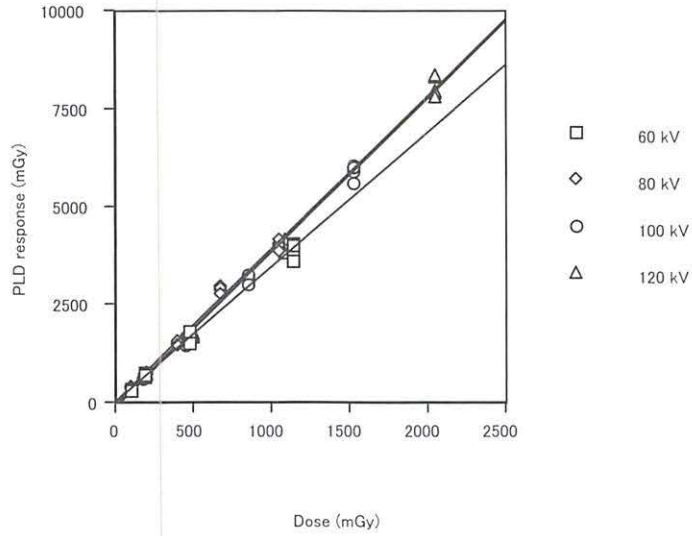

Figure 2. PLD chip dose-response relations on the acrylic phantom for the tube of 60, 80, 100, and 120 kV.

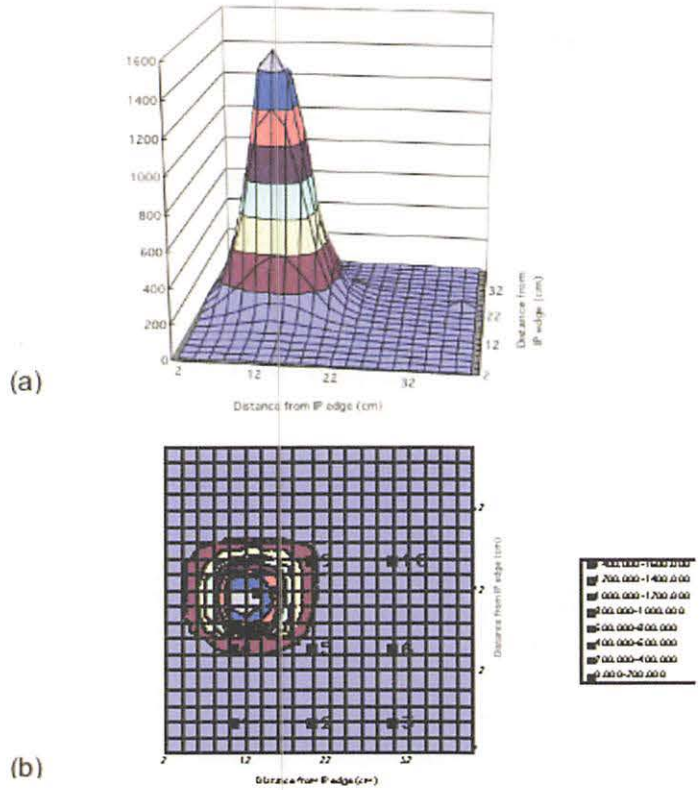

Figure 3. Contour dose map of patient 2 obtained by scanning of IPs. (a) 3-D map. (b) 2-D map. Ten measuring points were selected for dose monitoring with PLD chips. For each point, five PLD chips were placed.

IV. 2. Estimating Effective Energies and $H^*(10)$ of Scatters in Diagnostic X-ray Rooms Using Imaging Plates

Ohuchi H., Jutou N.[*], *Satoh T.*[**], *Eguchi Y.*[**], *Sasaki T.*[***], *and Baba M.*[***]

Graduate School of Pharmaceutical Sciences, Tohoku University
[*]*Chiyoda Technol Corp.*
[**]*Yamagata University Hospital*
[***]*CYRIC Tohoku University*

Introduction

Interventional radiology (IR) offers an opportunity to treat a greater range of pathologies, in more patients and at lesser cost and reduces the need for expensive operating suites and extended hospital in-patient admissions[1]. While the use of IR has greatly increased in recent years, reports of radiation-induced injuries to patients' skin have steadily increased since the early 1990s[2,3]. Patients are not the only people at risk. IR procedures are specialities in which staff can be exposed to significant occupational radiation risks. Staff doses correlate with patient doses, in that higher patient doses result in an increased amount of scattered radiation in the interventional suite. There are significant contributions to the scatter from materials in the suite other than the patient. Dose to staff such as radiologist, nurse, and radiological technologist might vary largely according to not only the nature of the work but also their positions in the procedure. The scatter has a variety of energies, thus, estimating the effective energies of X-rays should be important for evaluation of directional dose equivalent, $H^*(10)$. In this study, the effective energies of X-rays in a diagnostic X-ray room were estimated by using imaging plates (IPs) with three different metal filters and $H^*(10)$ was evaluated.

An IP made of europium-doped BaFBr, a photostimulated luminescence (PSL) material, is a highly sensitive two-dimensional radiation sensor. In the X-ray energy range, their sensitivity greatly depends on the photon energy because the photostimulable phosphor is composed of elements having relatively high atomic numbers. The effective energy, therefore, could be distinguished into a small keV step by using energy-response relations obtained by taking the ratios of the sensitivities data of different metal filters. In

the application of IPs to dosimetry, fading causes serious problems, however, an appropriate post-irradiation annealing procedure allows to mnimize the effect of fading, and quantitative estimation of the radiation dose is possible[4-6]. The values of $H^*(10)$ were determined by using the effective energies and the results were compared with those obtained using a response having a flat energy dependence by taking the weighted sum of the sensitivities data measured using three metal filters.

Methods

Commercially available IPs, BAS-MS (BAS-MS2025), manufactured by Fuji Photo Film Co. were used. The IP consists of 9-μm thick protective Mylar film and 115-μm thick photostimulable phosphor affixed to a 188-μm thick plastic backing. It is a highly sensitive, waterproof IP. A 4.5 cm x 4.5 cm piece of IP material was prepared as a single IP element by cutting each sheet. IP's responses to X-rays in air with effective energies of 30–120 keV, which covered the X-rays energies range used in IR procedures, were investigated using the X-ray generator at the Japan Quality Assurance Organization (JQA) in Tokyo, Japan. The IPs were irradiated with three metal filters and without a filter. A set of filters comprising aluminum (Al) (Z=13) sheets 0.3, 0.5, and 1.0 mm thick, copper (Cu) (Z=29) sheets 0.1 and 0.3 mm thick, and cadmium (Cd) (Z=48) sheets 0.5 and 1.0 mm thick was attached to each surface of the plate. IP's responses to ^{137}Cs gamma rays in air were investigated using a ^{137}Cs point source (0.238 mGy/hour at 1 m on Dec. 11 2003 and gamma emission energy of 0.662 MeV) at the Cyclotron and Radioisotope Center (CYRIC) of Tohoku University. Each exposure dose on the IP was fixed at 60 μGy, which was measured with a 100 ml ionization chamber, Exradin model A5 at JQA and a 800 ml ionization chamber, Exradin model A6 at CYRIC. After irradiation, the IPs were left inside an incubator kept at 15°C for 24 hours and then scanned by using a 200 μm x 200 μm BAS-1000 readout system (Fuji Photo Film Co., Ltd.).

Interventional radiological procedures and cardiacangiography are performed in two diagnostic X-ray rooms at Yamagata University Hospital. In both rooms, the procedures are performed with the X-ray tube under the examination couch. The room, where the interventional cardiology is frequently performed, is equipped with an X-ray generator (KXO-100G, Toshiba Medical Co.,), provided with biplane positioners with frontal and lateral C-arms. The filters for the X-ray generator were 1.1-mm-thick Al plus 0.03-mm-thick Ta for fuluoroscopy or 1.5-mm-thick Al for radiography. The effective

energies varied between 34.2 and 46.9 keV for fuluoroscopy and 31.0 and 42.3 keV for radiography when the tube voltage was varied between 60 and 120 kV.

For estimating the effective energies of scatters, each set of an IP with filter set was placed at three points inside the room. Point 1 was on the surface of a lead shield, which hangs from the examination couch to protect a cardiologist's waist from exposure. The IP was placed on the outside the shield. Point 2 was on the surface of the wall near the examination couch, 1.5 m above the floor. At point 3, the IP was placed on the surface of the wall in the corner of the room 1.5 m above the floor, where nurses often are on standby. During irradiation, the IPs were wrapped in black polyethylene to shield them from sunlight. After 27 days, the IPs were collected, annealed at 80°C for 24 hours by keeping IPs inside an incubator (SANYO, MOV-112P2), then scanned with BAS-1000. The values of the ratios of two sensitivities data in each combination of different metal filters and different thicknesses on specific tube voltage were obtained by irradiating the primary beam with the X-ray generator on a set of an IP with filter set in air at tube voltages of 60, 80, 100, and 120 kV in radiography mode.

Results and discussion

Six variations of energy-response relations were obtained by taking the ratios of two sensitivities data by combining different metal filters and different thicknesses. The combinations are 0.5-mm-thick Al/0.1-mm-thick Cu, 0.5-mm-thick Al/0.3-mm-thick Cu, 0.5-mm-thick Al /0.5 -mm-thick Cd, 1.0-mm-thick Al / 0.5-mm-thick Cd, 0.1-mm-thick Cu / 0.5-mm-thick Cd, and 0.3 -mm-thick Cu / 0.5-mm-thick Cd, as shown in Fig.1. All sensitivities data were normalized by the sensitivity data measured using ^{137}Cs gamma rays. The effective energies of scatters can be estimated by applying the results measured by the IP with a filter set into these relations. Among six relations, one obtained by taking the ratios of the sensitivities data of 0.1-mm-thick Cu and 0.5-mm-thick Cd has bigger difference between 30 keV and 120 keV than other relations. Relations by taking the ratios of the sensitivities data of Al and Cd also show rather big difference, however, aluminum filters can not make any difference in PSL density between with a filter and without a filter in rather high X-rays energy range above 80 kV as shown in Fig.2(a), which exhibits relative PSL sensitivities measured with and without aluminum filters of three different thicknesses for X-rays with effective energies of 30 - 120 keV. Thus, the relation obtained from the ratio of the sensitivities data of 0.1-mm-thick Cu and 0.5-mm-thick Cd was chosen for estimating the effective energies of scatters. The values of the ratios of two sensitivities

data at tube voltages of 60, 80, 100, and 120 kV were obtained to be 38.0, 13.0, 8.3, and 6.1, respectively. By using Cu/Cd relation, the values of the effective energies corresponded with these values of the ratios were read as 42, 52, 58, and 62.5 keV. The variation of the effective energies of the X-ray generator at Yamagata University Hospital is from 31.0 to 42.3 keV for radiography at the tube voltages from 60 to 120 kV. The discrepancy between these two values of the effective energies might come from the difference of the X-ray spectrum of the X-ray generator between at JQA and at Yamagata University Hospital. A difference of the effective energies of scatters could be distinguished into less than 0.5 keV step by using Cu/Cd relation, because significant difference in the values of the ratios is estimated to be 1.0 step. The effective energies of scatters in a diagnostic X-ray room were, thus, estimated 40.3, 32.3, and 27.8 keV at point 1, 2, and 3, respectively. Using values of the effective energies and the sensitivity data without a filter measured at JQA, the values of $H^*(10)$ were calculated to be 0.20, 4.28, 0.20 mSv, respectively.

By combining the sensitivities data measured using 1.0-mm-thick aluminum, 0.1-mm-thick copper, and 0.5-mm-thick cadmium filters (in Figures 2(a), 2(b), and 2(c)), a constant PSL sensitivity of an IP independent of the effective X-ray energy can be obtained. By taking the weighted sum shown in Equation 1, a response having flat energy dependence can be obtained as shown in Figure 2(d),

$$Res_{sum} = 1.1Res_{Al}-0.98Res_{Cu}+0.85Res_{Cd}\,, \qquad (1)$$

where Res_{Al}, Res_{Cu}, and Res_{Cd} are, respectively, the IP sensitivities measured with 1.0-mm-thick aluminum, 0.1-mm-thick copper, and 0.5-mm-thick cadmium filters. All sensitivities data were normalized by the sensitivity data measured using ^{137}Cs gamma rays.

Figure 2(d) shows that the IP sensitivity so obtained was constant to within 8% variation for X-rays with effective energies less than 80 keV. The values of $H^*(10)$ were evaluated to be 0.30, 4.02, and 0.28 mSv at point 1, 2, and 3, respectively, which show good agreement with the results of $H^*(10)$ evaluated by determining the effective energies.

References

1) International Commission on Radiological Protection (ICRP). ICRP Publication 85. (Ann. ICRP **30** (2)) (Oxford: Pergamon Press) (2000).
2) Vano E., Arranz L., Sastre J.M., Moro C., Ledo A., Garate M.T., and Minguez I., Br. J. Radiol. **71** (1998) 510.
3) Faulkner K. and Vano E., Radiat. Prot. Dosim. **94** (2001) 95.
4) Ohuchi H., Yamadera A., and Baba M., Radiat. Prot. Dosim. **107** (2003) 239.

5) Ohuchi H., Yamadera A., and Baba M., Radioisotopes **53** (2004) 115.
6) Ohuchi H. and Yamadera A., J. Nucl. Sci. Technol. Suppl. **4** (2004) 140.

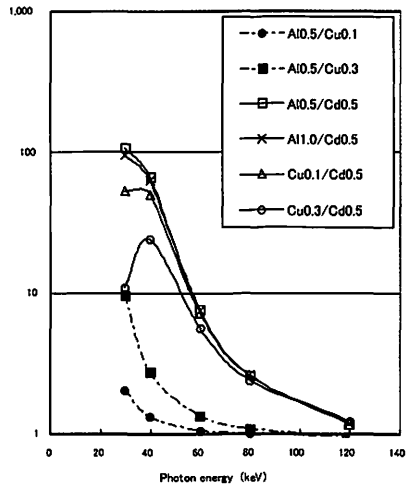

Fig. 1. Energy-response relations obtained by taking the ratios of two sensitivities data by combining different metal filters and different thicknesses.

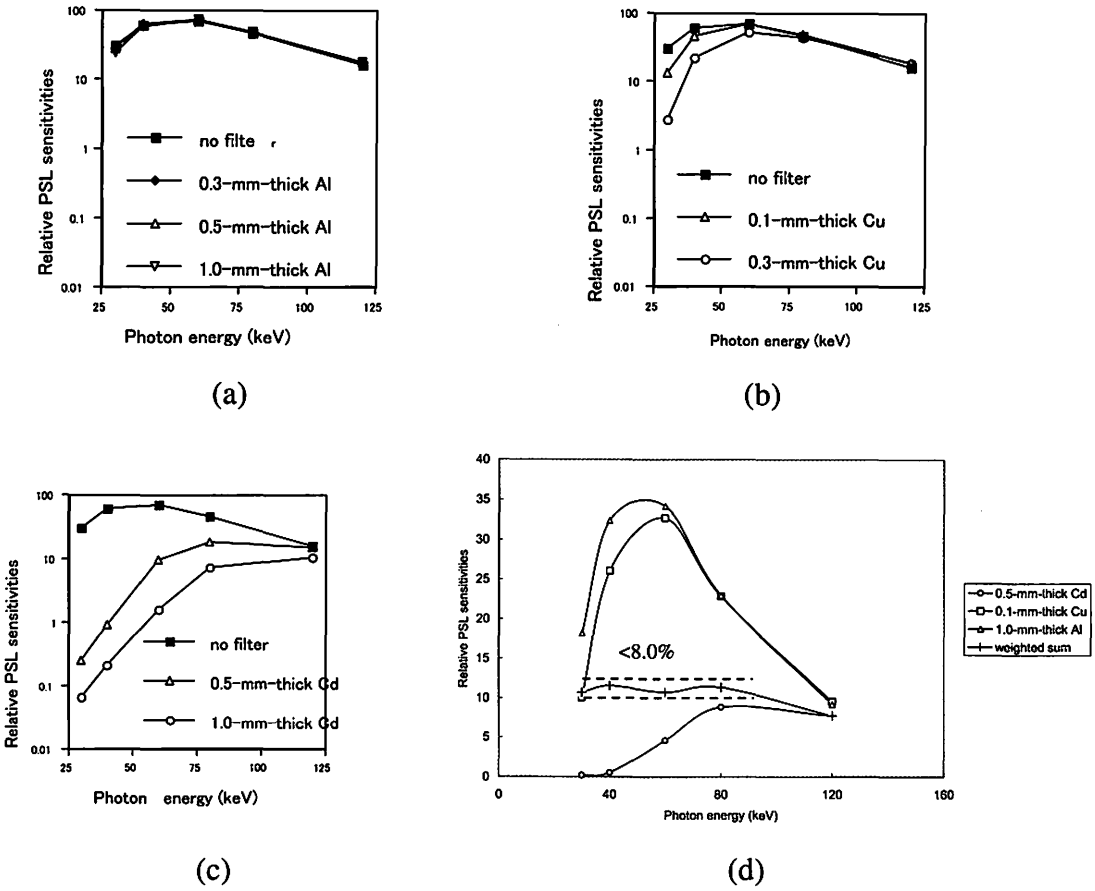

Fig. 2. Relative PSL sensitivities, which are normalized by the sensitivity data measured using ^{137}Cs gamma rays, measured with and without (a) aluminum, (b) copper, and (c) cadmium filters of different thicknesses. The + symbols in part (d) show the weighted sum of relative PSL sensitivities combined three sensitivity data with different metal filters.

IV. 3. Development of Image Reconstruction Technology for Ultra High-resolution PET and Micron-CT

Yamaguchi T., Ishii K., Yamazaki H., Matsuyama S., Kikuchi Y., Momose G., YamamotoY., and Watanabe Y.

Department of Quantum Science and Energy Engineering, Tohoku University

ABSTRACT

The development of high spatial resolution PET is vital for testing new medicines on small animals. We are developing "Dual Head PET" with high resolution and high sensitivity, whose detectors are in two arrays facing each other. The "Dual Head PET" provides incomplete projection data and the FBP algorithm is not suitable. On the other hand, a prototype of Micron-CT for biological research is being developed at Tohoku University. This Micron-CT uses a point X-ray source with a spot size of 3 μm and an X-ray CCD with 1000×1000 pixels of 8 μm×8 μm, achieving spatial resolutions of the order of micro-meter. The event data obtained by the X-ray CCD is statistically poor at practicable scanning time and the 3D FBP algorithm is not suitable because it is highly sensitive to statistical noise. Hence, we applied the Expectation-Maximization (EM) algorithm for image reconstruction and developed an image reconstruction method for Dual Head PET and Micron-CT. We demonstrated PET ant CT images, which were reconstructed the simulated data measured with Dual Head PET and the experimental data measured with Micron-CT.

INTRODUCTION

X-ray CT (Computed Tomography) was invented by G. Hounsfield and J. Ambrose in 1979. Now, a Cone-beam is being used for CT scan. After the invention of the CT scanner, Filtered Back Projection (FBP) algorithm incorporated into an analytical technique is usually used as the main method for the image reconstruction algorithm. For image reconstruction method with cone-beam, the Feldkamp method[1] is widely used now. This is FBP weighted by taking into account the cone angle. On the other hand, an algebraic

technique was devised for the image reconstruction method. The algebraic technique in Positron emission tomography has been widely studied since Shepp and Vardi[2] developed a method based on expectation maximization (EM) algorithm. K. Lange and R. Carson applied the EM algorithm to X-ray CT[3]. In comparison with FBP, the Signal-to-Noise ratio of images could be improved considerably. However, EM method has two disadvantages. Firstly, it is time consuming and secondly when projection data include noise, the solution diverges as the EM iterative procedure is implemented. To overcome the first disadvantage, acceleration methods to reduce the computational time have been proposed and the recent trend focuses on the use of block-iterative methods. One acceleration method is the ordered subsets (OS) EM algorithm (Hudson and Larkin[4]). In OSEM, projection data are grouped into a number of subsets, and the EM iterative procedure is repeatedly adopted for each subset until all subsets have been processed. To resolve the second shortcoming, various stopping rules are proposed. For instance, cross validation algorithm was used as a stopping rule[5]. In this algorithm, the projection data is divided into two groups and EM algorithm is applied to one data set. The Poisson likelihood of the reconstructed image is calculated with the other data set. When it is maximized, the EM iteration is stopped. The other stopping rule is Kontaxakis's stopping rule[6]. This rule stops the EM iteration when the image updating remains a constant. Maximum *'A posteriori'* (MAP) algorithm was devised as the image reconstruction method to stabilize EM reconstructed images with priori information for images[7]. When a projection data set is acquired, this method finds a solution that maximizes the conditional probability on images. This solution converges when the iteration number is increased. Considering poor statistical accuracy in X-ray CCD data obtained by practicable data acquisition time, hence, we applied the EM algorithm for image reconstruction to Micron-CT. To reduce computation time, OSEM algorithm was applied to the image reconstruction.

Meanwhile, research activity in PET instrumentation is largely dedicated to obtaining high spatial image resolution[8,9]. When the spatial resolution is better than 1mm, several resolution-limiting factors have to be taken into account in order to achieve the desired intrinsic resolution. These are essentially detector size, angular deviation and positron range. The influence of positron range is ignored here since the FWHM of the positron distribution is less than 0.2mm for ^{18}F-labeled radiopharmaceuticals. A scintillator detector is realized a limitation of miniaturizing it, so a thin Semiconductor detector improves the spatial resolution degradation caused by detector size. The solution for avoiding the degrading effect

of angular deviation lies in shortening the distance between opposite detector rows. In order to achieve high spatial resolution images, we are developing "Dual Head PET" by arranging a thin CdTe in two rows facing each other at short distance. This detector arrangement allows to reduce the effect of angular deviation and increases the overall scanner sensitivity. EM and MAP algorithm was chosen to reconstruct the data sets measured by Dual Head PET. In addition, Depth of Interaction (DOI) information improves the degradation of spatial resolution caused by parallax error, so that it is programmed in process of the reconstruction.

MATERIALS AND METHODS

For Dual Head PET, *Maximum A Posteriori* (MAP) algorithm is applied to the image reconstruction to improve reconstructed images[10-12]. MAP can remove the divergence in quantitative accuracy at higher iteration numbers often seen in EM due to noise. MAP updates the voxel value $\lambda_b{}^n$ by

$$\lambda_b{}^{n+1} = \frac{\lambda_b{}^n}{\sum_{d=1}^{D} p_{bd}\left(1+\frac{1}{\beta}\frac{\partial U(\lambda_b{}^n)}{\partial \lambda_b{}^n}\right)} \sum_{d=1}^{D} \frac{n_d p_{bd}}{\sum_{k=1}^{B} \lambda_k{}^n p_{kd}} \qquad (1)$$

where p_{bd} is the probability that γ-rays generating in the bth voxel are measured with the dth detector pair, n_d indicates the detected event in the dth detector pair,

$$\frac{\partial U(\lambda_b{}^n)}{\partial \lambda_b{}^n} = \sum_{l \in N_b} \varpi_{bl} \frac{\partial V(r,\delta)}{\partial r} = \sum_{l \in N_b} \varpi_{bl} \frac{16(r/\delta)}{\left(3+(r/\delta)^2\right)^2} \qquad (2)$$

and N_b is "cliques" which are defined by voxel b and voxels l next to b. The clique energy $V(r,\delta)$ is a function of the difference r between the values of two voxels b and l. The constant ω_{bl} is a weighting factor between voxels b and l. The parameter δ controls the effect of the energy function, and parameter δ determines the location of the derivative energy function peak with respect to r. In this study, the values of ω_{bl} were fixed at 1 and the value of δ was set to 100. When the parameter δ is kept constant during reconstruction, MAP has a noise-suppression effect on only one region. We assumed that voxel values followed a Poisson distribution. Hence the parameter δ was set to $2\sigma = 2\sqrt{voxelvalue}$. We compared the image with MAP (δ=*const*) algorithm and that of MAP (δ=*variable*).

For Micron-CT, Gradient algorithm is applied, which belongs to the group of EM methods. Gradient algorithm updates the voxel value $\mu_j{}^n$ by;

$$\mu_j^{n+1} = \mu_j^n \cdot \frac{\sum_{i=1}^{I} d_i \cdot \exp\left(-\sum_{j=1}^{J} l_{ij} \cdot \mu_j^n\right) \cdot l_{ij}}{\sum_{i=1}^{I} y_i \cdot l_{ij}} \qquad (3)$$

where l_{ij} is the intersection length for X-rays passing through the jth voxel in the ith projection, y_i is the number of detected events for the ith projection and d_i is the expected number of photon counts emerging from the source along the ith projection. l_{ij} is weighted to be able to reconstruct a 3D object with the incomplete data.

Figure 1 shows the simulation geometry of Dual Head PET. Monte Carlo method is used in order to simulate coincidence data sets for a pair of Dual Head PET. The measurement is simulated with 32 CdTe-crystals in 2 layers that is 4 arrays of 1.2×1.2×3 mm^3. The distance between detector arrays is 50 mm. Figure 2 shows digital phantoms. Phantom 1 consists of an uniform disc and two circular hot areas. The warm background and the hot discs have relative emision activities of 1 and 5, and diameters of 30 mm and 6 mm, respectively. Phantom 1 has 0.2 M total counts. Phantom 2 consists of an uniform disc, a lower right cold disc, two circular hot areas and a upper left sharp spot. The warm background, the cold disc, the upper right hot disc, the lower left hot disc and the sharp spot have relative emision activities of 1, 0, 1.5, 2 and 5, and diameters of 30 mm, 8 mm, 6 mm, 6 mm and 0.7 mm, respectively. Phantom 2 has 0.5 M total counts. We performed MAP reconstruction with 63×63×1 voxels of 0.7 mm×0.7 mm×0.7 mm in the field of view. The computation time was less than 1 min per 10 iteration on a DELL Precision PWS670 Workstation 3.2GHz.

Figure 3 shows the geometry of Micron-CT. This Micron-CT uses a point X-ray source with a spot size of 3 μmϕ and an X-ray CCD of Hamamatsu photonics Co. Ltd (C8800X) with×1000×1000 pixels of 8 μm width×8 μm height. Monochromatic X-rays permeating a sample are characteristic Ti -K-X-rays (4.558 keV) produced by 3MeV proton micro beams. In Our Micron-CT system, source and detectors are fixed and the sample is turned. 250 projection data are acquired par 360°, which acquisition time par 1 projection is about 8 sec. Figure 4 shows the light-microgram of a biological sample for Micron-CT, which is a ant's head of 1mmϕ. We performed OSEM (5 subset) with 456×456×360 voxels of 2.5 μm×2.5 μm×2.5 μm in the field of view. The computation time was about 12 hour per iteration on a DELL Precision PWS670 Workstation 3.2 GHz. In this case, l_{ij} was calculated when needed, because it was too much to store the intersection length l_{ij}.

RESULT AND DISCUSSION

Figure 5 shows the PET images reconstructed Phantom 1 with EM and MAP algorithm. These images are at the 30th iteration. MAP (δ=*const*) has δ and β of 875 and 100, respectively. In comparison with EM image, it is clear that the noise is strongly suppressed in the MAP images. MAP (δ=*const*) has a noise-suppression effect on only hot regions, while MAP (δ=*variable*) has a noise-suppression effect on both warm and hot regions.

Figure 6 shows the PET images reconstructed Phantom 2 with EM and MAP (δ=*variable*) algorithm. These images are at the 30th iteration. In respect of Phantom 2, MAP ($\delta=2\sigma$) was not able to reconstruct the sharp spot. So we performed the reconstruction with MAP that the value of β was set to 0.5σ. MAP ($\delta=0.5\sigma$) provided the noise suppression and the high spatial resolution. Thus it is necessary to investigate the most suitable coefficient of δ.

Figure 7 shows the CT images reconstructed the ant's head with OSEM algorithm, in which OS level is 5. These images are at the 4th iteration. With our Micron-CT, only slice with the source is acquired as complete projection data, and other slices are acquired as incomplete projection data. Nevertheless most slices were reconstructed with EM algorithm.

CONCLUSIONS

We developed an image reconstruction method for Dual Head PET and Micron-CT using EM algorithm.

MAP algorithm was applied to Dual Head PET. When the parameter δ is set to $2\sigma = 2\sqrt{voxelvalue}$, the shape of the energy function $V(r,\delta)$ is suitable for all regions. Hence it is possible to suppress the noise in both warm and hot regions on Phantom 1. On the contrary, the sharp spot was not reconstructed on Phantom 2. Thus we will study the most suitable coefficient of δ.

OSEM algorithm was applied to Micron-CT. This image reconstruction method obtains a three-dimensional image by using the cone-beam without helical scan. Most slices were well reconstructed. In addition, when data possess low statistical accuracy, the image reconstructed with EM algorithm is much improved a better Signal-to-Noise ratio in comparison with FBP. In this study, because the micro-tube of 25 μm could be reconstructed, the CT image of a cell (30 μm) will be acquired in the future.

ACKNOWLEDGEMENTS

This study was supported by 21 COE Program "Future Medical Engineering based on Bio-nanotechnology" and a Grant-in-Aid for Scientific Research (S) No. 13852017 (K. Ishii) of the Ministry of Education, Culture, Science, Sports and Technology

References

1) Feldkamp L.A., Davis L.C., and Kress J.W.,: J. Opt. Soc. Am. A. **1** (1984) 612.
2) A.Shepp L. and Vardi Y., IEEE Transactions On Medical Imaging, **MI-2** (1982) 113.
3) Lange K. and Carson R., JCAT **8** (1984) 306.
4) Hudson H.M. and Larkin R.S., IEEE Trans. Med. Imag. **13** (1994) 601.
5) Selivanov V.V., Lapointe D., Bentourkia M., and Lecomte R., IEEE Trans. Nucl. Sci. **48** (2000) 883.
6) Kontaxakis G. and Tzanakos G., Confer. Rec. IEEE Nuc. Sci. Symp. Me. Imag. Confer. **2** (1992) 1163.
7) Levitan E. and Herman G.T., IEEE Trans. Med. Imag. **MI-6** (1987) 185.
8) Moses W.W., Nucl. Instrum. Methods in Phys. Res. **A 471** (2001).
9) Rutao Y., Seidel J., Johnson C.A., Daube-Witherspoon M.E., Green M.V., Carson R.E., IEEE Trans. Med. Imag. **19** (2000).
10) Lalush D.S. and Tsui B.M.W., IEEE Trans. Med. Imag. **11** (1992) 267.
11) Ohura N., Ogawa K., and Kunieda E., Bul. Comput. Sci. Res. Center, Hosei University **13** (2000).
12) Lange K. and Fessler J.A., IEEE Trans .Med. Imag. **MI-6** (1987) 185.

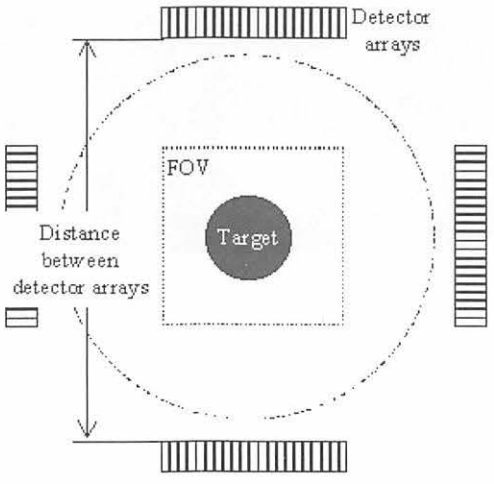

Figure 1. The simulation geometry of Dual Head PET.

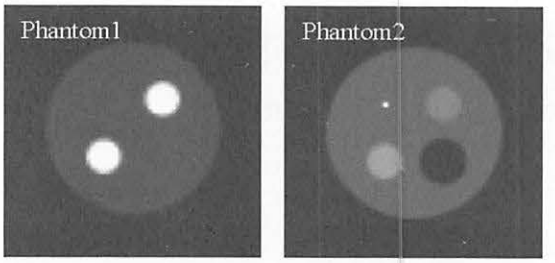

Figure 2. Digital phantoms for Dual Head PET.

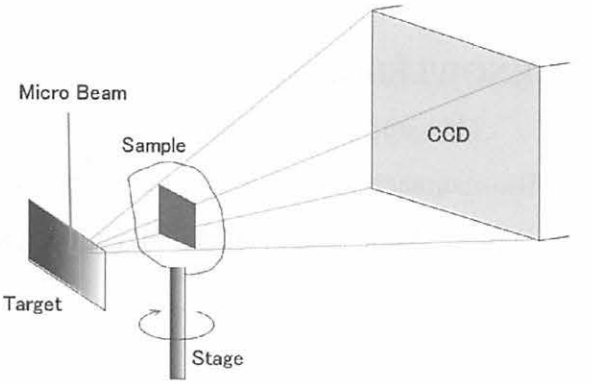

Figure 3. The geometry of Micron-CT.

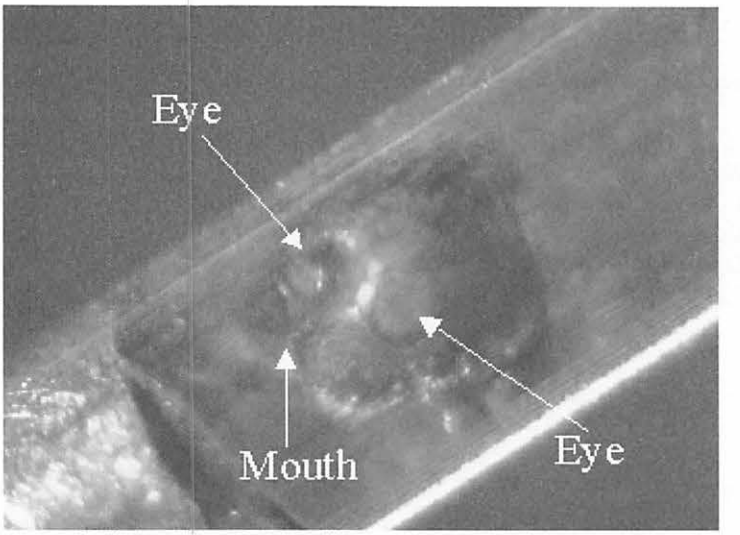

Figure 4. The biological sample (ant's head 1mmϕ) for Micron-CT.

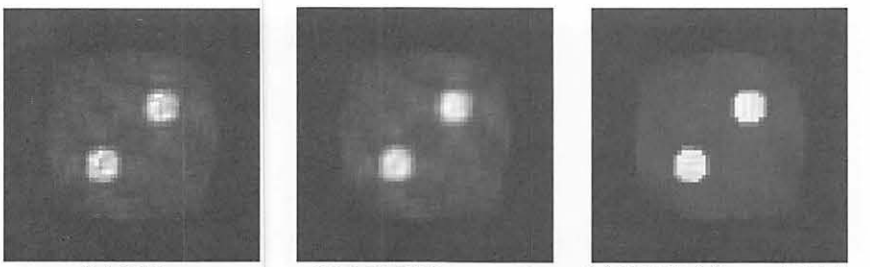

(a) EM (b) MAP(δ =const) (c) MAP (δ =variable)

Figure 5. PET reconstruction images of Phantom 1.

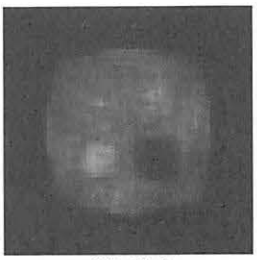

(a) EM

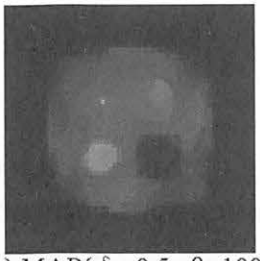

(b) MAP(δ =0.5σ,β=100)

Figure 6. PET reconstruction images of Phantom 2.

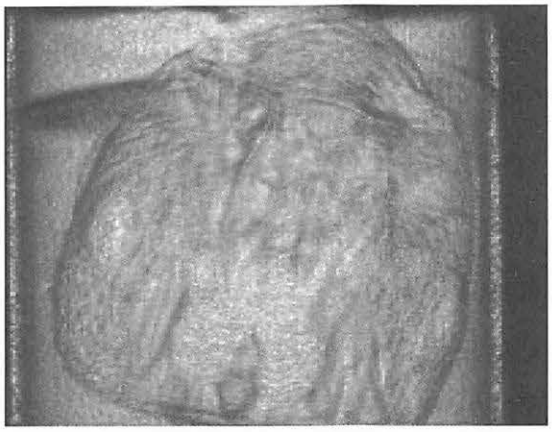

(a) The volume rendering image of the ant's head.

(b) The maximum intensity projection image of the ant's head

Figure 7. CT reconstruction images.

IV. 4. Study on Spatial Resolution of PET Camera Using Semiconductor Detector

Kikuchi Y., Ishii K., Yamazaki H., Matsuyama S., Yamaguchi T., and Yamamoto Y.

Graduate School of Engineering, Tohoku University

Introduction

PET is a technique that acquires functional image of tissues by injecting positron labeled medicine into objects. Usually, PET cameras contain radiation detectors arranged circularly (gantry). Two back-to-back photons, which derive from annihilation of positron-electron pair, are measured coincidently by detectors, and image is reconstructed by the measured data.

Mainly, PET is used in clinic. Moreover, PET is applied in fields of biology and pharmacology. Objects in these fields are small experimental animals like mice, rats and so on. Because high spatial resolution PET camera is needed in these animal applications, PET cameras for animal, whose gantry diameter is smaller, has been developed and commercialized. Resolution of these PET cameras is about 2mm, but higher resolution camera is demanded.

Physical limitation of resolution is determined by two factors, positron range and fluctuation of emission angle between two back-to-back photons[1]. The limitation is below 1mm in case that positron range of label nuclide, for example ^{18}F, is short. Resolution of PET camera also depends on detector size, adding to two factors abovementioned. If detector size is smaller than another two factors, influence of detector size can be neglected. Thin detector is useful to reduce influence of detector, but in conventional PET camera using scintillation detector this way cannot be adopted because fluorescence intensity decreases before reach to photo-detector and output signal become small.

We propose use of semiconductor detector for PET instead of scintillation detector. Output signal from semiconductor detector is independent of detector size. From our previous research, it was determined that CdTe (cadmium telluride) semiconductor detector,

whose atomic number was high (Cd: 42, Te 52), was suitable for application of PET and high resolution could be achieved by using small semiconductor detectors[2].

We are planning to develop prototype of semiconductor PET camera. In this study, we made dual head gantry system containing a pair of movable detector units, and we investigated resolution and sensitivity of the gantry for design of the prototype.

Materials and Methods

a) Dual head gantry system

It is necessary that influence of detector alignment on resolution is investigated for developing high resolution PET camera. First, dual head gantry was made by placing a pair of movable detector units oppositely.

32-ch CdTe detector array shown in Fig. 1 is adopted as detector for the gantry. This detector array is obtained by dividing the surface electrode of a semiconductor crystal and detectors are packed densely (size per channel 1.2 mm (1.4 mm pitch) x 1.1 5 mm x 4.5 mm). Energy resolution of these detectors is 3% (FWHM) for 511 keV and time resolution is about 5 nsec (FWHM).

A detector unit is made by placing the array in aluminum case. A pair of the detector units is installed in movable stage. With movable stage, detector units can be rotated and moved to both radial direction and transaxial direction, so that gantry diameter and FOV are changeable.

Signals from detector unit are amplified, pulse-shaped and time-picked off by NIM modules. Next, signal is converted to digital data and stored by PC based CAMAC data acquisition system. Because the data acquisition system also controls movement of gantry, information about position of detectors is involved to the acquired event data. After measurement, reconstructed image is obtained by the data.

b) Radioactive source and Phantom

With the dual head gantry system, ^{22}Na point source and ^{18}F phantom were measured. Size of the ^{22}Na point source, embedded in acrylic disk, is 0.6 mm diameter and its activity is 1.6 MBq. ^{18}F phantom is acrylic cylinder penetrated by tube whose inside diameter is 0.5 mm. Radioactivity distribution shown in Fig. 4 is formed by filling tube with ^{18}F solution in section of the phantom. Resolution can be estimated by identifying each spots in reconstructed image.

Experimental Setup

With rotating the detector pair, angular data samples (0, 45, 90, 135 degree) were acquired. ^{22}Na point source was measured gantry at 50mm and 150mm distance between detector units of the gantry in order to assume small gantry diameter like commercial animal PET camera. In the measurement, eight detectors of each the detector array were used.

In measurement of ^{18}F, twenty-four detectors of the each the detector array were used at 100 mm distance between detector units. FOV of 33.4 mm could be covered by moving detector units to transaxial direction during the measurement. Measurement period at initial position of the detector units was 5 min, and at following each position, period was extended to keep statistical uniformity at each position. Concentration of ^{18}F solution was 7.2 mCi/ml.

Reconstructed images

Reconstructed image of point source at 150 mm distance between detector units and profiles at 50 mm and 150 mm distance are shown in Figs. 5 and 6. Generally, influence of angular fluctuation is proportional to gantry diameter, but there is no difference in FWHM of profile between 50 mm distance and 150 mm distance. FWHM is about 1.0 mm. It is supposed that high resolution below 1 mm can be achieved with PET camera whose gantry diameter is by 150 mm, however resolution cannot be concluded from point source images because width of profile may be affected by image reconstruction. About 150 mm diameter gantry is available for application to larger animals than mice, for example rats.

Image of ^{18}F is shown in Fig. 7. Spots in the image are blurred somewhat, but each spot is identified in profile (Fig. 8). The profile of the phantom image indicates that resolution below 1 mm can be achieved clearly. Because it has been confirmed that resolution is uniform at 50 mm to 150 mm gantry diameter from the point source study, image to be equivalent can be obtained at 150 mm gantry diameter in phantom study.

Blurring of the image may be caused by statistical problem or fine shift of detector array alignment.

Estimation about sensitivity of prototype

Sensitivity is important parameter. Sensitivity of the prototype semiconductor PET camera was simulated. GATE (GEANT4 Application for Tomographic Emission),

simulation tool for Nuclear Medicine, was used. Assumed prototype PET camera is composed of detector units aligned circularly and detector units are made by detector arrays stacked.

a) Validity of Simulation

First, simulation to be equivalent to the ^{18}F phantom measurement was compared with the measurement in order to investigate validity of simulation. When LLD was 250 keV and ULD was 650 keV, total counts in the measurement were 86 % of the simulation counts.

b) Simulation condition

Assumed detector size was 1.2 mm x 1.15.mm x D (mm) (D = 5, 10, 15, 20, 25, 30 mm) and detector array included twenty-eight detectors with 1.4 mm pitch. Detector units were composed of the detector arrays stacked with 1.4 mm pitch to axial direction (layer number: L = 8, 16, 24). The detector units were aligned octagonally and point source was located at CFOV (Center of FOV).

c) Results

Result of simulation (Fig. 9) indicates relation of the detector depth (D mm) and layer number of the array (L) to absolute sensitivity. Sensitivity of commercial animal PET camera is several percents, for example in Micro PET R4 (Concorde Inc.) about 3 %[3]. When the R4 is referred and difference between the phantom study to simulation is considered, calculated sensitivity of the prototype is not inferior to commercial camera's sensitivity at L = 24 and D = 20 mm, however the axial FOV is narrow. Generally, depth of animal PET camera's detectors is about 10 mm and shorter than whole body PET. This is in order to avoid decrease of resolution in edge of gantry, caused by DOI effect. In case of semiconductor PET, several detectors can be aligned to radial direction, so that there is possibility to avoid the effect without additional techniques like use of phoswich detectors[4].

Conclusion

Detector alignment and sensitivity were investigated for design of prototype of high resolution semiconductor PET camera. It was supposed that spatial resolution below 1 mm was achieved at 150 mm diameter gantry that can be applied in study to rats. Sensitivity may be obtained commercial animal PET camera by thickening total depth of

detector. We guess that high resolution and sensitive prototype camera can be developed.

References

1) Budinger T., and Brennan M., Nucl. Med. Biol. **23** (1996) 659.
2) Kikuchi Y., Ishii K., Yamazaki H., Matsuyama S., Yamaguti T., Yamamoto Y., Sato T., Aoki Y., and Aoki K., Nucl. Instrum. Methods B, in press.
3) Knoess C., Siegel S., Smith A., Newport D., Richerzhagen N., Winkeler A., Jacobs A., Goble R., Graf R., Wienhard K., and Heiss W., Eur. J. Nucl. Med. **30** (2003) 737.
4) Liu H., Omura T., Watanabe M., and Yamashita T., Nucl. Instrum. Methods B **459** (2001) 182.

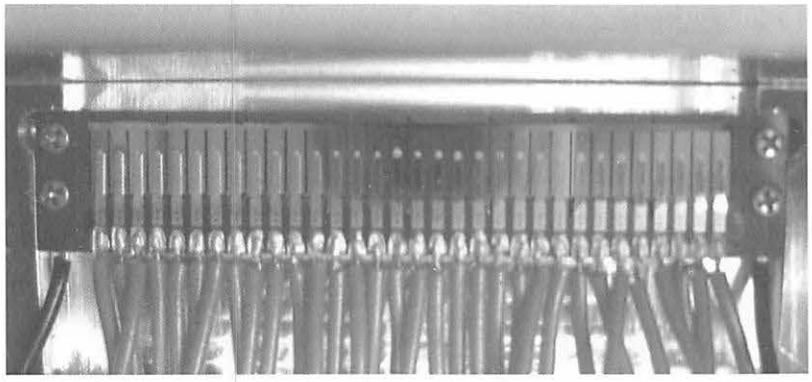

Figure 1. The picture of 32 ch CdTe detector array. The 32 ch detector array is composed of eight CdTe crystals and each crystal is divided into four sections.

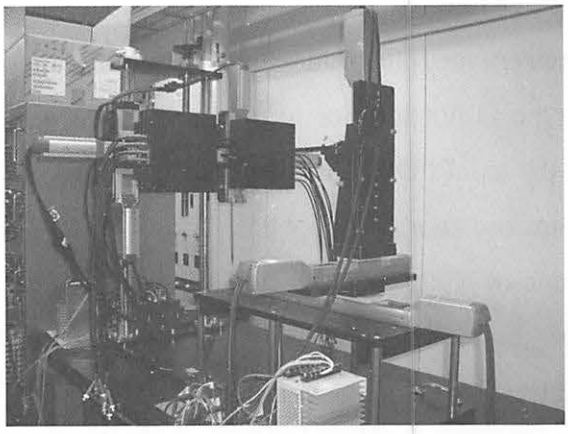

Figure 2. The dual head gantry system.

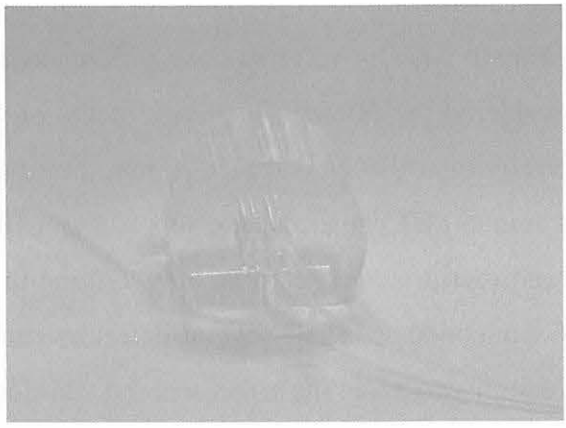

Figure 3. The picture of ^{18}F phantom.

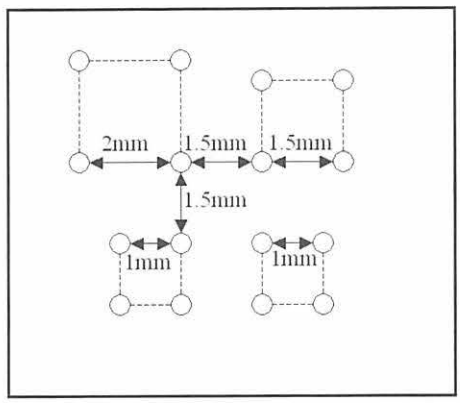

Figure 4. Schematic arrangement of hot spots in ^{18}F phantom.

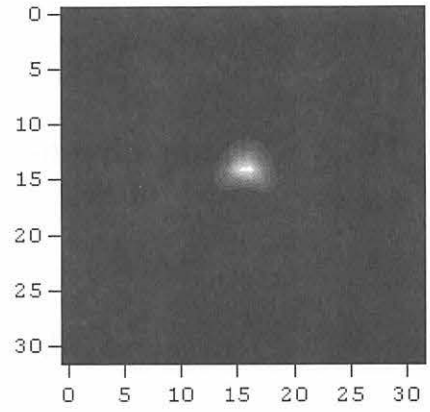

Figure 5. Reconstructed image of ^{22}Na point source.

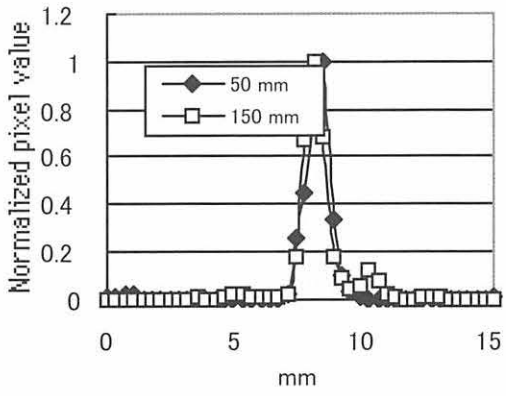

Figure 6. Profile of point source image.

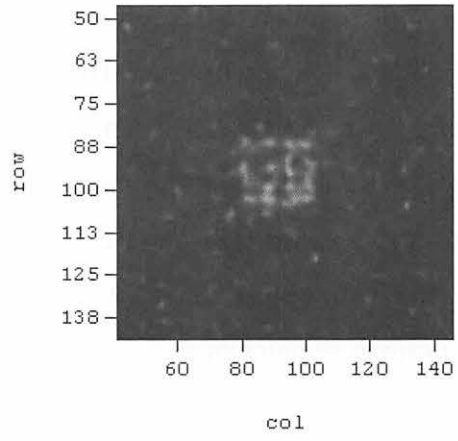

Figure 7. Reconstructed image of ^{18}F phantom.

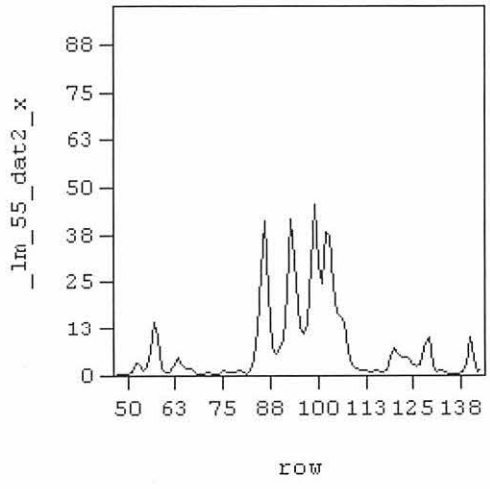

Figure 8. Profile of phantom image along axis in Fig. 7.

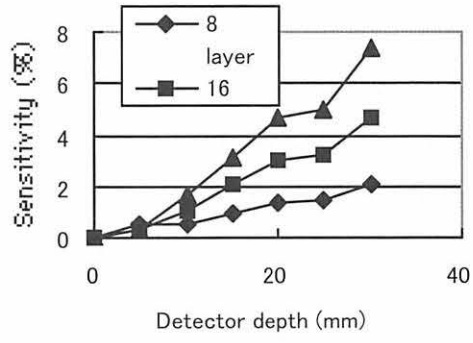

Figure 9. Simulated sensitivity of the prototype of semiconductor PET.

IV. 5. Examination of Aging in Sensitivity and Resolution of SET-2400W PET Scanner

Watanuki S., Miyake M., Tashiro M., and Itoh M.

Cyclotron and Radioisotope Center, Tohoku University

Introduction

A PET scanner (SET-2400W, Shimadzu Co., Kyoto Japan)[1] has been used at CYRIC, Tohoku University over 10 years. Although the scanner has been maintained periodically, its sensitivity has been successively degraded year by year. Since a detector system of the scanner was overhauled in August 2004, the scanner sensitivity has been well-recovered. Since a PET system is required durability of performance in aspects of a reliable examination and a cost, it is important to detect an aging of the system and to perform a proper maintenance. Although there are many previous reports on performance evaluation of a PET system, the reports on aging and effectiveness of maintenance of a PET system is hardly available. In the present report, results of our evaluation on aging of our PET system are presented and discussed.

Material and methods

Specifications and a diagram of SET-2400W detector system are shown in Figure 1. SET-2400W scanner has 448 detector blocks that consist of 6 x 8 BGO crystal arrays with 4 photo-multiplier tubes (PMTs). Positions of gamma ray incident crystals in a crystal array and incident photon energy are determined by four PMTs outputs, a linear correction table and an energy correction table. Therefore stability of gain and balance of PMTs are important for the determination of position and energy. Degradation of PMTs gain and balance causes deterioration of sensitivity and resolution of a PET system. It was likely that the sensitivity and resolution will deteriorate according to an aging of the detector system, then sensitivities and resolutions were examined at different time points for assessment of the aging.

Sensitivities in 2D mode scan were obtained from the system calibration data that were measured periodically from 1998 to 2004. The calibration data were measured by using a 25-cm-long cylindrical phantom with 20-cm-long diameter which was filled with 7 to 32 MBq solution. The sensitivity was defined as a total slice count rate at 1 MBq/phantom. The relative slice sensitivity (at slice 3-61) was also defined as a count rate of each slice at 1 MBq/phantom. The relative slice sensitivity was measured in 1995 and before/after overhaul in 2004. Initial sensitivity was defined by the sensitivity that was measured in accordance with a previous publication from National Electrical Manufacturers Association (NEMA) in 1994 (NEMA NU2-1994 standatd: in short, N-94 standard)[2]. Sensitivities according to the N-94 standard were also measured at just before and after the overhaul for verifying equivalence between the sensitivity value by calibration measurement and by N-94 measurement.

Transaxial resolution was measured at 0, 5, 10, 15 and 20 cm from FOV center using a line source. The measurement was carried out in 1995, 2002 and after the overhaul in 2004. A stainless steel tube filled with ^{18}F solution was used for the line source. Differences of maintenance items between an overhaul and a regular maintenance of SET-2400W are summarized in Table 1.

Results

Figure 2 shows variation of sensitivity of the scanner with years. The values with N-94 standard sensitivity measurement were plotted by open circle. Sensitivity values measured by N-94 are same as the value obtained by calibration at before and after the overhaul. The compatibility of measurement between the calibration and the N-94 measurement was confirmed by this agreement. Sensitivity had degreased year by year before the overhaul in spite of a performing of regular maintenance. Sensitivity measured in 1994 was 842 cps/MBq/phantom and sensitivities measured before and after the overhaul in 2004 were 458 and 785 cps/MBq/phantom, respectively. The sensitivity became approximately a half of the initial value within 10 years, but that was well-recovered by the overhaul.

Figure 3 shows the relative slice sensitivity in 2D scan mode. Variances of the slice sensitivities (slice 3-61) in 1995 and before and after the overhaul in 2004 were 0.11, 0.16 and 0.08, respectively. The variance before the overhaul was much larger than the other values, and peaks and valleys were visible only in the variance curve before overhaul in 2004. Figure 4 shows the resolution in 1995, 2002, and after the overhaul in 2004.

The resolutions before the overhaul were not visually distinguished from those measured in 1994 and after the overhaul in 2004.

Discussion and conclusion

It turned out that the sensitivity of the scanner considerably degraded with aging. It was thought that this degradation was mainly a result of decrease in a PMT gain. The PMT gain was not only tuned in the overhaul but also in regular maintenance. Since the sensitivity was decreased constantly before the overhaul and was recovered after the overhaul, it was thought that the regular maintenance failed to manage the degradation of all detectors.

The slice sensitivity variance was increased with aging and was recovered by the overhaul. If four PMT gains are not balanced, an incident crystal position shift to a edge of crystal block in a result of error with linear correction table. Since the valleys in the slice sensitivity curve match with borders of detectors, it was thought that an error of positioning happened by unbalance of PMT gains. However, an effect of the error was not observed in the result of resolution measurements. Positions of crystal which concerned with the line source position varies in a detector block, while an image slice keeps a fixed relationship with a crystal in a detector. Therefore, we assumed that the resolution is not affected by the positioning error.

The scanner sensitivity and the uniformity of slice sensitivity were considerably deteriorated by the degradation of PMTs gain and balance with aging. These deteriorations were well recovered by the overhaul. An appropriate overhaul is important to keep a scanner performance. But it is desired that a regular maintenance cloud care for these deteriorations.

References

1) Fujiwara S., Watanuki S. et. al, Ann. Nucl. Med. **11** (1997) 397.
2) National Electrical Manufacturers Association. NEMA NU-2 Standards Publication NU-2-1994: performance measurements of positron emission tomography, 1994.

Table 1. Objective detector and tuning items at overhaul and a regular maintenance of SET-2400W.

	Regular maintenance	Overhaul
Objective detector	Out of conditions	All
Tuning items	PMT gain PMT balance Timing	PMT gain PMT balance Timing Linear correction table Energy correction table

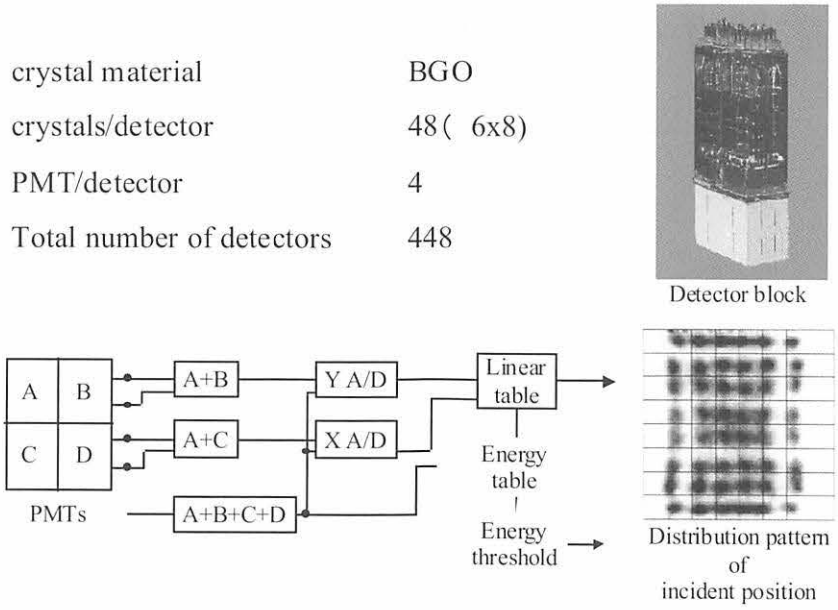

Figure 1. Specification and diagram of SET-2400W detector system.

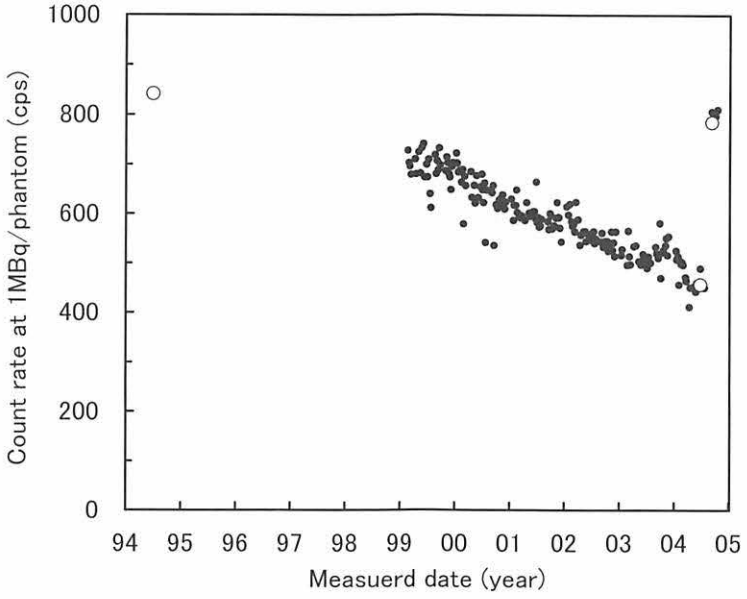

Figure 2 Variation of sensitivity of the scanner with years.

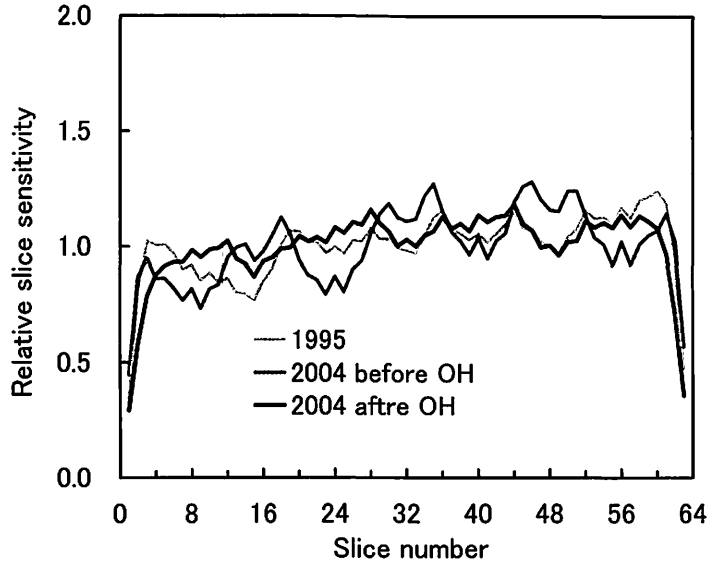

Figure 3. Variation of relative slice sensitivity in 2D scan mode.

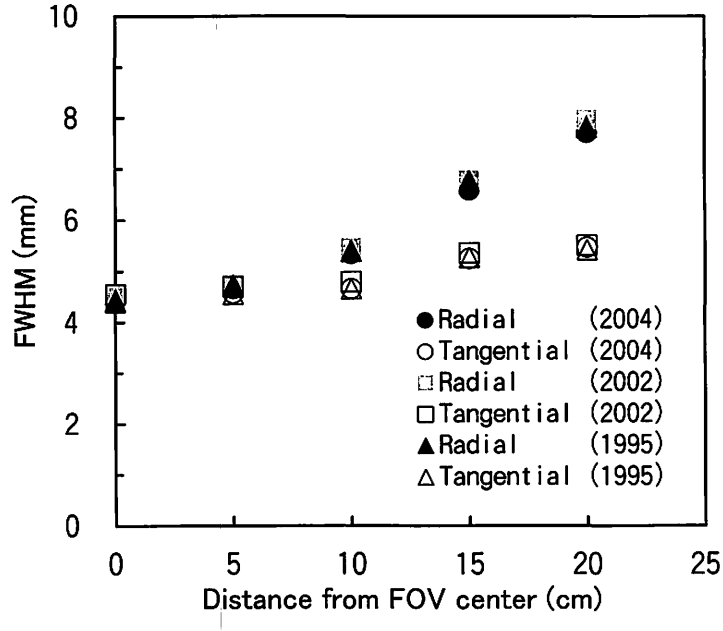

Figure 4. Variation of sensitivity of the scanner with years.

IV. 6. Study on Application of an Proton Therapy Accelerator to Boron Neutron Capture Therapy [BNCT] using MCNPX

Unno Y., Yonai S., and Baba M.

Cyclotron and Radioisotope Center, Tohoku University

Among radiation cancer therapy, Boron Neutron Cancer Therapy; BNCT is a promising treatment for brain tumors such as Glioblastoma Multiforme, and proton therapy have been adopted at some medical facilities. If both BNCT and proton therapy were installed in one hospital, a doctor will choose more suitable one and a patient will receive it without painful transfer. Therefore, in 2004, we have studied on application of a proton therapy accelerator to BNCT, using MCNPX[3] code.

An accelerator-based BNCT assembly has been already studied by S. Yonai[1]. In the dissertation, the author proposes that Ta (p, n) spallation reaction is optimum neutron source and iron is selected as the moderator for high-energy neutrons from the target. In order to shape the spectrum of epithermal neutrons in the energy of 4 eV to 40 keV, the laminated moderator of AlF_3 (26.5 cm), Al (12.1 cm) and ^6LiF (0.4 cm) is installed. All moderators and the target are enclosed by lead reflector (Fig.1).

We have calculated dose depth distributions with the above assembly at proton 150 MeV and 250 MeV (Fig. 2). A patient who is imitated by phantom, which is compounded by average soft tissue for male of ICRU44[4], is placed at 10 cm from the moderator bottom surface. Comparing with the distribution at 50 MeV (S. Yonai have already proposed the feasibility in ref. 2), the dose decreases at 250MeV, because fast neutrons are not moderated satisfactorily in the iron moderator. Therefore, we have modified the moderator for fast neutron by following two ways.

I. Tungsten moderator have replaced the iron moderator

II. Thickness of the iron moderator have changed 30 cm to 50 cm.

With the tungsten moderator, the result is shown in Fig. 3 at proton 50 MeV. The dose increases in case of only 30 cm thickness of the tungsten moderator. However, electric current needed to treat within 60 min is 1.2 mA, and generally we cannot realize the

current. Therefore, the iron moderator have superior to tungsten, because total cross section of tungsten have a high resonance at the neutron energy 10 eV-10 keV (Fig. 4).

On the other hand, we also have changed thickness of the iron moderator. The results are shown in Fig. 5. In this condition, the current is in Table 1. These results indicate that the iron moderator have advantage at higher energy, and, if an accelerator 150 – 250 MeV provided the current shown in Table 1, this accelerator could be applied to accelerator-based Boron Neutron Capture Therapy.

References

1) Yonai S., Tohoku University, Ph.D thesis.
2) Yonai S. et al., Med. Phys. **30** (2003) 2021.
3) Waters L.S., MCNPX User's Manual, TPO-E83-G-UG-X-00001 Revision 0, November **14** (1999).
4) International Commission on Radiation Units and Measurements; Tissue Substitutes in Radiation Dosimetry and Measurement, ICRU report **44** (1989).

Table.1 Beam current needed to treat within 60min.

Proton [MeV]	Fe thickness [cm]	Beam current [μ A]
50	30	99
150	30	7.7
250	50	5.0

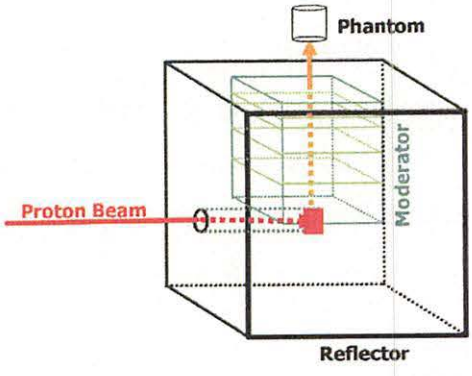

Figure 1 Geometry.

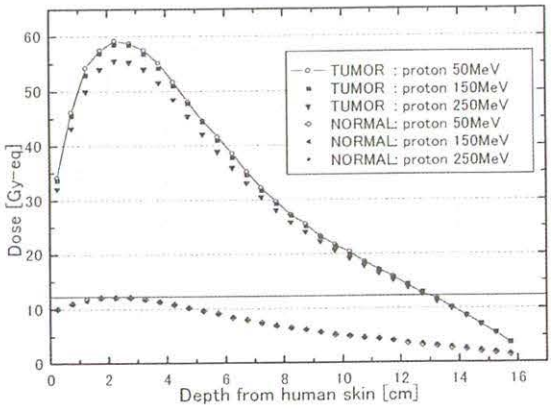

Figure 2. Dose depth distribution at proton 150 and 250 MeV.

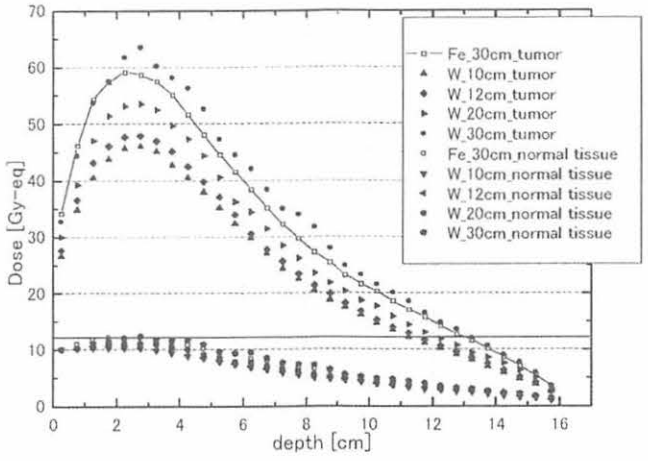

Figure 3. Dose depth distribution with the tungsten moderator.

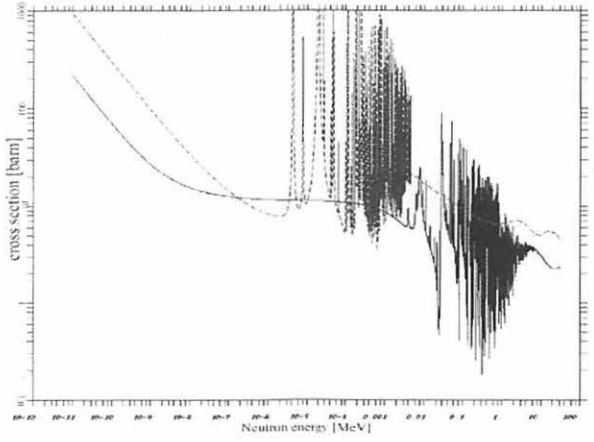

Figure 4. Total cross section of iron (black) and tungsten (blue).

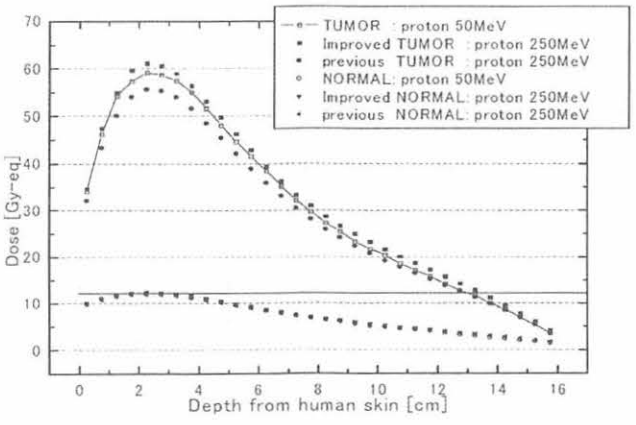

Figure 5. Dose depth distribution with change of the iron thickness at 250 MeV.

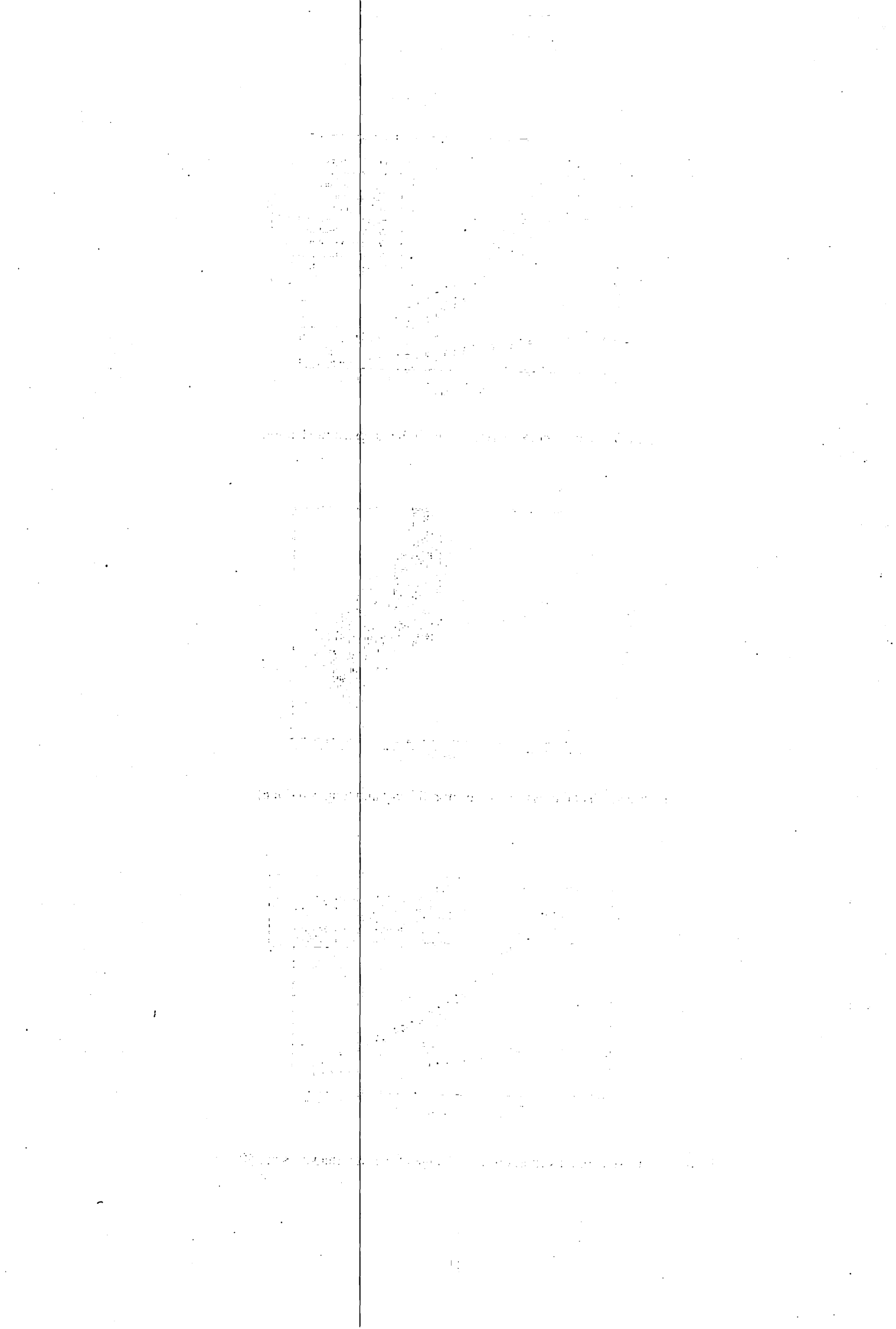

V. PIXE ANALYSIS

V. 1. The Results of Chemical State Analusis for Cr Compounds Using Carbon Ion PIXE

Amartaian TS., Ishii K., Yamazaki H., Matsuyama S., Suzuki A., Yamaguchi T., Abe S., Inomata K., and Watanabe Y.

Department of Quantum Science and Energy Engineering, Faculty of Engineering, Tohoku University

INTRODUCTION

The heavier elements, like As, Cd, Pb, Hg are highly toxic to the human body even at trace level. Furthermore, the toxicity of these elements differs widely in their chemical state. Therefore, trace heavy element analysis with their chemical state and high sensitivity is of great importance for environmental monitoring. Particle induced x-ray emission (PIXE) is a powerful technique for quantitative analysis because it is non-destructive, multi-elemental (from Na to U), highly sensitive and requires no special sample preparation. Usually proton beams with an energy around 3 MeV, are used in PIXE offering high sensitivity[1]. Since chemical shift is very small and difficult to measured with conventional Si(Li) detector, high sensitive measurement with chemical state is impossible in this condition.

The sensitivity of PIXE strongly depends on the x-ray production cross-sections, which are proportional to the square of the projectile charge[2], it can be expected that the use of heavy ion beams will improve the sensitivity of the analysis considerably. Furthermore, chemical change due to chemical state of the elements may be measured with conventional Si(Li) detector, since chemical change will be expanded due to multiple ionization. In our previous work, PIXE analysis using 70 MeV carbon ions is studied. In case of carbon bombardment, the lower limit of detection (LLD) for heavier elements is improved 2-4 times compared to proton bombardment[3].

Here, the carbon ion beams are applied to chemical state analysis using PIXE. In this study, chemical changes of energy shift, peak width and intensity of k_β line for Cr

compounds were measured using 70 MeV $^{12}C^{6+}$ ions and 3 MeV protons. And the results are compared.

EXPERIMENTAL

Experiments for carbon ions and protons are carried out at Cyclotron Radioisotope Center and Dynamitron laboratory at Tohoku University, respectively, in the similar condition. Samples are $Cr_2(SO_4)_3$, $CrCl_3$, $Cr(NO_3)_3$, $K_2Cr_2O_7$, Cr metal, CrB_2, Cr_2O_3, CrB and $CrF_3 3H_2O$. Three samples are prepared for each compound and measurements are carried out for three times for one sample. The targets were placed at an angle of 45°with respect to the beam direction. X-rays emitted from the target were measured at an angle of 90° with respect to the beam direction, by a Si(Li) detector. 1 mm Mylar film was placed in front of the Si(Li) detector to absorb the intense yield of low energy x-rays. The energy calibration was obtained with characteristic x-rays from a ^{241}Am source.

RESULTS

The relative change of an intensity ratio of k_β and k_α (Intensity Ratio), a ratio of k_β and k_α line width (line width ratio) and an energy difference between k_β and k_α line (relative energy shift) are shown 3-dimentionally in Figure 1 for protons and carbon ions. The changes of these parameters are within experimental errors except for intensity ratio in case of proton bombardment and difficult to specify chemical state of the elements. In case of carbon ion bombardment, relative energy shift changes significantly, which corresponding to changes in distribution of L-shell vacancy. For linewidth ratio, considerable change was not observed. For changes in those parameter corresponds to their chemical state. It shows that PIXE with heavy ions will lead to chemical state analysis with high-sensitivity.

ACKNOWLEDGEMENTS

The authors thank the working group of the Cyclotron Radioisotope Center, Tohoku University for the operation and maintenance of the accelerator and Prof. W.Galster for his helpful discussions.

References

1) Johansson S.A.E. and Campbell J.L. PIXE A Novel Technique for Elemental Analysis. John Wiley & Sons Ltd., pp 32-33 (1988).
2) Ishii K., Orihara H., Iwata Y., Bessho K. Int. J. PIXE **4** (1994) 1.
3) Amartaibvan Ts., Ishii K., Yamazaki H., Matsuyama S., Suzuki A., Yamaguchi T., Abe S., Inomata K., and Watanabe Y. 823.1~3, http//pixe2004.ijs.si/, Proceedings of 10th international conference on PIXE and its applications, Portoroz, Slovenia, June 4-8, 2004.

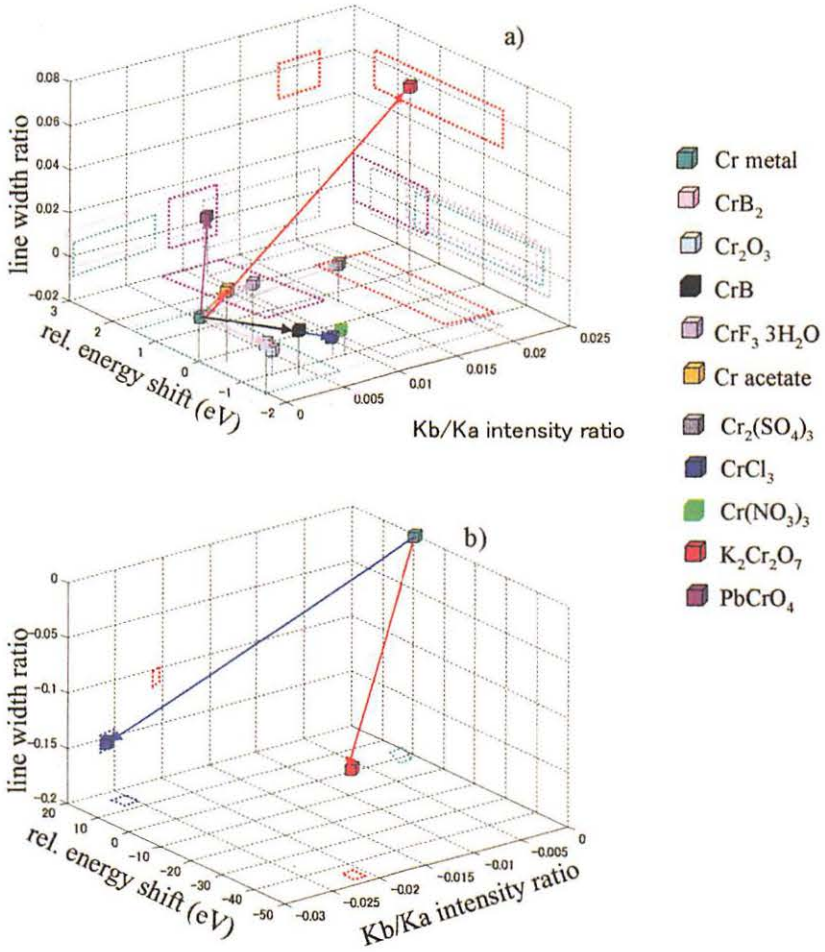

Fig. 1. Fig. 1. 3dimentional plot of line width ratio, relative energy shift and k_β/k_α-intensity ratio.

V. 2. Development of Monitoring System of Aqueous Environment by PIXE VI: Quantitative Analysis for Cr(III) and Cr(VI) Ions in Environmental Water Samples

Yamazaki H., Ishii K., Matsuyama S., Takahashi Y., Amartaivan Ts., Yamaguchi T., Momose G., Inomata K., Watanabe Y.,Ishizaki A., Oyama R., and Kawamura Y.

Department of Quantum Science and Energy Engineering, Graduate School of Engineering, Tohoku University

INTRODUCTION

A large amount of hazardous chemicals is discharged into the environment in the process of industrial activities. Thus water quality monitoring becomes increasingly important as we must use new water resources such as deep underground water. The toxic effects of some chemicals in the biosphere have been pointed out previously. The inclusion of a harmful element into flora and fauna strongly depends on the element's oxidation state. In monitoring pollution, it is thus necessary to determine both the quantity and the chemical state of a harmful element in environmental samples. Chromium shows a greatly different hazardousness according to its oxidation state and in Japan the quality limit of environmental water samples is legally set to lower than 50 ppb (ng/ml) for harmful chromium of hexavalent state. However complex separation and preconcentration procedures are required in order to determine Cr(VI) concentrations below 50 ppb in environmental water samples by using the spectrophotometric method, graphite furnace atomic absorption spectroscopy or induced coupled plasma atomic emission spectroscopy. PIXE using 3 MeV protons shows high sensitivity for chromium. Chemical states of chromium in percent-level concentrations can be determined by using the wavelength-dispersive PIXE technique, but this technique cannot be applied to assay the oxidation state of chromium at trace level concentrations.

In this study, an enhanced sample preparation method for PIXE analysis was developed for assaying the oxidation state of chromium ions dissolved in water samples. Trivalent Cr^{3+} ions are adsorbed at pH 9 by ferric hydroxide colloids generated in the solution and PIXE targets for analyzing the total concentration of chromium in both

hexavalent and trivalent states are prepared by depositing 0.15 ml of a sample solution on a user-made thin polycarbonate film. PIXE analyses of the two kinds of targets reveal the fraction of chromium of different oxidation state. The applicability of PIXE using this sample- preparation technique was confirmed to determine the oxidation state of chromium ions for concentrations less than 50 ppb in river water samples.

EXPERIMENTAL

Target preparation of dissolved trivalent Cr or hexavalent Cr ions

The standard method for collecting ferric hydroxide colloids selectively adsorbing Cr^{3+} ions on a thin filter was tested by investigating the pH-dependence of the recovery of dissolved chromium ions in 50 ppb concentration and ferric ions in 1 or 5 ppm (μg/ml) concentration added to solutions containing coexisting ions such as K^+, Ca^{2+}, Mn^{2+}, Cl^-, SO_4^{2-} and PO_4^{3-} in ppm concentrations, and the obtained calibration curve covers the concentration range from 5 to 100 ppb for Cr^{3+} ions. The target preparation procedure is as follows. In a 25 ml solution containing 50 ppb Cr^{3+} and coexisting ions in ppm-concentrations, in which the pH is adjusted to around 2 by adding conc. HNO_3, a chosen amount of ferric ions is added on a hot plate at 80°C, and then the pH is readjusted to a selected value by adding 2% NH_3 aq. After stirring 2 minutes on the hot plate at 80°C, the solution is filtered under suction (*ca.* 250 mmHg) through a Nuclepore filter of 0.2μm pore size and 10μm thickness. In order to determine the best suitable pH value for separating trivalent Cr ions from hexavalent ones in a solution, the target preparation procedure was applied to solutions containing 50 ppb CrO_4^{2-}. Test solutions containing chromium of different oxidation states and typical elements of appropriate concentrations in river water were used after serial dilution of each standard solution of certified concentration (1.00 mg / ml).

In order to confirm a high sensitivity of PIXE for analyzing the total chromium concentration, targets for CrO_4^{2-} were prepared by depositing 30 μl of test solution on a user-made polycarbonate film. The test solutions contained 0.5 ppm Ga as an internal standard. After drying at 60°C, the procedure was repeated four more times for a total of 150 μl dried solution on a film. As mentioned in our previous study,[12,13] a thin polycarbonate film is prepared by slowly dropping 0.25 ml of 0.5 wt% polycarbonate solution in chloroform- benzene mixture within a 20-mm aperture of Mylar target frame floating on 50 wt% sucrose aqueous solution. Rutherford backscattering spectra for the

user-made film and commercial polycarbonate film of 5 μm thickness were obtained with 3 MeV proton beams at a 135° scattered angle with respect to the incident beam axis. In order to evaluate the reliability of the quantitative PIXE analysis for samples deposited on polycarbonate films, a calibration curve was measured for 2-4 μC accumulated charges covering the concentration range from 10 to 100 ppb for CrO_4^{2-}.

PIXE analysis

The targets prepared from test solutions were analyzed in a vacuum chamber by using the submilli-PIXE camera (3 MeV protons, 1-5 nA beam currents, 4x4 mm scanning area, irradiation time 5-10 minutes) at Tohoku University, Japan. Target X-rays were measured at 135° with respect to the beam with a Si(Li) detector (0.012 mm thick Be window, 10 mm^2x3mm thick) covered with a 200-μm Mylar absorber whose high geometric efficiency allows the detection of X-rays > 4 keV. A target containing Fe^{3+} and Cu^{2+} of a known amount (40 ppb in a 25 ml solution) was prepared by a DBDTC-DBS pre-concentration technique[1], and used as an external standard for normalization of PIXE spectra from the filtration targets. In PIXE-spectrum analysis, we used a least-squares fitting computer code based on the pattern analysis method which has been developed in our laboratory[2]. The lower detection limit was obtained based on exceeding 3σ statistical error of the background counts integrated over the width of detector resolution (FWHM) at the position of the X-ray energy characteristic of the element of interest in the PIXE sample spectrum.

RESULTS AND DISCUSSION

Ferric hydroxide colloids possess amphoteric ion-exchange property with the isoelectric point located in the vicinity of pH 8[3,4]. By changing the pH values, the collection rates of iron and chromium of trivalent or hexavalent state were examined for the filter of 0.2 μm pores (Fig. 1). In order to confirm separation of Cr in 50 ppb concentrations from other constituents of river water, test solutions were prepared containing major constituents such as K^+, Ca^{2+}, Cl^-, SO_4^{2-} and PO_4^{3-} in the ppm-concentrations and minor ones of $Mn^{2+}$and Zn^{2+} in the ppb-concentrations. In test solutions with ferric scavenger added in 1 and 5 ppm concentration, Cr^{3+} ions are quantitatively recovered at pH > 5, and less than 40% of added CrO_4^{2-} ions is collected from the solution of pH 4.2 but recovery largely decreases on the alkaline side of Cr^{3+} adsorption.

Since ferric hydroxide colloids are produced in a solution of pH > 3, Cr^{3+} of low concentration like 50 ppb is appreciably coprecipitated on ferric hydroxides in a wide pH region because Cr^{3+} ions easily hydrolyze[19]. The recovery of CrO_4^{2-} decreases to 1 to 3 percent in the alkaline region of pH>8, since the anionic adsorption capacity of ferric hydroxides appreciably diminishes. These results indicate that we can obtain thin and uniform targets of trivalent chromium ions well separated from hexavalent chromium ions in an alkaline region of pH > 8. The adsorption of coexisting ions in 100-300 times higher concentrations had no effect on the recovery of trivalent chromium in the coprecipitation with ferric hydroxide colloids generated in test solutions.

In order to evaluate the reliability of quantitative PIXE analysis of dissolved Cr ions in trivalent state, a calibration curve was measured using targets, which were prepared at pH 9.0 ± 0.1 by adding 1 ppm Fe^{3+} to a 25 ml of trivalent chromium solution in concentrations ranging from 5 to 100 ppb, as shown in Fig.2-(a). A linear relationship is observed between the initial concentrations of Cr^{3+} ions added to the solutions ($[Cr]_{ini}$) and the concentrations converted from PIXE analysis values of Cr^{3+} scavenged on the filter ($[Cr]_{exp}$). Although a somewhat large difference of 8-14% was observed for two targets of 100 ppb, an error margin of ±6% was obtained for five targets prepared from test solutions of 50 ppb Cr^{3+} ions. The detection limit in the present PIXE measurement setup with 0.9-2.6 μC irradiation of 3 MeV protons is 1 ppb, when the characteristics X-ray peak yield is close to the 3σ statistical error of background counts. The average recovery of ferric scavenger was 0.98 ± 0.06 for 11 calibration measurement targets, indicating no appreciable loss in filtration of ferric hydroxide colloids.

Figure 2-(b) shows the calibration measurement results of deposit targets for the purpose of analyzing the total chromium concentration in a solution. In these measurements, targets were prepared by depositing 0.15 ml solutions containing CrO_4^{2-} ions with the concentrations ranging from 10 to 100 ppb. The straight line corresponds to the relation $C_{exp} = C_{ini}$. The difference between the nominal and the experimentally obtained oncentrations seldom exceeds ±6% in a wide concentration range, although a 26 % deviation is observed in the case of 10 ppb CrO_4^{2-}, which is close to the quantification limit being three times larger than the detection limit in PIXE measurements. In the case of PIXE spectra of CrO_4^{2-} deposit targets, the detection limit was estimated to be 3.4 ppb Cr in a solution based on the 3σ statistical error of background counts. It is clear that the limit of quality of environmental water sample relevant to human life can be assessed for harmful

hexavalent chromium (< 50 ppb) by means of PIXE measurement for deposit targets onto a thin polycarbonate film with low continuum X-ray background. In Fig. 3, the RBS spectra are compared for a commercial polycarbonate film in 5 μm thickness and an user-made polycarbonate film. In the case of user-made film, two narrow peaks appear in the recorded energy spectrum, indicating a thin target with a higher energy peak of oxygen atoms and a lower energy peak of carbon atoms. Based on the chemical composition, $(C_{16}H_{14}O_3)_n$, and the density of polycarbonate, 1.2 g/cm^3, the commercial film of 5 μm thickness should contain a layer with 4.7×10^{19} atoms / cm^2 of carbon and oxygen atoms and the fitted curve area of the commercial film (upper graph) indicates a layer with 4.6×10^{19} atoms / cm^2. In the case of the user-made film (lower graph), the experimental fitted curves show a surface atomic density of 5.7×10^{18} atoms / cm^2, indicating a much thinner film of 0.6 μm.

In order to confirm the applicability of PIXE using these sample-preparation techniques to determine the distribution of chromium oxidation states in environmental water samples, ferric hydroxide scavenged targets and deposit targets were prepared from 25 ml river water samples containing 50 ppb chromium in trivalent or hexavalent state. The river water sample was collected from Natori river at the outskirts of Sendai city. The sample had a pH value of 7.78 and an oxidation-reduction potential of 414 mV at 21.8°C, indicating a reducing condition in comparison to 480 mV of the standard oxidation-reduction potential at the same pH value for the pair of Cr_2O_3 and CrO_4^{2-}. Chromium was added to the filtrate of river water, and elements, either collected on the filter or contained in the filtrate, were analyzed by PIXE. It was revealed that the river water sample contained much iron, 0.581 ± 0.005 ppm, as an insoluble constituent and also much calcium, 9.0 ± 0.8 ppm, as a soluble constituent. Figure 4-(a) shows the PIXE spectrum of ferric hydroxide target for a 25 ml river water sample containing 50 ppb of trivalent chromium ions and chromium K X-ray peaks are clearly observed. For three iron scavenge targets separately prepared at pH 9 from a 25 ml solution containing trivalent chromium ions in 50 ppb, the average analyzed value was 49 ± 3 ppb, indicating quantitative coprecipitation of added Cr^{3+} ions on ferric hydroxide colloids generated in the solution. In Fig. 4-(b), a small but clear K X-ray peak of Cr is observed in the PIXE spectrum for a ferric hydroxide target prepared from a river water sample containing 50 ppb CrO_4^{2-} ions. The PIXE analysis for three targets prepared at pH 9 under identical solution condition indicated that around 12% of CrO_4^{2-} ions added to river water samples was

precipitated with ferric hydroxide scavenger. In comparison to the recovery of a few percents of CrO_4^{2-} ions in test solutions over pH 8 (Fig. 1), an appreciable increase of chromium recovery can be ascribed to a pre-existing reducing condition for CrO_4^{2-} in river water. For the deposit target of the sample added by both Cr^{3+} and CrO_4^{2-} ions in 50 ppb in Fig. 4-(c), the concentration of chromium was analyzed to be 99 ± 3 ppb, which is fairly close to the total Cr concentration in the original solution. In a 25 ml sample of river water to which both Cr^{3+} and CrO_4^{2-} ions were added at 100 ppb, the K X-ray peak of Cr in the ferric hydroxide target corresponded to 113 ± 2 ppb of the original Cr^{3+} concentration in the solution, and the deposit target indicated the total Cr concentration to be 209 ± 5 ppb which is close to the total Cr concentration in the original solution. Although lead chromate is a compound with low solubility (K_{SP}=1.6 x 10^{-4}), lead ions in high concentration to precipitate hexavalent chromium in < 10^{-8} mol/dm^3 were not detected in a river water sample. These findings reveal that around 13% of added chromium of hexavalent state is reduced to the trivalent state in river water with somewhat reducing condition for CrO_4^{2-} (E_{SHV} = 414 mV) at pH 7.78 and 21.8°C. Light elements like carbon, nitrogen and sulfur contained in an organic such as humin in river water is thought as a cause of the reduction of hexavalent chromium. Note that the lower detection limits for Cr in river water were estimated in PIXE analysis to be 1 ppb for ferric hydroxide scavenger and 7 ppb for deposit target, respectively. When compared with the detection limit of 3.4 ppb for deposit targets prepared from test solutions of CrO_4^{2-}, the coexistence of Ca in high concentrations like 9 ppm in river water deteriorates the detection limit of Cr(VI), but the 50 ppb limit in environmental water samples is easily detected by the PIXE analysis of 0.15 ml water sample deposited on a thin polycarbonate film.

CONCLUSION

The techniques developed for the preparation of PIXE targets from water samples were successfully applied to examine the distribution of oxidation states of chromium in water. The target preparation and the PIXE measurements are not time-consuming and suitable for environmental monitoring. The PIXE analysis using two kinds of targets, that is, ferric hydroxide target scavenging trivalent chromium and a target where a small volume of solution is deposited onto a thin polycarbonate film, is sufficiently sensitive to reveal the oxidation state of chromium in concentrations lower than the 50 ppb quality limit of drinking water for harmful chromium of hexavalent state. Hence, the method developed in

this study shows that PIXE analysis is an effective technique for monitoring the harmful chromium(VI) ions entering the primary pathways of human metabolism.

REFERENCES

1) Yamazaki H., et al., Int. J. PIXE **7** (1997) 31.
2) Murozono K., et al., Nucl. Instrum. Methods **B 150** (1999) 76.
3) Clearfield A., ed., Inorganic Ion Exchange Materials, Florida, CRC Press, Inc., 1982, pp.161-196.
4) Anderson M.A. and Rubin A.J., Ann. Arbor. Science (1981) 183.
5) Base C.F. and Mesmer R.E., The Hydrolysis of Cations, John Wiley & Sons, New York (1976), 211-220.

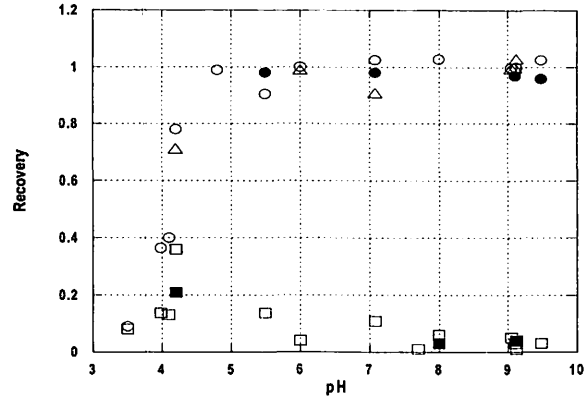

Figure 1. The pH-dependence of filtration scavenging for trivalent and hexavalent chromium with ferric hydroxide colloids. The precipitates were filtered under suction (~250 mmHg) with a Nuclepore filter of 0.2 μm pores. In a 25 ml solution containing 15 ppm K^+, 5 ppm Cl^- and 5 ppm SO_4^{2-}, ○: 50 ppb Cr^{3+} and 1 ppm Fe^{3+} added, ●: 50 ppb Cr^{3+} and 5 ppm Fe^{3+} added, □: 50 ppb CrO_4^{2-} and 1 ppm Fe^{3+} added, ■: 50 ppb CrO_4^{2-} and 5 ppm Fe^{3+} added, △: 50 ppb Cr^{3+}, 1 ppm Fe^{3+}, 5 ppm Ca^{2+}, 0.1 ppm Mn^{2+}, 0.025 ppm Zn^{2+} and 3 ppm PO_4^{3-} added.

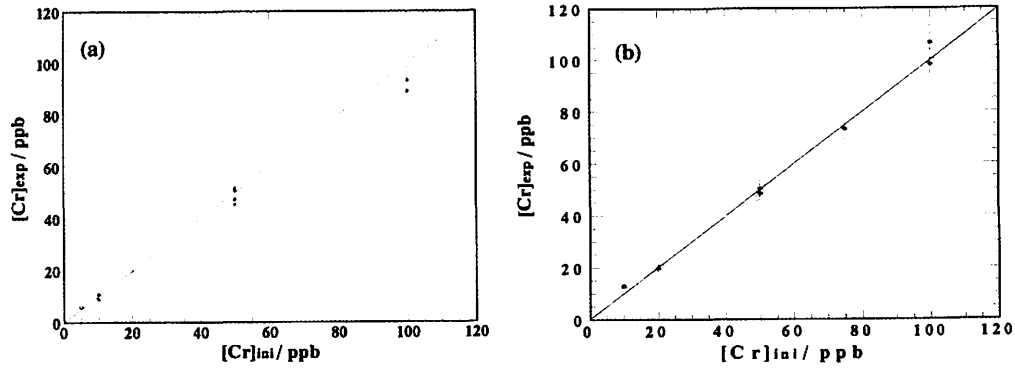

Figure 2. Experimental results ($[Cr]_{exp}$ / ppb) versus nominal concentrations ($[Cr]_{ini}$ / ppb), (a):trivalent chromium ions collected on ferric hydroxides targets using 1 ppm of Fe^{3+} scavenger, filtration at pH 9.0 ± 0.1, 0.8-2.6 μC irradiation in PIXE measurements, (b):hexavalent chromium ions deposited on a user-made thin polycarbonate film. 0.15 ml deposition, 2.4-4.1 μC irradiation in PIXE measurements.

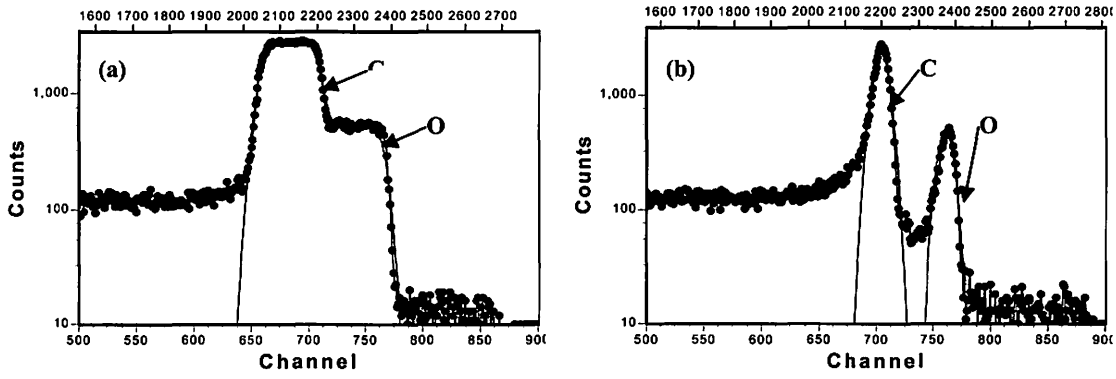

Figure 3. RBS energy spectra obtained with 3 MeV protons for thin polycarbonate films. The scattering angle is135^{O}, (a): a commercial polycarbonate film of 5 μm thickness, (b): user-made polycarbonate film.

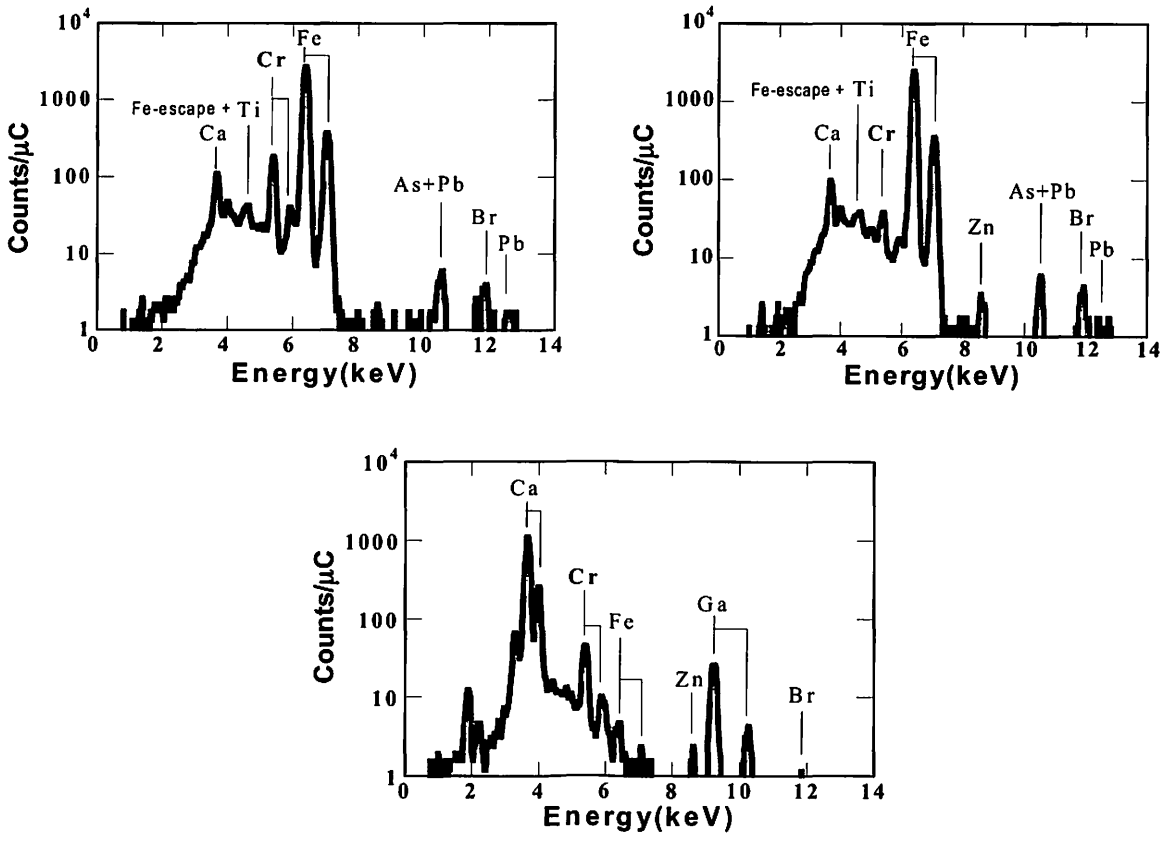

Figure 4. PIXE spectra for deposit and ferric hydroxide scavenge (pH 9) targets of river water samples with Cr added. (a): ferric hydroxide target of 25-ml river water added Cr^{3+} in 50 ppb, (b): ferric hydroxide target of 25-ml river water added CrO_4^{2-} in 50 ppb, (c): deposit target of 0.15-ml river water added both Cr^{3+} and CrO_4^{2-} in 50 ppb, PIXE measurement: 1.4-2.6 μC of 3 MeV protons, 200 μm Mylar absorber.

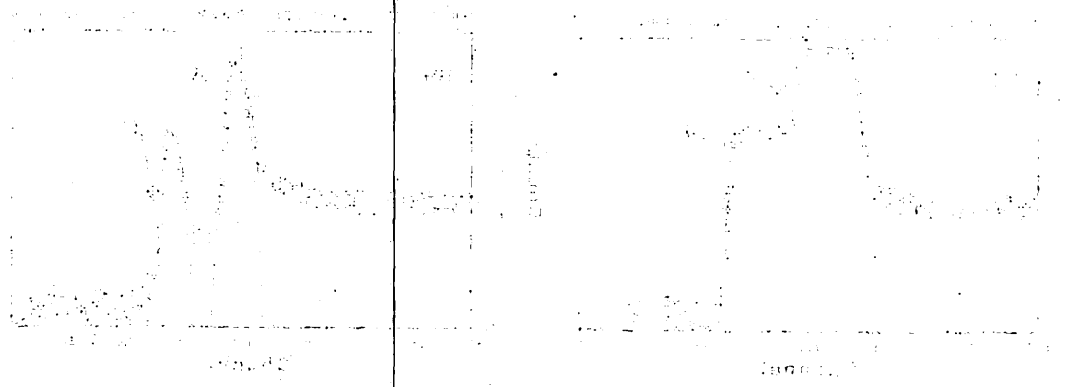

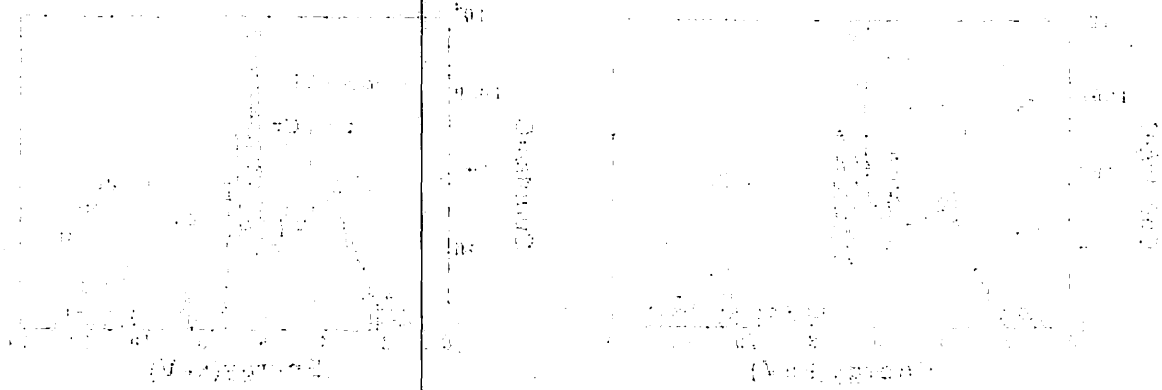

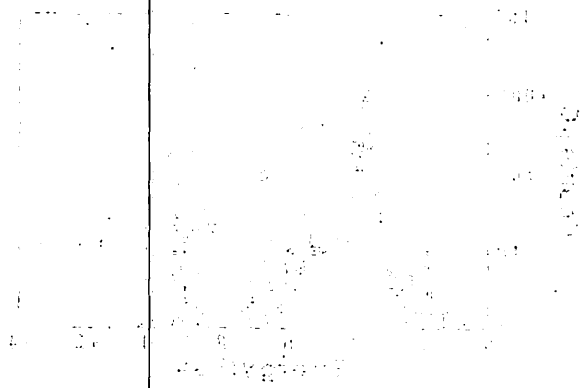

VI. RADIOCHEMISRTY AND NUCLEAR CHEMISTRY

VI. 1. Distribution Behavior of Technetium to Liquid, Solid Phases and onto Metal Surfaces after Supercritical Water Treatment

Satoh I., Yamamura T., Okuyama N., Shiokawa Y., Takahashi M., Sekine T.[*], *Sugiyama W.*[**], *Park K. -C.*[***], *and Tomiyasu H.*[***]

Institute for Materials Research, Tohoku University
[*]*Department of Chemistry, Graduate School of Science, Tohoku University*
[**]*Chubu Electric Power Co. Inc.*
[***]*Department of Chemistry and Material Engineering, Faculty of Engineering, Shinshu University*

Introduction

Above 647 K and 22 MPa, water is a supercritical fluid, which possesses unique solvating and transport properties compared to liquids or gases. Supercritical water (SCW), which shows liquid-like density and gas-like diffusivity, has the ability not only to decompose materials soluble in liquid water but also to promote particular reaction. Gasification of organic materials in the supercritical water using RuO_2 as a catalyst has been developed[1]. We applied this gasification method to the decomposition of bulky non-flammable organic materials generated in nuclear power plants, classified as low-level radioactive wastes (LLW)[2,3]. Radioactive iron, cobalt, cesium, iodine, strontium attached to the organic materials were found to be recovered in the solid phase with or without precipitation reagents and showed no transfer to gas phase.

Appreciable yield of 6.2% in the thermal neutron fission leads to the formation of technetium-99 with long-lived half-life ($t_{1/2}$= 2.1×10^5 y). The LLW also contains the technetium, which is known to have oxidation states from 0 to VII and shows variety of chemical properties including sublimation of Tc_2O_7 above 584 K[4]. For the decomposition of LLW by the SCW method, the distribution behavior of technetium is to be clarified. In this study, distribution of technetium after supercritical water reaction among solid, liquid and gas phases were determined. The distribution behavior was discussed concerning with differences (i) between SCW reaction with ruthenium oxide (RuO_2) and with hydrogen peroxide (H_2O_2), (ii) with or without its carrier and (iii) between technetium and alkaline metal. Adsorption of technetium on surface of various metal materials, which are

candidates for reactor materials, during the SCW reactions were also discussed.

Experimental

Technetium-95m was produced by $^{93}Nb(\alpha,2n)^{95m}Tc$ reaction at Cyclotron and Radioisotope Center of Tohoku University and purified by sublimation, followed by dissolution in water to prepare $HTcO_4$. Technetium-99 was used as a carrier. Ruthenium(IV) oxide (purity: >99.9 %) and granular polyethylene (medium density) were purchased from Kishida Chemical Co., Japan and Aldrich Chemical Company, Inc., U.S.A., respectively, and used without further treatment.

A batchwise reactor with 10 mL capacity made of Hastelloy C-22 was used. A small portion of an aqueous solution including about 1 mg of technetium, three pieces of metal plates (SUS304, Hastelloy C-22, Inconel 625, 5x10x1 mm size, polished with #2000), water and either of oxidant (H_2O_2) or reductant (RuO_2 and 150 mg of granular polyethylene) were loaded into the reactor and the supercritical reaction under the condition of "723 K-43 MPa-30 min." was carried out. After cooled off to room temperature, distribution coefficient was determined by measurement of γ-ray spectra of three phases separated (solid, liquid and gas) and metal pieces. Cesium solution with a tracer of ^{137}Cs was used for a reference of the behavior.

The radioactivity of ^{95m}Tc was determined from the areas of peak at 204.11 keV by using a γ-ray spectrometer (GEM-28185-P, ORTEC Inc., USA). The distribution of their radioactivity in solid, liquid and gas phases was determined as given by

$$D_{\text{phase}} = \frac{A_{\text{phase}}}{A_{\text{T}}} \qquad (1),$$

where D_{phase} designates the distribution ratio, A_{T} and A_{phase} are the radioactivity of initially loaded and the radioactivity of each phase after the supercritical water reaction respectively, and the subscription phase is "sol", "liq" or "gas", referring to the solid phase, the liquid phase and the gas phase, respectively.

Results and discussion

Distribution of technetium with or without carrier and /or precipitating agent

Amount of technetium found in the solid, liquid and gas phases recovered after supercritical water reaction are indicated with the distribution ratio D in Table 1. Both in H_2O_2 and RuO_2 methods, technetium does not transfer to gas phase in spite of its low

boiling point but limited to solid phase. This distribution of technetium was not affected by addition of its carrier of ^{99}Tc but shifted to solid phase by addition of $Fe(OH)_3$.

It should be noted that only around 20% of technetium was found in a recovery after SCW-RuO_2 reaction. By measuring γ-rays from inside of the hastelloy reactor, appreciable quantity of technetium was found, in spite of that inside wall were rinsed many times with water after SCW-RuO_2 reaction. On the other hand, fairly amount of technetiumu was recovered after SCW-H_2O_2 reaction.

Distribution of technetium onto metal surfaces

It is worthwhile to note that technetium shows a large tendency to be adsorbed onto metal surfaces and the adsorbed technetium should be removed by repeating washing by H_2O_2 method for the next reaction. In order to elucidate the adsorption on metal surfaces, supercritical water reactions were carried out with three types of metal materials (Table 2). Moreover, the results for technetium was compared with those for cesium, which is a member of alkaline metal ion whose character is simple ionic. Technetium was found to adsorbed onto various metal materials. Washing by SCW with H_2O_2 for 5 times is required to remove the adsorbed technetium from the reactor.

In RuO_2 method, technetium may be reduced to colloidal or polymeric TcO_2 or $TcO(OH)_2$ which has a great affinity to metal surface[5,6]. The adsorbed TcO_2 can be oxidized to TcO_4^- by H_2O_2 and dissolved in solution. Effect of supercritical water with RuO_2 on technetium chemistry requires further investigation.

Conclusion

Distribution of technetium after supercritical water reaction was investigated. Technetium does not transfer to gas phase in spite of its low b.p. but distributes to solid phase both in SCW with H_2O_2 and RuO_2 reactions. Furthermore, technetium was found to adsorbed on to various metal materials. Washing by SCW with H_2O_2 for 5 times is required to remove adsorbed technetium from reactor. The result of adsorption of technetium by SCW with RuO_2 and the dissolution by SCW with H_2O_2 suggested that the reductive atmosphere of SCW with RuO_2 may result in the formation of colloidal or polymeric TcO_2 or $TcO(OH)_2$ which have a great affinity to metal surface. The supercritical water process can be used for decomposition of non-flammable plastics of LLW with limiting technetium to solid and onto metal surfaces.

References

1) Park K.-C. and Tomiyasu H., Chem. Commun. (2003) 694.
2) Sugiyama W., Yamamura T., Park K.-C., Tomiyasu H., Satoh I., Shiokawa Y., Okada H. and Sugita Y., J. Supercritical Fluids **35** (2005) 240.
3) Sugiyama W., Park K.-C., Yamamura T., Koizumi T., Okada H., Sugita Y. and Tomiyasu H., J. Nucl. Sci. Technol. **42** (2005) 256.
4) Schwochau K., Technetium: Chemistry and Radiopharmaceutical Applications,Wiley-Vch, Weinheim (2000)
5) Naito S., Sekine T., Kino Y. and Kudo H., Radiochim. Acta **82** (1998) 129.
6) Sekine T., Narushima H., Kino Y., Kudo H., Lin M. and Katsusima Y., Radiochim. Acta **90** (2002) 611.

Table 1. Distribution of technetium to three phases after supercritical water treatment.

Reaction	Carrier		$10^2 D_{sol}$ ‡†	$10^2 D_{liq}$ ‡†	$10^2 D_{gas}$ ‡
	Tc-99 /mg	$Fe(OH)_3$ /mg			
RuO_2 method	---	---	23.75 (97.11)	0.71 (2.89)	0.00
	0.5	---	22.86 (97.26)	0.64 (2.74)	0.00
	0.5	13	17.30 (99.30)	0.12 (0.70)	0.00
H_2O_2 method	---	---	86.54 (99.28)	0.63 (0.72)	0.00
	0.5	---	41.98 (97.91)	0.90 (2.09)	0.00

‡D_{phase} were determined according to eq. (1).
†Values in parentheses are calculated by $D_{phases}/(D_{sol} + D_{liq} + D_{gas})$

Table 2. Distribution of Tc and Cs to each site after supercritical water reactions of non-flammable plastics¶

Contents		No reaction ‡		RuO_2 method				H_2O_2 method		
		Cs-137	Tc-95m	Cs-137	Cs-137 + $CsNO_3$	Tc-95m	Tc-95m + Tc-99	Cs-137	Tc-95m	Tc-95m + Tc-99
Phases recovered after reaction	Solid phase	---†	---†	5.8	15.63	33.9	65.75	1.9	17.8	16.75
	Liquid phase	83.7	85.5	64.5	80.29	0.5	0.76	80.2	1.5	23.62
	Gas phase	---†	---†	0	0	0	0	0	0	0
Metal specimens	SUS304	0	0	0		1.9	1.95	0	1.2	1.47
	Hastelloy	0	0	0		7.7	0.93	0	3.8	0.62
	Inconel	0	0	0		1.4	1.38	0	0.9	0.71
Washings with SCW-H_2O_2 reaction	1st reaction	3.1	4	6.9	4.17	22.6	24.12	12.1	51.8	28.55
	2nd reaction	1.3	1.6	5.9	0.63	4.8	1.79	2.4	3.8	5.58
	3rd reaction	---	---	2.9	0.17	2.3	0.52	1.1	1.7	1.11
	4th reaction	---	---	1.6	0.12	3.8	0.41	1.3	1.3	0.26
	5th reaction	---	---	0.8		1.4	0.38	0.5	0.8	0.51
Total amount recovered		88.1	91.1	88.4	101.01	80.3	97.99	99.5	84.6	79.18

¶Distributions are indicated as percentile to the amount initially loaded. ‡Solutions and specimens were left in the reactor for two hours without supercritical water reaction. †No solid and gas phases owing to no reaction.

VI. 2. Insertion of Po in C_{60} Fullerenes and Formation of Dimers

*Ohtsuki T. and Ohno K.**

Laboratory of Nuclear Science, Tohoku University
**Department of Physics, Yokohama National University*

Endohedral fullerenes which have atoms inside the C_{60} cage have attracted great current interest in the physical and/or chemical properties. However, the production rate of the endohedral C_{60} is quite low compared to the ordinary C_{60}. For pre-exisiting C_{60}, Saunders[1] have demonstrated the possibility of incorporating noble-gas atoms into fullerenes under high-pressure and high-temperature conditions. Braun et al.[2] have produced an atom-doped C_{60} by using the prompt-gamma or particle recoil induced by neutron irradiation. However, only partial information on the formation process, on the produced materials, and on the nature of the chemical interaction between a foreign atom and a fullerene cage have been established.

So far, we examined the production of fullerene derivatives created when alkali, alkali-earth, transition metals, 3B-6B elements and noble-gas elements, were produced by nuclear reactions induced by irradiation of samples with high-energy bremsstrahlung or charged particles[3-6]. We found that the radioactive Be, C, N, noble-gas elements and 3B-6B elements can be doped in fullerenes. Such radioactive fullerenes and their derivatives are of considerable interest not only for following the location and metabolism of these substances in living organisms[7-9] but also for nuclear waste disposal applications where the fullerene may serve as a nano-container of radioactivities[10].

Here, we show that even a heavy nuclide like the ^{210}Po isotope can be inserted into C_{60} from outside of the cage by nuclear recoil. In order to theoretically check the possibility of direct insertion, we carried out it it ab initio molecular-dynamics (MD) simulations based on the all-electron mixed-basis approach[11].

To produce the source of radioactive nuclides, Bi_2O_3 was used in powder form. The grain size of the materials was smaller than 20 μm. Purified fullerene (C_{60}) was carefully mixed with each material (weight ratio=1:1) in an agate mortar, adding a few ml

of carbon disulfide (CS_2). After drying up, about 100 mg of the mixture sample was wrapped in a pure aluminum foil of 10 mum in thickness for irradiation. Irradiation with 16 MeV deuterons was performed at the Cyclotron Radio-Isotope Center, Tohoku University. The beam current was typically 1 μA and the irradiation time was about 5 hours. Only ^{210}Po (α-source) can be produced in the ^{209}Bi(d,n) reaction. The radionuclide produced, its characteristic α-ray, its half-life, and the nuclear reaction are 5.3 MeV, 139 days and ^{209}Bi(d,n)^{210}Po, respectively. The sample was dissolved in CS_2 and filtered through a Millipore filter(pore size=0.2 μm) to remove insoluble materials. The soluble portion was injected into a HPLC device equipped with a 5PBB (Cosmosil) at a flow rate of 3 ml/min. For the confirmation of fullerenes and their derivatives, a UV detector was installed with a wavelength of 400 nm. In order to measure the α-rays emanating from ^{210}Po, eluent fractions were collected for 30 sec intervals. After drying up the CS_2 solvent on a stainless-steel plate, the 5.3 MeV α-ray activities from ^{210}Po of each fraction were measured in a vacuum chamber with a silicon surface-barrier detector (SSD) coupled to a 1024-channel pulse-height analyzer. Therefore, radioactive ^{210}Po could be uniquely detected by means of its characteristic α-rays.

Figure 1 shows for materials inserted into C_{60} samples, a radiochromatogram measured with an α-detector and a chromatogram measured with an UV detector, both plotted versus retention time after injection. A clear correlation between the UV-absorption intensity and the α counting rate in the 6.5-7 minute interval is seen in Fig. 1. From the correlation of the elution behavior between the UV chromatogram and the radioactivities of the ^{210}Po atoms, we found that the atom-doped fullerene $^{210}PoC_{60}$ was indeed produced by nuclear recoil implantation.

In order to theoretically check the possibility of direct insertion, we turn our attention to the it *ab initio* molecular dynamics simulations. The method used here is based on the all-electron mixed basis approach[11] using both plane waves (PW's) and atomic orbitals (AO's) as a basis set within the framework of the local density approximation (LDA) in density functional theory. For the LDA exchange-correlation function, we adopt Ceperley-Alder's fitting form. In the present study, we have recently implemented in our program the AO's with the f symmetry including a semi-relativistic effect in order to treat the Po atom. To generate the f AO's as well as the s, p and d AO's defined inside the non-overlapping atomic spheres, we use an atomic program based on Herman-Skillman's framework with logarithmic radial meshes. We use a supercell composed of 64×64×64

meshes (with a mesh corresponding to 0.196 Å), in which we put one C_{60} molecule and one Po atom at a distance 1.50 Å outside from the center of a six-membered ring of C_{60}. For the present system, we use 339 AO's and 4169 PW's corresponding to a 7 Ry cutoff energy. For dynamics, we use an adiabatic approximation, and set the basic time step as $\Delta t = 0.1$ fs and perform five steepest descent (SD) iterations after each update of atomic positions. The Po atom has a given initial velocity toward the center of the six-membered ring of C_{60}. We do not impose any velocity control, so that the system is almost microcanonical with little energy dissipation from the SD algorithm. Fig. 2 represents several snapshots of our simulation where Po hits the center of the topmost six-membered ring with the 40 eV initial kinetic energy. It is very surprising that such large atoms as Po can be so easily encapsulated from the outside. Thus we find that Po is successfully encapsulated and $Po@C_{60}$ is created.

To check the amount of $^{210}Po@C_{60}$ produced, we performed three times extractions in CS_2 solvent using an ultrasonic generator for the sample irradiated. The result of the alpha-spectrometry in each fraction is shown in the inserted figure in Fig. 1. Even though there is a slight delay in the chromatogram, populations of ^{210}Po were seen in the 6.5-7 min and 8-9 min intervals. It was found that the amounts of the soluble materials extracted in the three-times extraction were about twenty times greater than in the one-time extractions in the CS_2 solvent. The observation of the second peak (8-9 min) corroborates the formation of endohedral fullerene dimers with encapsulated radionuclides, namely $^{210}Po@C_{60}$-C_{60}. It seems that the shock of the collisions produces fullerene dimers through interactions with a neighboring fullerene cage.

In the present study, radioactive nuclides are produced by (d,n) reactions. The energetic nuclides should destroy the fullerene cages because the K.E. is estimated to be of a quite different order of magnitude than the energies (eVs) of molecular bonding. Therefore, the atoms being produced escape from their own material due to the K.E. of about a few hundred kiloelectron volts. Then, the kinetic energies are reduced in the sample to a magnitude which is appropriate for the fusion. Finally, the radionuclides hit the C_{60} cages and stop in the cage (formation of endohedral fullerene) and, furthermore, the shock produces fullerene polymers by interaction with a neighboring fullerene cage.

Such endohedral fullerenes can serve as a nano-containers of radioactivities and deliver them to the objective tissues in various metabolic pathways. Here, $^{210}Po@C_{60}$ molecules can be easily broken to pieces due to the energy release of α-ray (5.3 MeV) from

^{210}Po and that from the residual nuclide (^{206}Pb, a few hundred keV). And, the α-ray may attack the objective tissues in the body following the explosion of the nano-container (C_{60}). Furthermore, if the complex isotopes ^{207}Po(positron emitter) and ^{210}Po and/or ^{206}Po(α emitter) are used, it can be followed the metabolic pathway by the annihilation γ-rays with a Positron Emission Tomography (PET). Therefore, if a suitable preparative technique could be developed, there may be valuable applications of these in nuclear medicine and/or as tracers. Recent advances in fullerene chemistry may also make it possible to control fullerene absorption/excretion profiles in the future.

References

1) Saunders M., Cross R.J., Jimenez-Vazquez H.A., Shimshi R., and Khong A., Science **271** (1996) 1693.
2) Braun T. and Rausch H., Chem. Phys. Lett. **288** (1998) 179.
3) Ohtsuki T., Masumoto K., Ohno K., Maruyama Y., and Kawazoe Y., Phys. Rev. Lett. **77** (1996) 3522.
4) Ohtsuki T., Masumoto K., Sueki K., Kobayashi K., and Kikuchi K., J. Am. Chem. Soc. **117** (1995) 12869.
5) Ohtsuki T., Ohno K., Shiga K., Kawazoe Y., and Maruyama Y., Phys. Rev. Lett. **81** (1998) 967.
6) Ohtsuki T., Ohno K., Shiga K., Kawazoe Y., and Maruyama Y., J. Chem. Phys **112** (2000) 2834.
7) Friedman S.H., Decamp D.L., Sijbesma R.P., Dudl F., and Kenyon G.L., J. Am. Chem. Soc. **115** (1993) 6506.
8) Braun T., J. Radioanal. Nucl. Chem. **259** (2004) 331.
9) Yamago S., Tokuyama H., Nakamura E., Kikuchi K., Kananishi S., Sueki K., Nakahara H., Enomoto S., and Ambe F., Chem. Biol. **2** (1995) 385.
10) Amato I., Science **258** (1992) 1886.
11) Ohno K., Mauri F., and Louie S.G., Phys. Rev. B **56** (1997) 1009.

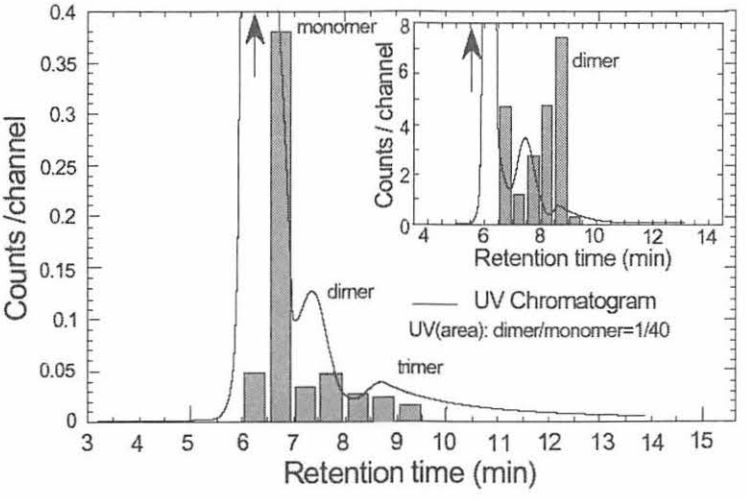

Fig. 1. HPLC elution behavior of the soluble portion of the crude extracted in the deuteron irradiated sample of C_{60}+Bi_2O_3. Plotted versus the retention time along the horizontal axis is a histogram of the alpha counting rate (in counts/s) measured with a solid-state Si-detector and a solid curve representing a chromatogram measured with a UV-detector. (The Inserted figure is for three-times-extraction in CS_2 using an ultrasonic apparatus.)

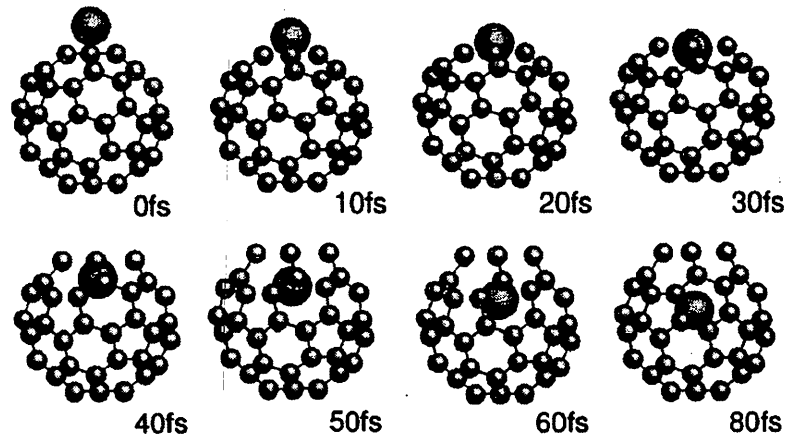

Fig. 2 Simulation of Po hitting the center of a six-membered ring of C_{60} with a kinetic energy of 40 eV. Here, the local skeleton disappears from the figure when the bond-length is elongated by more than 1.5 Å.

VI. 3. Formation Cross Section of ^{244}Cf and ^{245}Cf in the Reaction of ^{238}U+^{12}C

Ohtsuki T., Yuki H., Takamiya K.[*], *Kasamatsu Y.*[**], *Takabe T.*[**], *Nakajima K.*[**], *Hasegawa H.*[**], *Shinohara A.*[**], *Shibata S.*[*], *Mitsugashira T.*[***], *Sato N.*[****], *Suzuki T.*[****], *Miyashita Y.*[****], *Shinozuka T.*[****], *Kikunaga H.*[*****], *and Nakanishi T.*[*****]

Laboratory of Nuclear Science, Tohoku University
[*]*Research Reactor Institute, Kyoto University*
[**]*Deptartment of Chemistry, Osaka University*
[***]*Institute of Materials Research, Tohoku University*
[****]*Cyclotron Radio-isotope Center, Tohoku University,*
[*****]*Deptartment of Chemistry, Kanazawa University*

In the heavy element region, the residual formation cross sections are strongly influenced by fission competition, namely as a function of Γ_n/Γ_f. Therefore, investigation of the Γ_n/Γ_f value is very important for synthesizing heavier nuclides such as Fm, No and further heavier mass region. In the present study, the radioactive products such as ^{245}Cf and ^{244}Cf have synthesized by means of ^{238}U(^{12}C, 5n-6n) reaction. The obtained cross section can be useful for evaluation of the Γ_n/Γ_f value. Here, we applied a simple and unique method of target preparation, specifically, a membrane filter of an Al_2O_3 disk (25 mug/cm^2 in thickness[1]) that can be useful with precipitation after filtrating the target material. Furthermore, we have developed measurement devices, such as a He-jet transport and a rotating-wheel measurement system, for studying heavier nuclides than Cf isotopes. The ^{238}U deposited on prepared Al_2O_3 disks was irradiated with ^{12}C ions and the isotopes of ^{245}Cf and ^{244}Cf were produced with ^{238}U(^{12}C, xn) reactions. The obtained excitation functions of ^{245}Cf and ^{244}Cf were compared with those presented so far. We found that the ^{238}U(^{12}C, 5n)^{245}Cf and ^{238}U(^{12}C, 6n)^{244}Cf cross section was one order of magnitude lower than those reported.

An alumina disk, namely Al_2O_3, is normally used as a beam profile monitor for irradiation of ion beams in many accelerator facilites; and the durability of the irradiation is therefore well known. A membrane filter of an Al_2O_3 disk (60 μm in an average membrane thickness, which is 25 μg/cm^2) for use in chemical separations (*i.e.*, for

precipitation) can be directly utilized as the target backing to irradiate. A sample of ^{238}U (^{nat}U) in 6 N 100 ml of nitric acid solution (1 g ^{238}U/100 ml) was diluted with pure water to a concentration of ^{238}U of 155 mg/100ml. The diluted HNO_3 solution (6.2 ml) containing 9.6 mg of ^{238}U was collected in another beaker. A few drops of phenolphthalein were added to the solution to verify its pH levels. Ammonia water at a concentration of 25% (pH ~10) was added to the solution, whose alkalinity was then determined by phenolphthalein. Water was added to give a total volume of 9.6 ml (1 mg ^{238}U/ml). The solution was allowed to stand for at least 30 min due to the growth of uranium crystals (uranium hydroxide). The solution of exactly 900 μl containing the 900 mug ^{238}U as a hydroxide was partially collected in a separate beaker, and diluted by 2-3 ml of water. Finally, the diluted solution was filtrated using a membrane filter (Anodisc 25) distributed commercially by Whatman Co., Ltd. The ^{238}U hydroxide was then deposited on the Anodisc. The Anodisc (pore size, 0.1 μm; diameter, 20 mm; an effective thickness, 25 μm) used is an alumina filter, namely Al_2O_3, therefore it is resistant to strong beamstraggling and heat under severe conditions caused by beam irradiation. The chemical yield of the filtration was estimated to be approximately 100%. The prepared target was baked with an electric furnace at 500 °C to oxidize the precipitate to UO_2.

Recently, a He-gas jet transport system was installed at the CYRIC for producing heavy elements above Z=100. The target was mounted in an aluminum holder and placed in the He-gas jet reaction chamber on the end of a beam course. The reaction chamber was connected to the He-gas (containing KCl clusters) jet transport system. The He-jet recoil-transport system can be used with multi-targets. Here, only one Anodisc target with deposited ^{238}U (260 μg/cm^2) was placed in the reaction chamber. He-gas (flow rate, 3 l/min) was applied through a KCl-cluster generator at 640 °C.

Reaction products were recoiled out from the targets by nuclear reactions, and kinetic energies were reduced in He-gas containing KCl clusters. The products adsorbed on the cluster were then transported with He-gas through a capillary tube (15 m long) to an automated rotating-wheel chamber placed in the room next door. Six α-ray detectors equipped with a PIN-photodiode were installed in the rotating-wheel chamber to measure the α-rays emitted from the transported nuclides. Each detector was calibrated by means of the α-rays of ^{228}Th source and its daughters. The products transported by He-gas were blown onto polyethylene terephthalate films. The transport efficiency of the system was estimated to be 50%, which was obtained in the test run in the $^{197}Au(\alpha, 4n)^{197}Tl$ reaction.

Irradiation was carried out at an incident energy of 120 MeV. After degradation of the energy through two sets of harver-foils, each for the vacuum window and the irradiation chamber, Anodisc target was irradiated by the degraded energies. The beam current was typically 150 particle-nA. Accumulation of the products on rotating-wheel and measurements of the α-rays of ^{245}Cf and ^{244}Cf was repeated at 10 min intervals. The data were stored using a PC-CAMAC system and analyzed with a number of computer programs.

The α-ray spectrum of ^{245}Cf and ^{244}Cf, produced by the ^{238}U (^{12}C, 5n) and ^{238}U(^{12}C, 6n) reactions, respectively, is shown in Fig. 1. It was found that clear peaks of the α-rays of ^{245}Cf and ^{244}Cf were observed around 7.0-7.2 MeV. In previous research, major α-ray peaks of ^{245}Cf and ^{244}Cf have been found to occur at 7.137 MeV and 7.218 MeV, respectively, with the ^{244}Cm(α, 3n) and ^{244}Cm(α, 4n) reactions[2,3]. This is consistent with the two peaks observed here at 7.14 MeV and 7.21 MeV, respectively, which can be attributed to the α-rays of ^{245}Cf and ^{244}Cf by the observed energies of the α-rays and their half-lives. Furthermore, only the peak at 7.14 MeV for ^{245}Cf α-decay and 7.21 MeV for ^{244}Cf α-decay were observed in the use of the Anodisc deposited with ^{238}U at an irradiation energy of 75 MeV and 90 MeV, respectively. Finally, we have obtained the cross section of the ^{238}U (^{12}C, 5n) and ^{238}U(^{12}C, 6n) in several irradiation energies on target. The excitation functions of ^{245}Cf and ^{244}Cf are shown in Fig. 2 with those reported by Sikkeland et al[4]. as a function of laboratory energy system. We found that the cross sections for the ^{238}U (^{12}C, 5n) and ^{238}U(^{12}C, 6n) were estimated to be one order of magnitude lower than those reported. To date, only Sikkeland it et al. have reported so far the excitation functions of ^{245}Cf and ^{244}Cf by the ^{238}U (^{12}C, xn) reactions, although they do not present their α-ray spectra. The excitation functions for producing heavy elements such as ^{245}Cf, ^{244}Cf, and also heavier nuclides can be obtained by means of the Anodisc target.

Finally, we point out a method for target preparation. After irradiation, the surface deposited with ^{238}U changed to brown at the area irradiated by ^{12}C beams. However, it was found that the strength of the Anodisc target was sufficient to withstand the damage caused by beam irradiation. Therefore, the Anodisc seems to be useful as target backing for irradiation by several ion beams.

References

1) Mitsugashira, T., et al., private communication.
2) Magara M., Shinohara N., Hatsukara Y., Tsukada K., Iimura H., Usuda S., Ichikawa S.I., Suzuki T., Nagame Y., Kobayashi Y., and Oshima M., Radiochim. Acta **72** (1996) 39.
3) Fields P.R., Barnes R.F., Sjoblom R.K., and Milsted J., Phys. Lett. **24B** (1967)340.
4) Sikkeland, T., Maly, J., and Lebeck, D., Phys. Rev. **169** (1968) 1000.

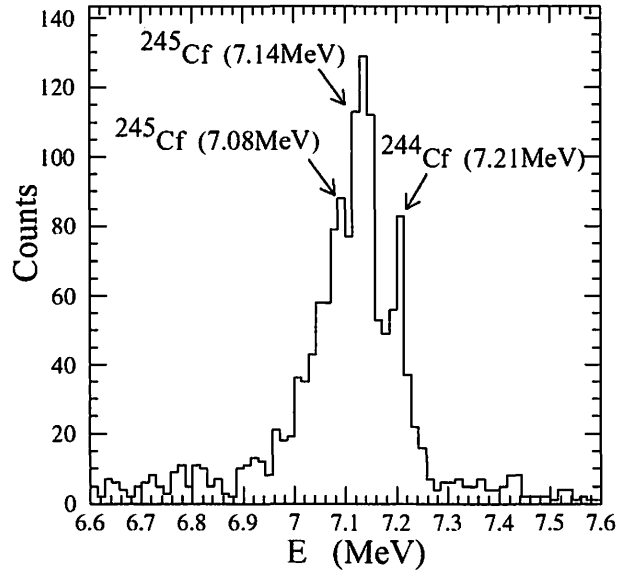

Fig. 1. The α-ray spectrum of ^{245}Cf and ^{244}Cf produced by the ^{238}U(^{12}C, 5n) and ^{238}U(^{12}C, 6n) reactions.

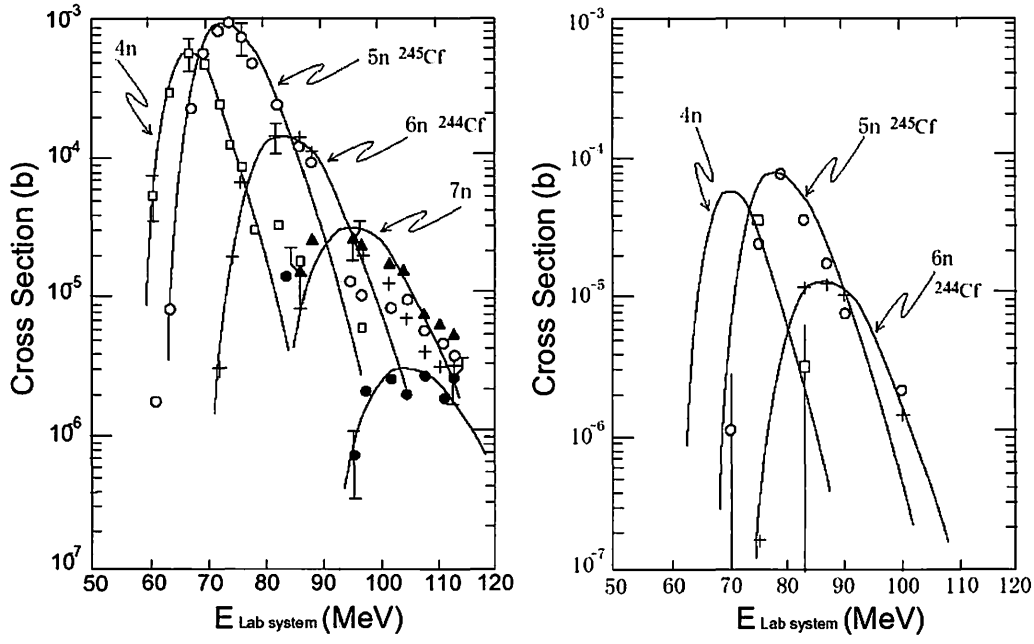

Fig. 2. (Left) Experimental cross section for ^{245}Cf and ^{244}Cf by the ^{238}U (^{12}C,xn) reactions reported by Shikkeland et al., (Right) same as left, but obtained by the present experiments.

VI. 4. Measurement of the Cross Section of the $^{40}Ar(\alpha,2p)^{42}Ar$ Reaction

Yuki H., Sato N.[*], *Ohtsuki T., Shinozuka T.*[*], *Baba M.*[*], *Ido T.*[*], *and Morinaga H.*[**]

Laboratory of Nuclear Science, Tohoku University
[*]*Cyclotron and Radioisotope Center, Tohoku University*
[**]*Technische Universitat München*

Introduction

Radioactive isotopes are great important not only for research in basic science, material science, medical and radiopharmaceutical use but also for education in those area. ^{42}K is one of the convenient sources of β^-- and/or γ-rays for several practical use, and that is produced by β^--decay from ^{42}Ar. Half lives of the ^{42}Ar and the ^{42}K are 33 years and 12 hours, respectively, therefore the correlation between the ^{42}Ar and the ^{42}K is in a secular equilibrium. The ^{42}Ar-^{42}K generator has been proposed by Morinaga as a useful source for school education of radiation and/or radioactivity. Two reactions, one for $^{40}Ar(t, p)^{42}Ar$ and another for $^{40}Ar(\alpha,2p)^{42}Ar$ reactions, can be considered for the production method of the ^{42}Ar. However no tritium accelerator is available nowadays. Therefore, the $^{40}Ar(\alpha, 2p)^{42}Ar$ reaction can be applied to produce the ^{42}Ar-^{42}K generator even though the reaction cross section might be smaller than that of the $^{40}Ar(t, p)^{42}Ar$ reaction. No excitation function of the $^{40}Ar(\alpha, 2p)^{42}Ar$ reaction experimentally measured have been reported so far. In the present study, we have measured the excitation function of the $^{40}Ar(\alpha, 2p)^{42}Ar$ reaction in order to produce the ^{42}Ar efficiently[1,2].

Experimental

Figure 1 shows a schematic view of the target system. Target cells made of quartz glass are 30 mm in long and 30 mm in an inside diameter with windows of 0.05 mm polyimide foils (Kapton, Goodfellow Metals, England). After evacuation, the cells were filled with natural Ar-gas up to 1 atm and the gas inlets of cells were stuffed with rubber plug and sealed with epoxy resin. Four cells were set in a cylindrical cell-holder frame at

the beam course of CYRIC for irradiation with the α-beams. Irradiations have been carried out two times in each beam energy of E_α =50, 60 and 70 MeV in order to check the reproducibility of the measurement values. Cupper foils of 0.01 mm in thickness are set between each cell in order to degrade the energy of α-beams. The α-beams from the AVF cyclotron are collimated in 10mmϕ, and passed through a 0.012 mm Harvar foil which is for the separation of vacuum of the beam line. In upper stream of the target cells, Harvar-foil of 0.01 mm was also set in order to cool the foils by He-gas. After passing through the four target cells, the α-beams were stopped in a Faraday-cup by the end of cell-holder frame. The irradiation time was about 7-9 hours by about 500 nA beam current.

After irradiation, the each cell was measured by a Ge-detector coupled with 4096 multichannel analyser. Since the emission probability of γ-ray accompanied with the β-decay of ^{42}Ar is 0 %, the ^{42}Ar itself can not be measured by the γ-ray spectroscopy. Instead, amount of the ^{42}Ar can be estimated by the 1524 keV γ-ray activity emitted from the ^{42}K as a correlation of secular equilibrium. However, the ^{42}K was also produced directly by the ^{40}Ar(α,pn)^{42}K reaction during the irradiation, therefore, the ^{42}K decayed from the ^{42}Ar can be measured after decaying out the primary ^{42}K in several weeks later.

In order to calculate the cross section from the amount of the radioactivity of γ-ray, the efficiency of Ge detector should be known. Since the decay rate of the ^{42}Ar was very small, the target cells are placed close to the detector in order to accumulate sufficient yields of the γ-ray emitted by the ^{42}K. Therefore, it was difficult to determine the efficiency of the detector, because the ^{42}K nuclides in the target cell were not regarded as a point source. Here, the primary ^{42}K was used to determine the efficiency by changing the distance between the source and Ge-detector (considering the geometrical effect).

The counting rate of 1524 keV γ-ray was decreased as a function of the half-life of the primary ^{42}K produced directly by the ^{40}Ar(α, pn)^{42}K reaction. Then, after several weeks, the counting rate became almost constant. Therefore, amount of the ^{42}K produced by the ^{40}Ar(α, 2p)^{42}Ar reaction can be measured with no interference of the primary ^{42}K.

Cu foils for the degradation of beam energy were also used as the beam current monitor. Total dose of the beam current evaluated by the excitation functions of the ^{65}Cu(α, 2n)^{67}Ga reaction[3,4] were consistent with that measured by Faraday-cup within the errors originated from uncertainties in the excitation functions.

Results and Discussion

The cross sections measured in the $^{40}Ar(\alpha, 2p)^{42}Ar$ and $^{40}Ar(\alpha, pn)^{42}K$ reactions are shown in Fig.2, which were the values averaged by two runs in the same beam energy. The errors were estimated by the different value performed in two runs. The incident energies of α-particles for each target cell were determined by the calculated energy degradation in Ar-gas, air, Harvar, polyimide and Cu foils using TRIM code[5]. Errors in the energy scale were indicated by the calculated energy degradation and the beam straggling in Ar-gas in the each target cell.

The excitation function of the primary ^{42}K in the local energy region presented by Tanaka *et al.*[6] is also shown in Fig. 2. It seems that the present value for the $^{40}Ar(\alpha, pn)^{42}K$ reactions is smoothly connected to that presented by Tanaka *et al.* even though the different techniques used each other. The calculated values of the cross sections using ALICE code[7] are also given in Fig. 2. As can be seen in the figure, the values calculated by the ALICE code may be overestimated in the $^{40}Ar(\alpha, 2p)^{42}Ar$ reaction in the lower energy region, and that may be underestimated in the $^{40}Ar(\alpha, pn)^{42}K$ reaction in the higher energy region. The experimental results show that the cross section of the $^{40}Ar(\alpha, 2p)^{42}Ar$ reaction becomes still larger as increase the beam energy. In order to estimate the probable production rate of the ^{42}Ar for the generator, experimental investigation in the extended energy region are needed.

References

1) Nozomi S. et al., CYRIC Annual Report 2003 p. 127.
2) Yuki H. et al., CYRIC Annual Report 2003 p. 130.
3) Bonesso O., Ozafran M J., Mosca H O., J. Radioanal. Nucl. Chem. **152** (1991) 189.
4) Mukherjee S., Kumar B B., Singh N L., Pramana J.Phys. **49** (1997) 253.
5) Ziegler J.F., Biersack J.P., Littmark U., "The stopping and range of ions in solids", Pergamon, New York (1984).
6) Tanaka S, Furukawa M., Mikumo T., Iwata S., Yagi M., Amano H., J. Phys. Soc. Jpn **15** (1960) 952.
7) Blann M., Vonach K.H., Phys. Rev. C **28** (1983) 1475.

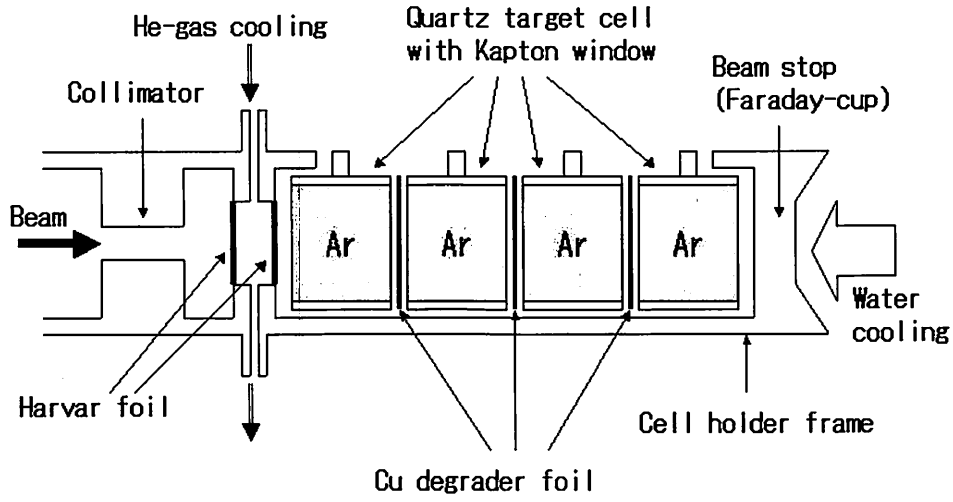

Figure 1. Schematic view of the target system for irradiation of gas target cells.

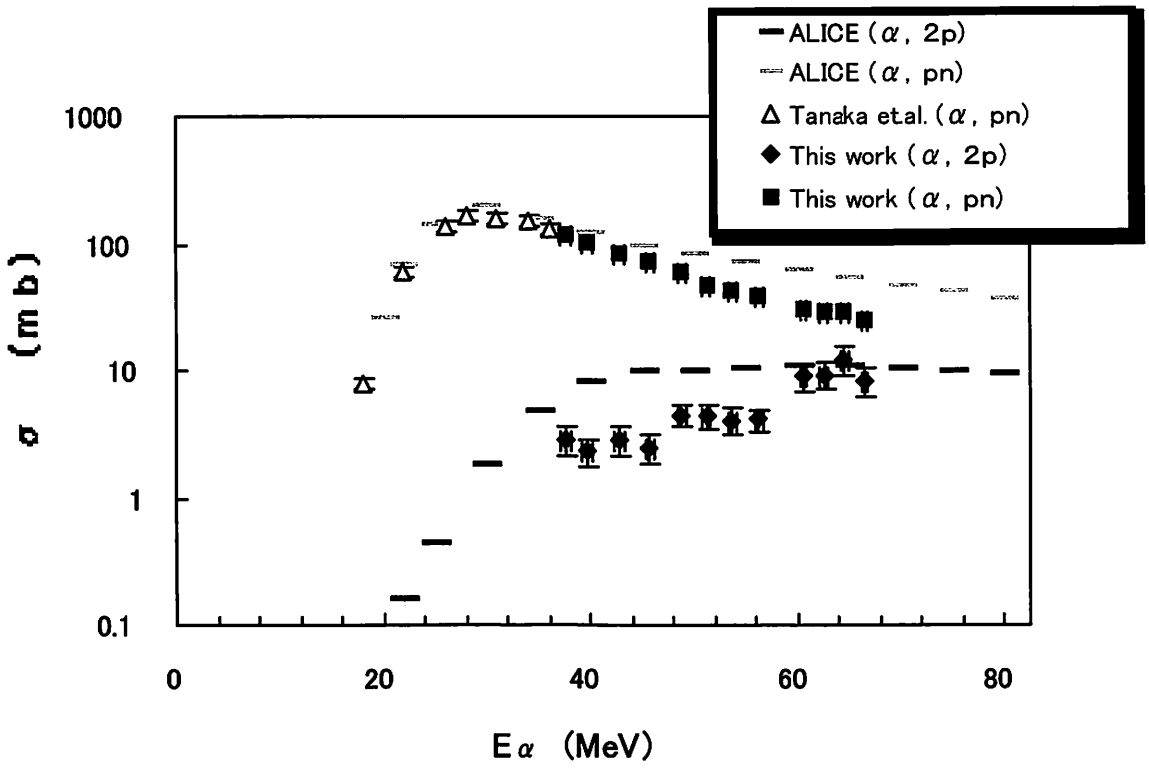

Figure 2. Comparison of the experimental and calculated excitation functions for the (α, 2p) and (α, pn) reaction on the target of ^{40}Ar.

VII. RADIOPHARMACEUTICAL CHEMISTRY AND BIOLOGY

VII. 1. A Comparison of Technetium and Rhenium Uptake by Plants

*Tagami K., Uchida S., and Sekine, T.**

Environmental and Toxicological Sciences Research Group, National Institute of Radiological Sciences
**Department of Chemistry, Graduate School of Science, Tohoku University*

Introduction

Technetium-99 (^{99}Tc) is of potential long-term importance in environmental dose assessment because it has a long half-life of 2.11×10^5 y and it is produced by thermal neutron fissions of ^{235}U and ^{239}Pu giving a relatively high fission yield (ca. 6 %), similar to that of ^{137}Cs. The most stable chemical form of Tc in the surface environment is pertechnetate, TcO_4^-, which has a high geochemical mobility and availability for plants[1,2]. The possible accumulation processes are Tc uptake with water mass flow (passive uptake) or active nutrient uptake (e.g., NO_3-, SO_4^{2-}, MoO_4^{2-} and $H_2PO_4^-$) by plants. A variety of transport proteins involved in anion uptake by plants might be involved in TcO_4- uptake[3]. However, these simple and passive pathways with water mass flow or active nutrient uptake cannot explain Tc accumulation in plants since no specific Tc transport sites in plant cells have been observed; There should be another active pathway for Tc, but how Tc is taken up is unclear. The authors hypothesized that Tc is abosrbed as a counter taken-up as a counter ion in plants. Thus, a tracer experiment, growing plants in a nutrient solution culture, was carried out to compare the plant uptake behaviors of Tc and major cations and anions from nutrient solution.

Materials and Methods

Three days after germination, plant seedlings of cucumber (n=5), radish (n=3), and a type of Chinese cabbage commonly eaten in Asian countries, called as qing gin cai (n=4) were grown in a nutrient solution prepared from a commercially available nutrient powder, HYPONeX®, which was dissolved in deionized water (1:1000 in weight). The plants were placed in a greenhouse at 21 °C and exposed to normal daylight conditions for about 3 weeks. Then, each plant was transplanted to a 120-mL plastic vessel containing 80-mL of

new nutrient solution with $^{95m}TcO_4$- and ReO_4- (a chemical analogue of Tc). The details of the apparatus were reported previously[4]. The plant samples were in contact with the solution through their fine roots for 3 days under normal daylight conditions.

After the contact, the nutrient solution was passed through a 0.22-μm filter and the concentrations of ^{95m}Tc in nutrient solutions were measured with an NaI(Tl) scintillation counter (Aloka, ARC-300). Concentrations of major elements (Na, K, Mg, Ca, P, and S) were measured by were ICP-OES, and Re and Cl were determined by ICP-MS. For plant samples, the fine roots were rinsed with deionized water and then the roots were gently wiped with paper towels. The plants were then separated into two to three parts, i.e., leaves, fleshy root and fine roots. The dried samples were placed in plastic tubes and the activity of ^{95m}Tc was measured with the NaI(Tl) scintillation counter.

Results and Discussion

In the nutrient solutions with three plant species (12 samples), concentrations of each major element, ^{95m}Tc and Re after cultivation (C) were compared with their initial concentrations (C_0) to show if the ion flux was greater than ($C/C_0<1$) or less than ($C/C_0>1$) water mass flow. After three days, relative concentrations (C/C_0) of Tc, K, Mg, Cl, and Re had excess ion fluxes, but other elements did not. The C/C_0 relationships for Na, K, Mg, Ca, P, S, Cl, and Re with C/C_0 for ^{95m}Tc are plotted in Fig. 1. High correlations of $R \geq 0.8$ ($p<0.01$) were apparent for K, Mg, Cl and Re. Rhenium is thought to be a chemical analogue of Tc, subsequently, C/C_0 for these elements were almost the same; indeed Re also showed high correlations with that of K ($R=0.92$, $p<0.01$). In radish plants, it was previously reported that Tc and Re behave similarly[4].

As written above, fluxes in excess mass flow were measured for K^+ and Mg^{2+}. To adjust the ionic balance to a suitable condition, counter anions are needed; it is known that Cl^- acts as a counter ion during K^+ fluxes, contributing to turgor of leaves. If these plants had absorption selectivity for Cl^- as a counter anion for K^+ and Mg^{2+}, then ReO_4^- and TcO_4^- would be retained in the nutrient solutions; however, the plants showed active absorption of both elements. Since ReO_4^- and TcO_4^- are stable in a nutrient solution and readily available to the plant, these ions can pass through nutrient anion transporters on the root surface, and accompany the excess nutrient cation flow. Possibly, ReO_4^- and TcO_4^- ions acted as substitutes for Cl^-. The ionic radii of Cl^- and TcO_4^- in aqueous solutions are close, being 1.81 Å and 2.40 Å, respectively[5]; consequently they may act similarly. Though ReO_4^- data have not been reported, the ionic radius should be close to that of TcO_4^-.

The absorbed ^{95m}Tc distributions and concentration factors ("Tc concentration in a plant part [Bq g^{-1}-dry]" / "Tc in the initial nutrient solution [Bq mL^{-1}]") in plant parts are shown in Fig. 2. The concentration factors of 41-77 for leaves and 33-56 for fine roots were observed after 3 d contact. The data were similar to those reported previously[4] when they were calculated on a wet weight basis. Since dry weights of leaves and fine roots were different, distribution ratio, which is defined as "Tc content in a plant part" divided by "total absorbed Tc" was calculated and the results are also shown in Fig. 2. Although these plants made contact with the nutrient solution through fine roots, most of the Tc was found in the upper parts, especially in the leaves. In plants, TcO_4^- and ReO_4^- can move up through the xylem. They would be accompanied by K^+ or other cations, and finally Tc and Re would be translocated to the leaves, where their chemical forms would be changed to organic forms[6]. Through this active uptake mechanism together with the passive uptake with water mass flow or active nutrient uptake, Tc could be highly accumulated in plants, though it is not an essential element.

This paper has been condensed from the article in *Chemosphere* **60**, 714 (2005).

References

1) Coughtrey P.J., Jackson D., Thorne M.C., 1983. Radionuclide distribution and transport in terrestrial and aquatic ecosystems, a critical review of data, vol. 3. AA Balkema, Rotterdam.
2) IAEA, 1994. Handbook of parameter values for the prediction of radionuclide transfer in temperate environments, IAEA technical reports series, No. 364. IAEA, Vienna.
3) Bennett R., Willey N.,. J. Environ. Radioactiv. **65** (2003) 215.
4) Tagami K., Uchida S., Appl. Radiat. Isotopes **61** (2004) 1203.
5) Neck V., Kanellakopulos B., Radiochim. Acta **42** (1987) 135.
6) Krijger G.C., Kollöffel C., Wolterbeek H.T., J. Environ. Qual. **29** (2000) 866.

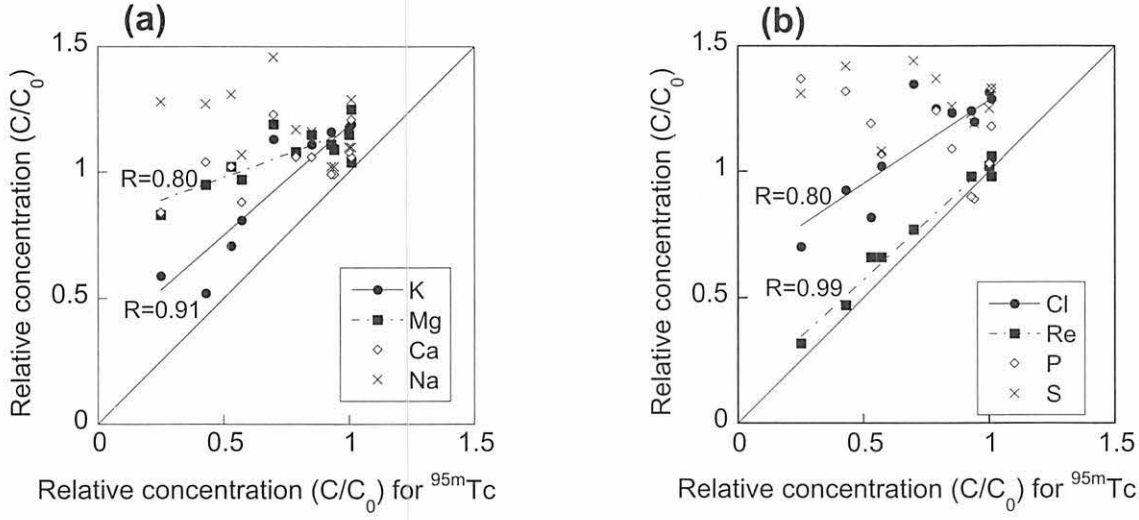

Figure 1. Relationships between concentration ratios (C/C_0) of ^{95m}Tc and (C/C_0) of (a) K, Ca, Na and Mg, (b) Cl, Re, S and P, which remained in nutrient solution after 3 d contact with three plant species (n=12). Lines for K, Mg, Cl and Re show correlation curves.

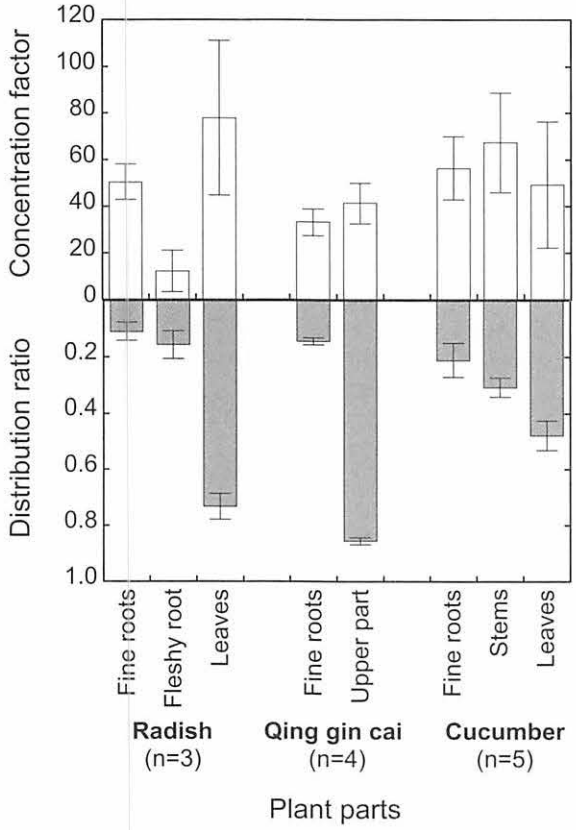

Figure 2. Distribution ratio of absorbed Tc in plant body and concentration factors after 3 d contact (n=3-5). Error bars show 1 s.d. of replicates.

VII. 2. Automated Preparation of *O*-[^{11}C]methyl-L-tyrosine Using Miniature Valves on a Manifold

Ishikawa Y., Iwata R., Furumoto S.[*], *Pascali C.*[**], *Bogni A.*[**], *Kubota K.*[***], *and Ishiwata K.*[****]

Cyclotron and Radioisotope Center, Tohoku University
[*]*TUBERO, Tohoku University*
[**]*National Cancer Institute, Milan*
[***]*International Medical Center*
[****]*Tokyo Metropolitan Institute for Gerontology*

Among several novel positron-emitting tyrosine analogues proposed for imaging amino acid transport in these few years, the synthetic ^{18}F-labeled amino acid, *O*-(2-[^{18}F]fluoroethyl)-L-tyrosine[1], and its analogues, *O*-(3-[^{18}F]fluoropropyl)-L-tyrosine[2] and *O*-[^{18}F]fluoromethyl-L-tyrosine[3], have gained increased interest. Although fluorine-18 is generally the preferred choice for distribution and multi-dose production due to its longer half-life of 109.8 min, carbon-11 still retains some potential if an efficient and simple radiosynthesis is possible. Furthermore, since biological information (toxicity, metabolism, etc.) on fluoro-analogues is not often available, more workload is needed for introducing the fluoro-tracers in clinical practice. *O*-[^{11}C]Methyl-L-tyrosine ([^{11}C]MT) was prepared using [^{11}C]CH_3OTf[3] and more recently its first clinical evaluation has been carried out with promising results[4].

Automated preparation is one of the requisites to routine clinical application of short-lived PET radiopharmaceuticals. This is more rapidly and easily achieved when the radiosynthesis is simpler. Such an automated module is installed in a shielded box (hot cell) which is small but expensive and thus compact design is strongly desired. In the present study the purification procedure of [^{11}C]MT was simplified by replacing an HPLC purification with a conventional column chromatographic separation using commercial solid phase extraction (SPE) cartridges. The automated module was miniaturized using small valves assembled a manifold block.

[^{11}C]Methyl iodide (MeI) was produced with a MeI MicroLab system (GE) by gas phase iodination via [^{11}C]CH_4. *O*-[^{11}C]Methyl-L-tyrosine was prepared according to the

scheme shown in Fig. 1[3]. Briefly, a solution of L-tyrosine disodium in DMSO (3 mg/0.3 mL, Sigma) was bubbled in a small vial with [^{11}C]MeI carried by He flow (50 mL/min) at room temperature. The reaction was then quenched by adding water (2 mL) and the resulting mixture was injected onto two combined cartridges of Sep-Pak Plus tC18 (Waters) and Bond Elut Jr. SCX (Varian). The cartridges were then eluted with saline at a flow rate of *ca.* 5 mL/min. A fraction of [^{11}C]MT was collected in a sterile vial through a membrane filter.

A block of PEEK (width 126 x depth 94 x height 35 mm) was designed to assemble 10 miniature, manifold-mountable, solenoid valves (EVX, Takasago Elec. Co.), a 3-mL glass reaction vessel (Reacti-vial, Pierce), the two combined SPE cartridges and a 5-mL vial for water according to the flow diagram shown in Fig. 2. A solenoid operated Teflon micro pump (110TP, Bio-Chem) was adopted for eluting the SPE cartridges with saline. A small radioactivity sensor (S-1726, OKEN) was used for monitoring the radioactivity eluted from the cartridges.

An injectable saline solution of [^{11}C]MT was obtained directly from the SPE cartridges within 30 min after EOB. Radiochemical yield was ca. 60% (decay-corrected, based on [^{11}C]MeI) and radiochemical purity over 97%. The combined use of SPE cartridges worked well to separate [^{11}C]MT from DMSO, L-tyrosine and some radioactive by-products as demonstrated in Fig. 3. A low-cost micro-pump was introduced to carry out a reproducible chromatographic separation on the SPE cartridges. The [^{11}C]MT fraction was collected in 15-20 mL of saline. Thus, the purification of [^{11}C]MT with SPE instead of HPLC considerably simplified the preparation and accordingly adapted it to automation.

Manifold valves are generally used to reduce internal volumes and external connections between valves. These features bring the following further advantages: reduction of material loss; ease and rapidness in cleaning after synthesis; and capability of compact design. In Fig. 4 is shown a photographic view of the miniature module dedicated to the synthesis of [^{11}C]MT, in which valves, tubing, connectors, cartridges and reaction vial combined into a single, pre-assembled component.

The automated miniature module was installed at International Medical Center July 2004 and since then it has been used for clinical study of [^{11}C]MT.

References

1) Wester H.J., Herz M., Weber W., Heiss P., et al., J. Nucl. Med. **40** (1999) 205.
2) Tang G., Wang M., Tang X., Luo L., Gan M., Nucl. Med. Biol. **30** (2003) 733.
3) Iwata R., Furumoto S., Pascali C., Bogni A., Ishiwata K., J. Label. Compd. Radiopharm. **46** (2003) 555.
4) Ishiwata K, Tsukada H, Kubota K, et al., Nucl. Med. Biol. **32** (2005) 253.

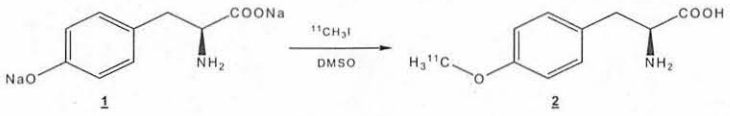

Fig. 1. Synthesis scheme of [^{11}C]MT.

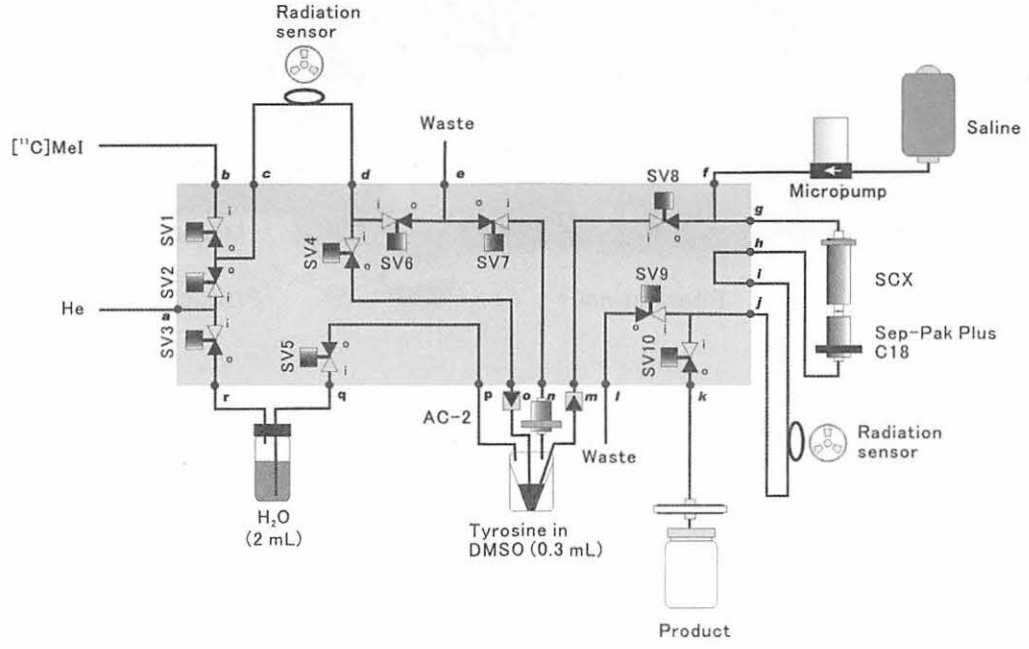

Fig. 2. A schematic diagram of a miniature module.

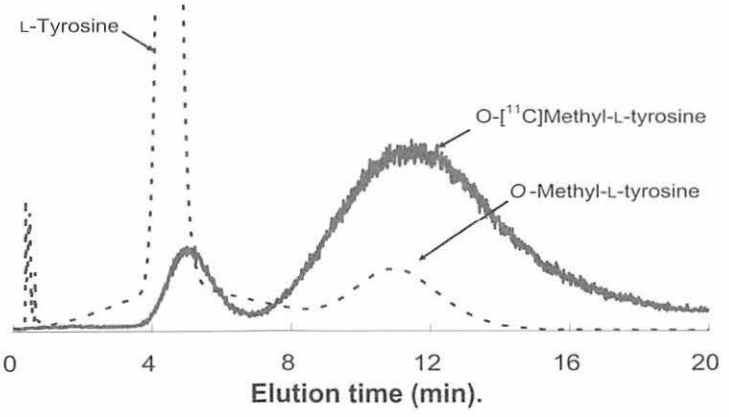

Fig. 3. A typical elution profile of [^{11}C]MT.

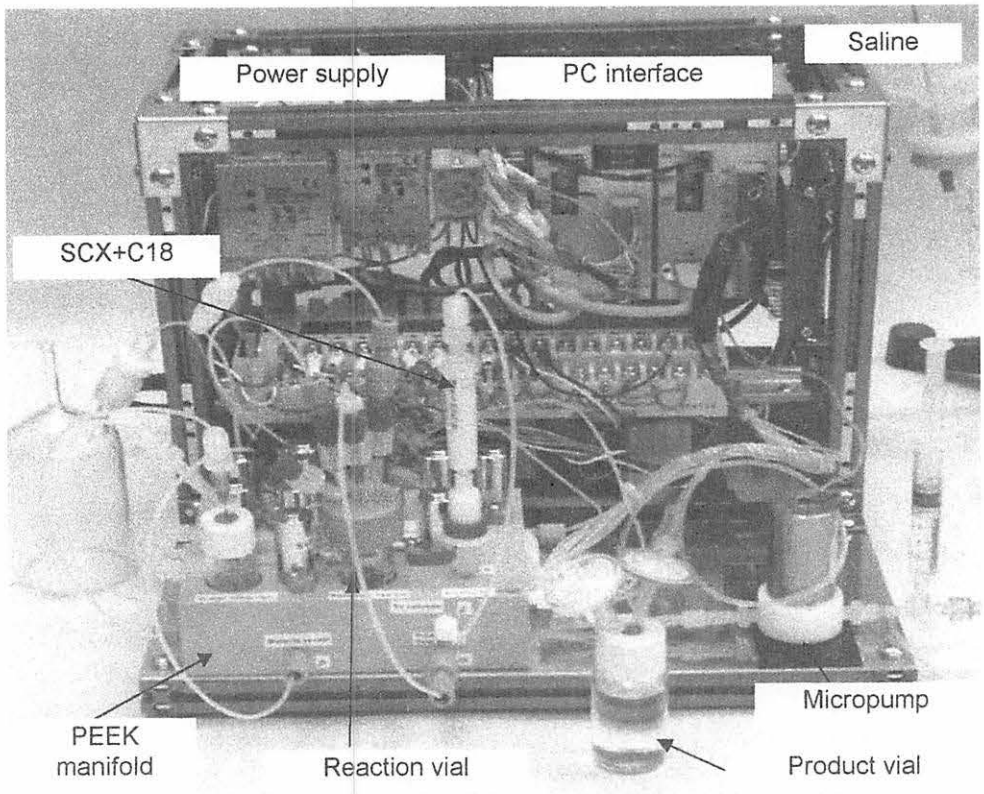

Fig. 4. A photographic view of the miniature module.

VIII. NUCLEAR MEDICINE

VIII. 1. Correlation of FDG Accumulation in the Frontal Cortex with Fractional Anisotropy in the Corpus Callosum.

Inoue K., Ito H., Ito M., and Fukuda H.*

Department of Nuclear Medicine and Radiology, IDAC, Tohoku University
**Cyclotron and Radioisotope Center, Tohoku University*

Introduction

The aging process is thought to result in changes in synaptic activity, reflecting both functional and structural cell derangement. Positron emission tomography and ^{18}F-fluoro-D-deoxyglucose (^{18}F-FDG) has been used to measure glucose utilization of the brain, which reflect activity of neural cells. Several PET studies of brain glucose metabolism have reported regional and global declines[1,2], whereas a recent study has suggested the declines might reflect brain atrophy[3].

Neural function of signaling is carried out by interconnection of neurons via neuronal fibers. For examinations of the integrity of the microstructure of cerebral white matter, diffusion-tensor imaging (DTI) is recently becoming an established technique that provides information on tissue microstructure and architecture for each voxel[4-6]. Among several quantitative measures provided by DTI, fractional anisotropy (FA)[7] is an index of the orientational coherence of water diffusion, and higher in regularly organized tissues, such as the corpus callosum and pyramidal tract, whereas lower in tissues where fiber orientations are more inhomogeneous such as crossing fibers and degenerated fibers, and much lower in more isotropic regions such as in gray matter and in cerebrospinal fluid (CSF) space[8-12]. Several studies focusing on normal aging have reported significant reduction in FA of the whole brain[13], of the corpus callosum and the centrum semiovale[14], as well as of the deep white matter regions[8,10]. Some studies have also demonstrated an anterior-posterior gradient in the effect of normal aging in the white matter and the corpus callosum[8,10,15]. The decline of FA of the white matter with aging has been considered to reflect loss of nerve fibers and degeneration of myelin[16].

In the present study, we aimed to examine whether degradation of microstructure of

fiber tracts was associated with change in the glucose metabolism in the brain evaluated by ^{18}F-FDG-PET in the normal elderly subjects. For the aim of this study, we measured FA of the genu and splenium of the corpus callosum and deep white matter of the frontal and occipitoparietal lobe bilaterally to examine association with microstructure of the fiber tract with regional ^{18}F-FDG accumulation in the brain. We also examined whether there was correlation between FA with gray matter (GM) atrophy measured by using voxel based morphometry (VBM)[17,18] that may cause apparent correlations between FA with ^{18}F-FDG accumulation by partial volume effects.

Methods

Subjects

Nineteen healthy elder volunteers (11 males, 8 females, mean age 73.3±2.5 yr, range 70-78 yr) participated. They were recruited from participants in a research program on brain aging in city dwellers conducted by the Tohoku University. Only those who did not have a history of a major medical, neurological, or psychiatric disease, and had normal T1- and T2- weighted MR brain images, or minor hyperintensities on a T2-weighted image in deep white matter or periventricular white matter, were recruited for the present study. Written informed consent was obtained from all the subjects after a proper explanation of the study being conducted, according to guidelines approved by Tohoku University and the Code of Ethics of the World Medical Association (Declaration of Helsinki).

PET

All subjects fasted for at least 5 hours before injection of ^{18}F-FDG of approximately 214 MBq. The blood glucose level was measured before an injection, which were 99±13 mg/dl. PET scans were obtained using a SET2400W scanner (Shimadzu Inc., Kyoto, Japan), which acquired 63 planes simultaneously over a 200-mm axial field of view (FOV) with a spatial resolution of 4.5 mm at full width at half maximum (FWHM)[19]. An emission scan was obtained for 10 min, beginning 45 min after the injection. Subjects were instructed to stay quietly on a sofa with their eyes closed in a dimly lit room from the injection to the scan. A transmission scan was obtained for 7-10 min with ^{68}Ge/^{68}Ga rod source for attenuation correction after the tracer injection. PET images were reconstructed by filtered back projection using Butterworth-ramp filter (order 2, cutoff frequency 8 mm) with measured attenuation, dead time, and decay correction factors.

MR

All MR imaging studies were performed using a Symphony 1.5-Tesla system (Siemens, Erlangen, Germany). A three-dimensional volumetric T1-weighted image (T1WI) was obtained as a gapless series of thin transverse sections using a MPRAGE sequence (TE/TR, 5.5/2180 ms; flip angle, 30°; 25-cm FOV; acquisition matrix, 256×256; slice thickness, 1.5 mm). DTI was acquired using a single-shot diffusion-weighted spin-echo echo planar imaging (TE/TR, 115/5600; NEX , 4; acquisition matrix, 128×128; 25 cm FOV, and 30 5.0 mm thick contiguous axial slices with 0.5 mm interslice gap). The diffusion tensor was acquired for each slice with six sets involving diffusion gradients placed along non-collinear directions (b = 1000 seconds/mm^2): (x,y,z) = [(1,1,0), (0,1,1), (1,0,1), (-1,1,0), (0,-1,1), (1,0,-1)], and an individual set without diffusion weighting (b = 0 seconds/mm^2; b0 image)[20]. DTIs were processed offline using a Dr. View/LINUX software (Asahi Kasei Information Systems Co., Ltd., Tokyo, Japan) to create a FA image[7].

Image processing

Image processing for PET image and T1WI were performed using SPM2 software (http://www.fil.ion.ucl.ac.uk/spm/). Each PET image was co-registered to a corresponding T1WI image. Linear and non-linear parameters for anatomical normalization to the ICBM 152 template T1WI (Montreal Neurological Institute) were estimated for each T1WI, and applied to anatomical normalization of both PET image and T1WI[21]. A T1WI was then segmented into an image of GM, white matter and CSF. PET images were smoothed using a Gaussian kernel of 16mm full-width at half maximum (FWHM) to compensate individual anatomical differences. GM images were smoothed using a Gaussian kernel of 12mm for further VBM analysis.

ROI measurement of FA.

For each subject, six regions of interest (ROIs) were drawn on each b0 image using 3D ROI function of the MRIcro software (v. 1.38)[22]. ROIs were placed on the splenium (SCC) and genu (GCC) of the corpus callosum and the deep white matter in the frontal (F-DWM) and occipitoparietal (OP-DWM) lobe bilaterally (Fig. 1) using the b0 image, and overlaid on the FA image.

Analysis

Counts of PET images were globally normalized using proportional scaling.

Statistical analysis was performed using "single subject and covariate only" model of SPM2, with FA values for each ROI as a covariate. Statistical threshold was set at $P < 0.05$ (false discovery rate corrected for multiple comparisons)[23].

We also performed VBM of GM[17,18] to examine if there was correlation of GM concentration with FA that would be associated with correlation of FDG accumulation with FA using the same statistical model mentioned above.

Results

FA of each ROI was 0.64±0.07 for the GCC, 0.73±0.07 for the SCC, 0.24±0.03 and 0.27±0.03 for the right and left F-DWM, 0.36±0.05 and 0.33±0.06 for the right and left OP-DWM, respectively. We found statistically significant positive correlation with FA in the GCC and regional FDG accumulation in the posterolateral frontal cortex bilaterally, and the anterior part of the left superior frontal gyrus (SFG) (Fig. 2, Table 1). We found no statistically significant correlation with FA in other ROIs. We did not find statistically significant correlation of the GM concentration with FA.

Discussion

In the present study, we measured FA of white matter fiber in the corpus callosum and DWM in the frontal and occipitoparietal lobe, and compared with FDG accumulation in the brain. We found that the FDG accumulation in the posterior lateral prefrontal cortex bilaterally and the anterior prefrontal cortex in the left hemisphere was positively correlated with FA in the GCC, i.e., the regional FDG accumulation was decreased in subjects who has lower FA of the GCC. Several studies have shown that apparent regional decrease in brain FDG uptake or cerebral blood flow could be resulted from partial volume averaging due to the brain atrophy[3,26]. The decreases in the FDG accumulation observed in the present study, however, was not resulted from partial volume effects, because we found no statistically significant GM atrophy which was correlated with FA. The GCC consist of fibers that connecting the lateral and medial surfaces of the frontal lobes[27]. The deterioration in fibers of the GCC would result to compromise in neural signaling between the frontal cortical regions of the each hemisphere connected via the GCC, and to decrease in neural activities in those regions. Among the cortical regions in which we detected decreases in FDG accumulation, the anterior SFG might send fibers to the GCC. The homotopic regions of the posterior prefrontal cortex where we found statistically significant correlation, however, have been considered to send fibers to the body of the corpus

callosum, not to the GCC[27,28]. The present findings could reflect indirect functional connections between the posterior and anterior prefrontal cortex, which sends fibers to the GCC. In the present study, subjects stayed in a resting state with their eyes closed without any control of subject's mental activity. Functional relationships of frontal cortices and mental activity of the subjects were, therefore, difficult to make straightforward interpretation. In conclusion, the present study demonstrated that deterioration in microstructure of the white matter fibers are associated with metabolic changes in the cerebral cortex without significant GM atrophy in the healthy elderly subjects.

References

1) Petit-Taboue,M.C., Landeau B., Desson J.F., Desgranges B., and Baron. J.C., Neuroimage **7** (1998) 176.
2) Moeller J.R., Ishikawa T., Dhawan V., Spetsieris P., Mandel F., Alexander G.E., Grady C., Pietrini P., and Eidelberg D., J. Cereb. Blood Flow Metab. **16** (1996) 385.
3) Ibanez V., Pietrini P., Furey M.L., Alexander G.E., Millet P., Bokde A.L., Teichberg D., Schapiro M.B., Horwitz B., and Rapoport S.I., Brain Res. Bull. **63** (2004) 147.
4) Le Bihan D., Nat. Rev. Neurosci. **4** (2003) 469.
5) Le Bihan D., Mangin J.F., Poupon C., Clark C.A., Pappata S., Molko N., and Chabriat H., J. Magn. Reson. Imaging **13** (2001) 534.
6) Sullivan E.V., and Pfefferbaum A., Eur. J. Radiol. **45** (2003) 244.
7) Basser P.J., and Pierpaoli C., J. Magn. Reson. **B 111** (1996) 209.
8) Head D., Buckner R.L., Shimony J.S., Williams L.E., Akbudak E., Conturo T.E., McAvoy M., Morris J.C., and Snyder A.Z., Cereb. Cortex. **14** (2004) 410.
9) Abe O., Aoki S., Hayashi N., Yamada H., Kunimatsu A., Mori H., Yoshikawa T., Okubo T., and Ohtomo K., Neurobiol. Aging **23** (2002) 433.
10) Pfefferbaum A., Sullivan E.V., Hedehus M., Lim K.O., Adalsteinsson E., and Moseley M.. Magn. Reson. Med. **44** (2000) 259.
11) Pierpaoli C., and Basser P.J., Magn. Reson. Med. **36** (1996) 893.
12) Pierpaoli C., Barnett A., Pajevic S., Chen R., Penix L.R., Virta A., and Basser P., Neuroimage **13** (2001) 1174.
13) Rovaris M., Iannucci G., Cercignani M., Sormani M.P., De Stefano N., Gerevini S., Comi G., and Filippi M., Radiology **227** (2003) 731.
14) Pfefferbaum A., and Sullivan E.V., Magn. Reson. Med. **49** (2003) 953.
15) O'Sullivan M., Jones D.K., Summers P.E., Morris R.G., Williams S.C., and Markus H.S., Neurology **57** (2001) 632.
16) Moseley M., NMR Biomed. **15** (2002) 553.
17) Ashburner J., and Friston K.J., Neuroimage **11** (2000) 805.
18) Good C.D., Johnsrude I.S., Ashburner J., Henson R.N., Friston K.J., and Frackowiak R.S.J., Neuroimage **14** (2001) 21.
19) Fujiwara T., Watanuki S., Yamamoto S., Miyake M., Seo S., Itoh M., Ishii K., Orihara H., Fukuda H., Satoh T., Kitamura K., Tanaka K., and Takahashi S., Ann. Nucl. Med. **11** (1997) 307.
20) Basser P.J., and Pierpaoli C., Magn. Reson. Med. **39** (1998) 928.
21) Ashburner J., and Friston K.J., Hum. Brain Mapp. **7** (1999) 254.
22) Rorden C., and Brett M., Behav. Neurol. **12** (2000) 191.
23) Genovese C.R., Lazar N.A., and Nichols T., Neuroimage **15** (2002) 870.
24) Bhagat Y.A., and Beaulieu C., J. Magn. Reson. Imaging **20** (2004) 216.
25) Madden D.J., Whiting W.L., Huettel S.A., White L.E., MacFall J.R., and Provenzale J.M., Neuroimage **21** (2004) 1174.
26) Meltzer C.C., Cantwell M.N., Greer P.J., Ben-Eliezer D., Smith G., Frank G., Kaye W.H., Houck P.R., and Price J.C., J. Nucl. Med. **41** (2000) 1842.

27) Nieuwenhuys R., Voogd J., and van Huijzen C., In: The human central nervous system - A synopsis and atlas. Berlin: Springer-Verlag; 1988.
28) Abe O., Masutani Y., Aoki S., Yamasue H., Yamada H., Kasai K., Mori H., Hayashi N., Masumoto T., and Ohtomo K., J. Comput .Assist. Tomogr. **28** (2004) 533.

Table 1. Regions where the peak of t values were observed.

Region	x	y	z	t
Lt. inferior frontal gyrus	-52	10	36	7.8
Lt. superior frontal gyrus	-28	52	32	5.9
Rt. middle frontal gyrus	48	4	38	6.3

(x, y, z): coordinates of standard space (Montreal Neurological Institute).

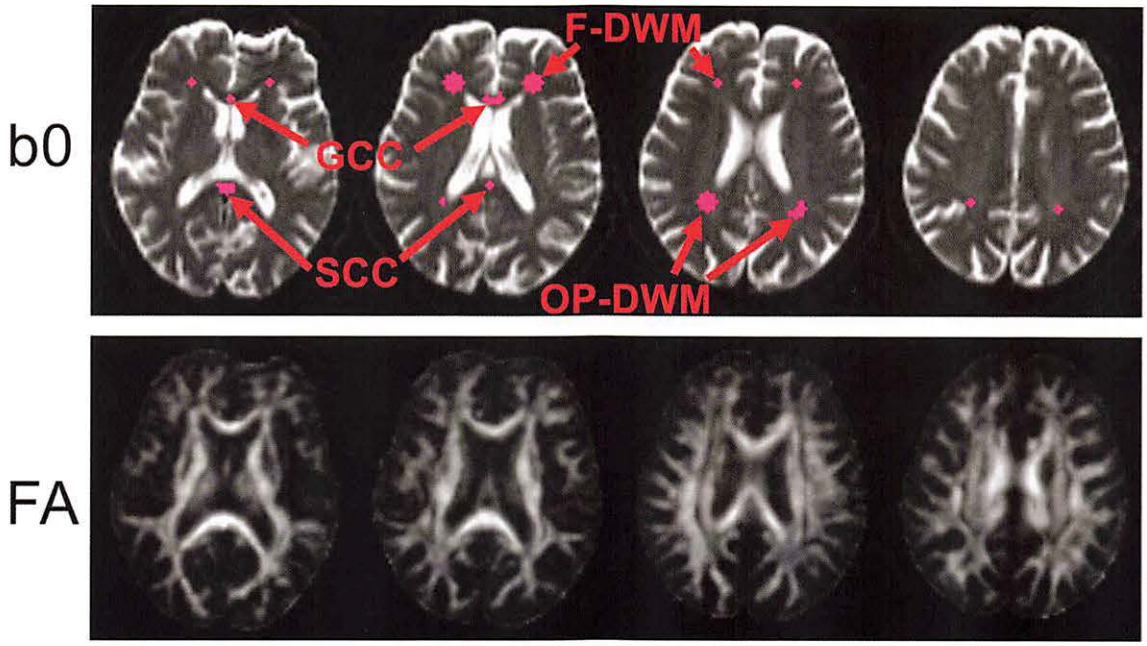

Figure 1. Regions of interest (ROIs) : placed for each subject's b0 image on the genu (GCC) and splenium (SCC) of the corpus callosum, deep white matter of the frontal (F-DWM) and occipitoparietal (OP-DWM) lobe. The ROIs were overlaid on the FA image for each subject.

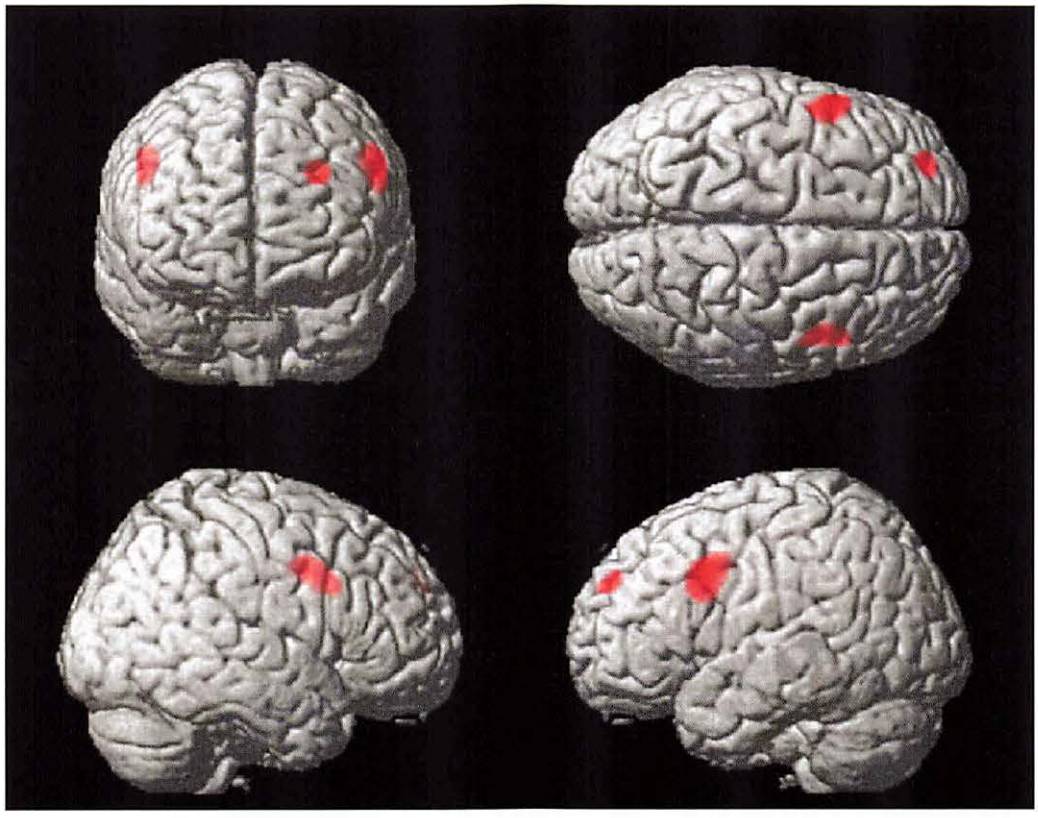

Figure 2. ^{18}F-FDG accumulation in the lateral prefrontal cortex showed statistically significant positive correlation with FA in the GCC ($P < 0.05$, corrected for multiple comparison).

VIII. 2. Differential Activation of the Human Brain in Response to Sham Stimulation after Experience of Visceral Stimulation

Hamaguchi T., Kano M., Kanazawa M., Rikimaru H., Watanabe S., Itoh M.*, Yanai K.**, and Fukudo S.*

Department of Behavioral Medicine, Tohoku University Graduate School of Medicine
**Division of Nuclear Medicine, Cyclotron Radio Isotope Center, Tohoku University*
***Department of Pharmacology, Tohoku University Graduate School of Medicine*

Introduction

Anticipation of pain is mechanism to prevent future harm by learning signs of impending pain[1-4], allowing avoidance of future painful events. Anticipation of an intense visceral stimuli induces activation of orbitofrontal cortex (OFC), PFC, perigenual ACC, thalamus, lentiform nucleus, and PAG region[5].

The placebo effects on the midbrain which contains endogenous opioids during analgesic anticipation[6]. Anticipation reduced ACC activity during the earlier phase of pain and the thalamic and the insula activity during the late phase of pain[6]. Previous studies provide that anticipation events on pain through the functional module of the brain.

Hypersensitivity to visceral stimulation is major pathophysiology of Irritable bowel syndrome (IBS)[7-9,10]. However, the brain area related to initial programming of sensitization provoked by the visceral perception is still unknown. This study clarified that brain activation due to sham colonic distention is different between experienced no stimulation and after experienced intense stimulation.

Methods

Subjects. This study was approved by the Ethics Committee of Tohoku University School of Medicine. All subjects gave written informed consent. Forty-five normal volunteers (12 female, 33 male, 20-26 years old, all right-handed) participated in the first study. All subjects were free from gastrointestinal disorder symptoms or signs.

PET scanning. rCBF in each subject was measured during 4 scans (70 seconds each)

using a PET scanner with [^{15}O] labeled water (HEADTOME V SET-2400W, Shimadzu, Japan).

The descending colon was distended with a computerized barostat pump (Medtronics Synectics, Shoreview, MN). To clarify the sensitization process to colonic distention, orders of stimuli was set with six different patterns as follows: group 1: sham - 20 - 40 (n = 8), group 2: sham - 40 - 20 (n = 7), group 3: 20 - sham - 40 (n = 7), group 4: 20 - 40 - sham (n = 8), group 5: 40 - sham - 20 (n = 8), group 6: 40 - 20 - sham (n = 7). No subject was informed of the order or intensity of stimuli.

After each stimulation, the subjects were asked to report the 7 items of visceral perception or emotion. Each sensation was evaluated on an ordinate scale.

Data Analyses

PET images were analyzed using SPM2 on a MATLAB platform. PET images were reconstructed using three dimensional filtered back projection algorithm[11-13]. Ordinate visceral perception and emotion were compared between groups with Mann-Whitney U test.

RESULTS

Visceral perception and emotional changes during sham stimulation in different order

In sham stimulation after 40 mmHg distention, abdominal discomfort ($Z = 1.86$, $p = 0.06$ corrected for ties; Mann-Whitney U test) and abdominal distention ($Z = 1.56$, $p = 0.11$) were not significantly but tended to be higher than sham stimulation without prior distention (group 4 and 5 vs 1 and 2 in sham, Fig. 1).

rCBF changes during sham stimulation in different order

The main effect of the sham stimulation (0 mmHg) after 40 mmHg distention, determined by comparison with group 4 add 5 and group 1 add 2, denoted activation of the right cingulate gyrus (Brodmann area; BA24, $Z = 4.16$, Fig. 2a), right insula (BA13, $Z = 4.08$, Fig. 2b), and right middle frontal gyrus (BA10, $Z = 3.92$, uncorrected for multiple comparisons $p < 0.001$, Fig. 2c).

Discussion

In this study, sham stimulation after the experience of 40 mmHg visceral stimulation activated right cingulate cortex (BA24), right insula (BA13), and right PFC (BA

10) compared to sham stimulation without experience of actual visceral stimulation. These brain areas are relevant to emotions and visceral perception[14-17]. Anticipation of an intense visceral stimuli induces activation of OFC, PFC, perigenual ACC, temporal cortex, thalamus, lentiform nucleus, and PAG region[5]). This response resembles brain activation by the actual rectal stimulus[5]). The placebo effects on the midbrain which contains endogenous opioids during analgesic anticipation[6]). Prior experience of intense stimuli might be evoked anticipation.

Regions in the medial and ventral areas of the frontal lobe seem to be especially important in relating information about external sensory stimuli to interoceptive information that represents emotional significance. Intensity of 40 mmHg distention might cause long lasting activation of PFC. An alternative interpretation is that the dorsolateral PFC redirects attention away from pain, as it has been implicated in general attentional processes[6,18]). Prior visceral stimuli with 40 mmHg possibly cause associated learning of the visceral perception through activation of cingulate cortex, insula, PFC, medulla, left OFC. As a result, PFC may be activated by sham distention after 40 mmHg distention.

REFERENCES

1) Rainville P., Duncan,G.H., Price D.D., Carrier B. and Bushnell M.C., Science **277** (1997)968.
2) Ploghaus A. et al., Science **18** (1999)1979.
3) Rainville P.,. Curr. Opin. Neurobiol. **12** (2002) 195.
4) Porro C.A., Cettolo V., Francescato M.P. and Baraldi P., Neuroimage **19** (2003) 1738.
5) Naliboff B.D. et al., Psychosom. Med. **63** (2001) 365.
6) Wager T.D. et al., Science **303** (2004) 1162.
7) Fukudo S. et al., J Gastroenterol **37 Suppl 14** (2002)145.
8) Fukudo S., Nomura T. and Hongo M., Gut **42** (1998) 845.
9) Kanazawa M., Nomura T., Fukudo S. and Hongo M., Neurogastroenterol. Motil. **12** (2000) 87.
10) Munakata J. et al., Gastroenterology **112** (1997) 55.
11) Colsher J.G., Phys. Med. Biol. **25** (1980) 103-15.
12) Stazyk M.W., Rogers J.G. and Harrop R.., Phys. Med. Biol. **37** (1992) 689.
13) Cherry S.R., Dahlbom M. and Hoffman E.J., Phys. Med. Biol. **37** (1992) 779.
14) Silverman D.H. et al., Gastroenterology **112** (1997) 64.
15) Mertz H. et al., Gastroenterology **118**,(2000) 842.
16) Hobday D.I. et al., Brain **124** (2001) 361.
17) Hamaguchi T. et al., Neurogastroenterol. Motil. **16** (2004) 299.
18) Peyron R. et al., Brain **122 (Pt 9)** (1999) 1765.
19) Price C.J and Friston K.J., Neuroimage **5** (1996) 261.

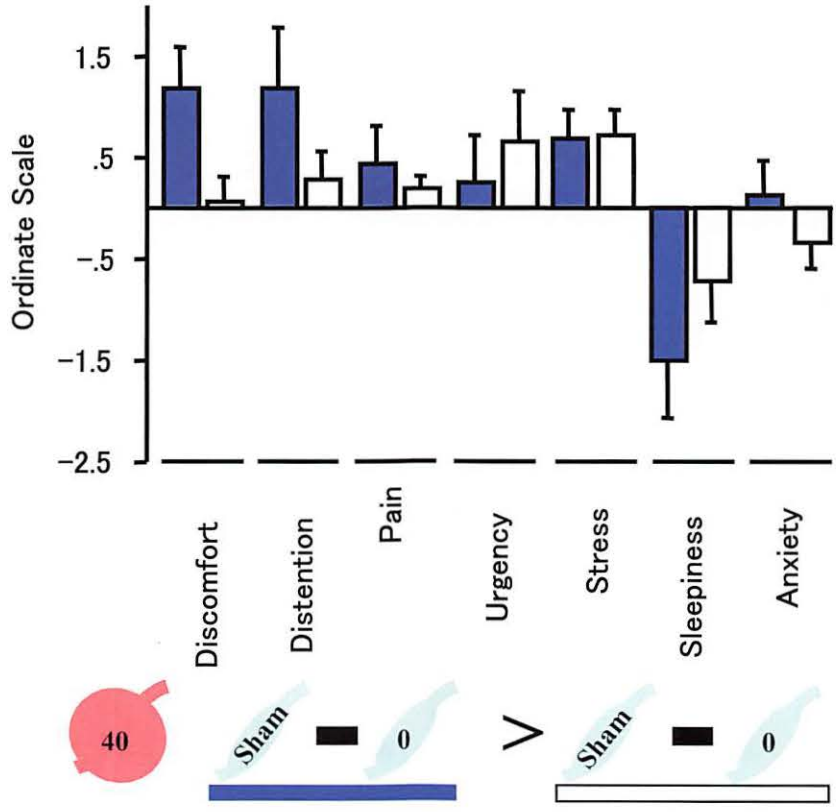

Fig. 1. Comparisons of visceral perception and emotion during stimulation minus baseline. Sham stimulation after 40 mmHg stimulation v.s. sham without prior stimulation. Solid bars (blue) indicated the combined group 4 and 5. Open bars were combined group 1 and 2 (mean and standard error). Vertical axis indicated the visceral perception and emotion changes from baseline of the ordinate scale. There were no significantly differences in the ordinate scale during sham stimulation between with intense stimuli and without prior stimuli. Statistical analyses was used by Mann-Whitney U-test.

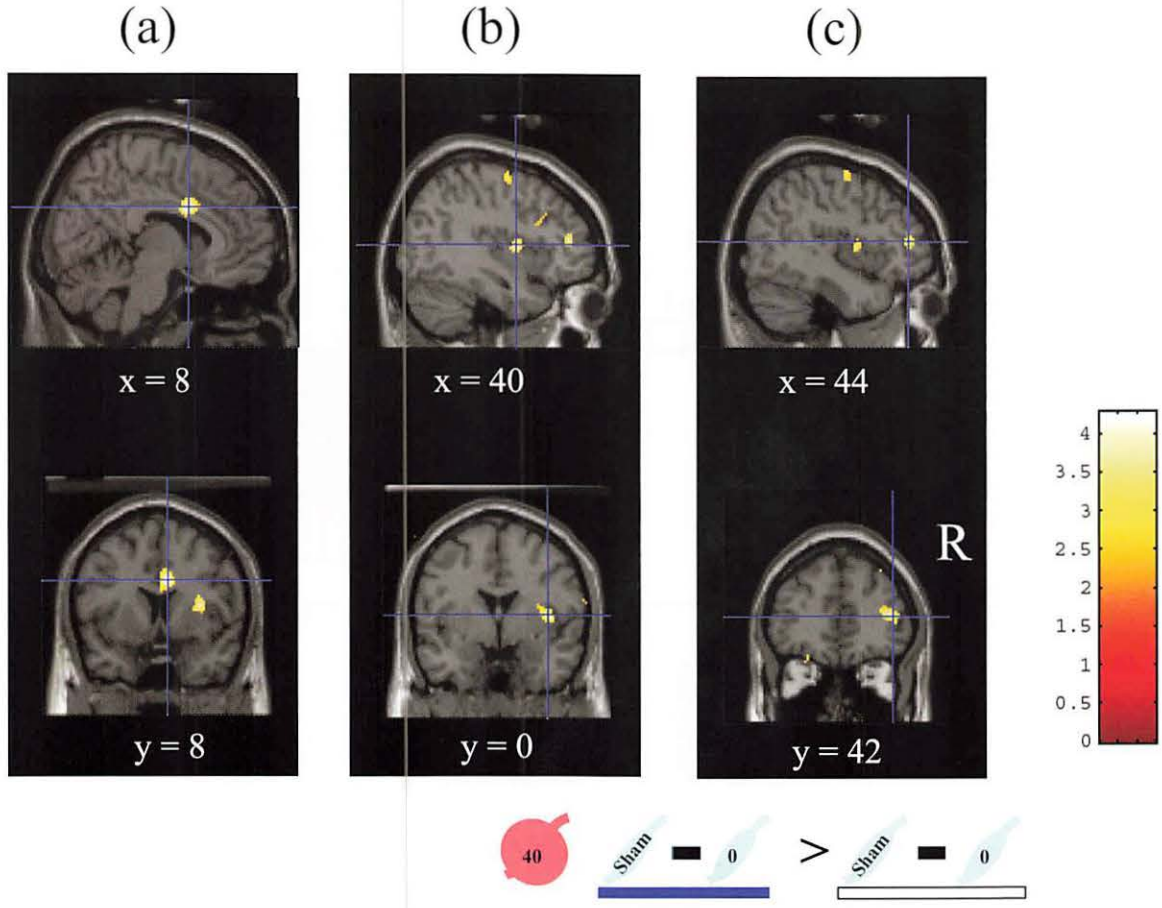

Fig. 2. Statistical (Z) maps of the rCBF during sham stimulation after 40 mmHg stimulation (group 4 and 5) compared with sham stimuli without prior stimuli (group 1 and 2). The maps overlaid on a sagittal (above) and verticofrontal (below) view of a single-subject MRI anatomical image, showing the location of significant higher rCBF. A conjunction analysis were made using 'multi-group, conditions and covariates' (uncorrected $p < 0.001$ for multiple comparisons, threshold of the voxel with alpha level $Z = 3.75$) SPM model[19]. Sham stimulation after the experience of 40 mmHg distention versus sham without the experience of colonic distention (minus baseline respectively). (a) Right cingulate gyrus, (b) right insula, (c) right middle frontal gyrus were found higher activation comparison of sham distention after the experience of 40 mmHg distention than no experienced sham stimuli.

VIII. 3. Does Colonic Motility Really become Conditioned in Humans? A PET Study Using Transcutaneus Electrical Nerve Stimulation (TENS).

Kanazawa M., Endo M.[*], *Yamaguchi K.*[**], *Hamaguchi T., William E. Whitehead.*[***], *Itoh M.*[**], *and Fukudo S.*

Departments of Behavioral Medicine, Tohoku University Graduate School of Medicine
[*]*Pharmacology, Tohoku University Graduate School of Medicine*
[**]*Cyclotron and Radioisotope Center, Tohoku University*
[***]*Center for Functional GI and Motility Disorders, the University of North Carolina at Chapel Hill*

INTRODUCTION

In classical or Pavlovian conditioning, the conditional stimulus (CS), which is a neutral stimulus paired with an uncomfortable unconditional stimulus (US) previously, comes to elicit behavioral and physiological responses as well as the US alone[1-3]. This learning process provides a model to understand anticipatory reports of pain and anticipatory gastrointestinal symptoms in situations that are not objectively threatening or painful[4]. However, little is known about the process of anticipatory response in gastrointestinal motility in humans.

Classical conditioning is considered to be a model to understand anticipatory responses to aversive events, which is an essential component of how the brain-gut interaction develops in functional gastrointestinal disorders. Previously, we have reported the following observations in humans[5]: (1) The colonic motility becomes conditioned with increasing smooth muscle tone and increasing number of phasic contractions; and (2) Characteristic brain areas become activated during anticipation regardless of the stimulus intensity. In this report, anticipatory responses in the brain and the colon in humans were reviewed.

METHODS

Subjects

Nine right-handed healthy male subjects (mean age 24 ± 1 years; 19 to 29 years)

were recruited from Tohoku University Campus in Sendai, Japan. All participants were free of gastrointestinal complaints and had not taken any medications within 4 weeks prior to testing. Each participant in this study underwent a medical history evaluation and was given a physical examination. Written informed consent was obtained from all participants, and this study was approved by the Tohoku University Ethics Committee.

Measurement of Rectosigmoid Function

The experiment was performed after a fasting period of at least 9 hours. The subjects were placed in supine position and were instructed not to move during each session because of positron emission tomography (PET) scanning at the same time. A computer-driven barostat (Synectics Visceral Stimulator; Synectics, Stockholm, Sweden) was used to assess the rectosigmoid function[6-8]. A polyethylene bag (diameter; 9 cm, length; 9 cm, volume; 0-500 ml), which was tightly fixed at both ends to a catheter, was inserted into the rectosigmoid colon of each subject and placed with distal end of the bag 10 cm from the anal verge 30 min before the study.

Measurement of Brain Activation

Using a similar technique which we have described in the previous report[9], regional cerebral blood flow (rCBF) was measured. Subjects were instructed to lie on their back in the positron emission tomography (PET) scanner and to minimize head movement and keep their eyes closed during the scanning (for 70 sec). Using a $^{68}Ge/^{68}Ga$ radiation source, transmission scans were carried out prior to PET scanning. ^{15}O-Labelled water (Tohoku University Cyclotron Radioisotope Center) was injected into the right arm vein 10 sec before the beginning of each stimulus session. Ten seconds later, the radioactivity in the brain reached a plateau and an increase in rCBF was detected by the PET scanning as an index of neural activity evoked by the stimulus. As shown in Figure 1, five scans of rCBF in each subject were measured using PET scanner in 3-dimensional sampling mode (HEADTOME V SET-2400W, Shimadzu, Kyoto, Japan)[10]. The scanner produced 63 horizontal slices with a separation of 3.125 mm, an axial field of view of 200 mm, an in-plane resolution of 590 mm, a full width at half maximum (FWHM), and an axial resolution of 3.9 mm FWHM. To ensure that radioactivity levels in each subject returned to baseline before starting a new scan, a 10-min interval was given between successive scans.

Protocol

There were 3 sessions; pre-conditioning, conditional and post-conditioning trials. Subjects were exposed 7 times to a loud buzzer (500 Hz with an intensity of 87dB) lasting 1 second and being followed by a 9 seconds break. This sequence served as the conditional stimulus (CS). For the first sequence, only the CS tones were administrated as a pre-conditioning trial.

The unconditional stimulus (US), which followed the conditional stimulus during the conditional trials and a part of the post-conditioning trials, was composed of transcutaneous electrical nerve stimulations (TENS; OG GIKEN AUDIO TREATER EF-501, Okayama, Japan) delivered to the back of the right hand at a frequency of 15 Hz with 2 different levels of intensity (7 or 4 mA). The US started just after each tone was finished and the stimulus period lasted 70 sec. After three sets of the conditional stimulus or the post-conditioning conditional stimulus sequence, high-mA TENS was applied as the unconditional stimulus. After the post-conditioning conditional stimulus sequence, low-mA TENS was applied as weak unconditional stimulus. After the pre- or post-conditioning CS-alone sequence, the unconditional stimulus was not applied. In the post-conditioning session, stimulus intensities of 0 (sham), 4 and 7 mA were given in random order.

PET scanning was performed at the resting period as a background, and the pre- and post-conditioning trials for each subject (5 injections/scans). Each combination of the stimulus (the conditional stimulus with/without the unconditional stimulus) with break (10-second duration) was repeated 7 times because the PET technique requires a 70-sec recording window for each scan. The intra-bag pressure of barostat was kept at 10 mmHg to measure changes in the bag volume in the rectosigmoid colon.

Analysis

The intrabag volume in the rectosigmoid colon was measured continuously and its variations were visually analyzed. Mean bag volume over each two-minute interval served as a measure of muscle tone, and number of phasic volume events (PVEs), served as a measure of phasic contractions. In the present study, 2-minute interval for the analysis of barostat measurement was selected not to fail to observe changes in the rapid volume waves[6]. To control for occasional, minor changes in colorectal tone, the volume had to differ more than 10 % from the baseline tone occurring at a frequency of 1-4 min^{-1} to be characterized as a change[6]. Movement artifacts were defined as sudden changes in bag volume that did not continue for more than 15 sec and/or did not differ more than 10 %

from baseline[6]; these artifacts were excluded from data analysis. Changes in the bag volume or number of phasic volume events from each two-minute baseline interval just before the stimulus (baseline interval) to each two-minute interval just after the beginning of the stimulus (stimulus interval), and each following two-minute interval (post-stimulus interval), were considered to represent the colorectal wall reactivity to the conditional stimulus with/without the unconditional stimulus. The paired Student t-test or Wilcoxon's rank-sum test was used for comparing the rectosigmoid function in the two-minute baseline, stimulus, and post-stimulus intervals of each trial. Alpha level was set at 5% for these statistical analyses.

PET data were transferred to a super computer (NEC SX-4/128H4, Tokyo, Japan) at the computer center of Tohoku University through the optical network. The image reconstruction of all brain area was carried out using the Three Dimensional Filtered Back Projection Algorithm[11]. The PET image data were analyzed using standard software (Statistical Parametric Mapping; SPM99, The Welcome Department of Cognitive Neurology, London) according to the method of Friston, et al[12]. All brain slices were analyzed. The PET images were realigned, spatially normalized, and transformed into an approximate Talairach-Tournoux stereotactic space, 3-D Gaussian filtered (FWHM; 13 mm), and proportionally scaled to account for global confounders. The size of each voxel was set at 2 x 2 x 2 mm. A t-test was used to compare rCBF differences between the pre- and post-conditioning CS-alone trials as a primal analysis for the effect of the conditioning. We set alpha equal to 0.1% (uncorrected for multiple comparisons) as the region of significant differences. The region which showed the significant activity correlations was identified on the basis of Talairach coordinates.

RESULTS

All the subjects reported pain to the right hand and different given stimulus intensities during the post-conditioning buzzer (the conditional stimulus; CS) with high- or low-mA stimulus (the unconditional stimulus; US) trials. They did not report any pain or discomfort to the right hand in the buzzer alone test trials. The buzzer with TENS or the buzzer alone did not induce any gastrointestinal symptoms.

Assessment of Rectosigmoid Function

The mean bag volume during two-minute baseline interval was not significantly

different among the sessions before and after the conditioning. In the post-conditioning CS + high-mA US trial, the mean bag volume during two-minute post-stimulus interval was significantly smaller than that during two-minute baseline interval (65 ± 29 ml vs 47 ± 18 ml, $p<0.05$). In the pre-conditioning trial and the post-conditioning CS-alone (baseline; 36± 11 ml vs post-stimulus; 34 ± 13 ml) and CS + low-mA US trials (48 ± 20 ml vs 38 ± 11 ml), the mean bag volume during post-stimulus intervals did not show significant difference compared to that during each baseline interval. Thus, no conditioned effect was demonstrated for rectosigmoid muscle tone.

In the post-conditioning CS-alone trial, the number of phasic volume events (PVEs) during the two-minute post-stimulus interval was significantly greater than that during the immediately preceding two-minute baseline interval (0 [0-2] /min vs 1 [0-2.5] /min, $p<0.05$). Also, the number of PVEs during the post-stimulus intervals were significantly greater than those during the baseline intervals in the post-conditioning CS + low-mA US (0.5 [0-1.5] /min vs 1 [0.5-2] /min, $p<0.05$) and CS + high-mA US (0 [0-1.5] /min vs 1 [0-2.5] /min, $p<0.05$) trials, respectively. There were no significant differences in the number of PVEs in the pre-conditioning trial (0 [0-1.5] /min vs 0.5 [0-1.5] /min). These data support a conditioning effect for colonic phasic contractions.

Assessment of Central Activation

The average PET data from all the subjects showed the conditioning elicited significant activation of the left lateral prefrontal, right anterior cingulate, bilateral parietal cortices, right insula, right pons and left cerebellum ($p\leq0.001$, uncorrected, Fig. 1) when comparing rCBF differences between pre- and post-conditioning CS-alone trials of PET images.

DISCUSSION

In the present study, the loud buzzer used prior to conditioning as a conditioned stimulus (CS) did not cause any alteration in rectosigmoid motility. However, following a series of conditional trials in which the buzzer was paired with painful electrical stimulation to the right hand, the buzzer alone elicited increases in the phasic contractions of the rectosigmoid colon, which were similar to those seen following the conditioned stimulus plus the unconditional stimulus. This provides evidence for Pavlovian conditioning of phasic motor responses. However, we did not find evidence for conditioning of the tonic

motor response (barostat volume) or subjective pain; following conditional trials, the CS-alone did not elicit changes in barostat volumes or reports of any gastrointestinal symptoms in the healthy subjects.

Considering the conditioning effect in the brain, our findings of the brain imaging (Fig. 1) were in accordance with previous studies showing cerebral activation in the frontal and parietal cortices following Pavlovian conditioning[13-15]. Activation of the prefrontal cortex was seen during somatic stimulus, and has been implicated in cognitive appraisal of the stimulus[16]. In addition, significant cortical activation in the anterior cingulate cortex (ACC) which is believed to play a role in mediating the affective qualities of the pain experience[17,18] and expectation of pain[19], and in the insula which serves as limbic integration cortex[20] was also seen as anticipatory responses in this study. Therefore, our results support that activation of the cognitive- and affective-related brain regions may contribute to the learned anticipatory responses and that this learned process was confirmed after the conditional trials in this experimental model. However, the direct relationships between the brain activation and the gastrointestinal response during anticipation have not been clarified with this model.

In summary, the Pavlovian conditioning study is significant because of positive findings that the conditioned phenomenon in this model is a first step to understand the anticipatory colonic motility responses. Significant increases in colonic phasic contractions and significant increases in cerebral blood flow in the cognitive- and affective-related cortical regions were observed in this study. This conditioning paradigm could be a model to investigate anticipatory responses in gastrointestinal motility and brain function which may contribute to development of functional gastrointestinal disorders. We concluded that the colonic motility can become conditioned by pairing a painful somatosensory stimulus with a neutral stimulus in humans.

References

1) Rescorla R.A.., Ann. Rev. Neurosci. **11** (1988) 329.
2) Bjorkstrand P.A.., Biol. Psychol. **30** (1990) 35.
3) Dadds M.R., Bovbjerg D.H., Redd W.H., Cutmore T.R.., Psychol. Bull. **122** (1997) 89.
4) Cameron O.G., Psychosom. Med. **63** (2001) 697.
5) Kanazawa M, Endo M, Yamaguchi K, Hamaguchi T, Whitehead WE, Itoh M, Fukudo S., Neurogastroenterol Motil, (in press).
6) Bell A.M., Pemberton J.H., Hanson R.B., Zinsmeister A.R.., Am. J. Physiol. **260** (1991) G17.
7) von der Ohe, Hanson R.B., Camilleri M., Neurogastroenterol. Mot. **6** (1994) 213.
8) Whitehead W.E., Delvaux M., Dig. Dis. Sci. **42** (1997) 223.
9) Hamaguchi T., Kano M., Rikimaru H., et al., Neurogastroenterol. Motil. **16** (2004) 299.
10) Fujiwara T., Watanuki S., Yamamoto S., et al., Ann. Nucl. Med. **11** (1997) 307.

11) Cherry S.R., Dahlbom M., Hoffman E.J., Phys. Med. Biol. **37** (1992) 779.
12) Friston K.J., Frith C.D., Liddle P.F., Frackowiak R.S., J. Cereb. Blood Flow Metab. **11** (1991) 690.
13) Fredrikson M., Wik G., Fischer H., Andersson J., Neuroreport **7** (1995) 97.
14) Hugdahl K., Berardi A., Thompson W.L., et al., Neuroreport **6** (1995) 1723.
15) Fischer H., Andersson J.L., Furmark T., Fredrikson M., Behav. Neurosci. **114** (2000) 671.
16) Derbyshire S.W., Jones A.K., Gyulai F., et al., Pain **73** (1997) 431.
17) Bantick S.J., Wise R.G., Ploghaus A., et al., Brain **125** (2002) 310.
18) Bernstein C.N., Frankenstein U.N., Rawsthorne P., et al., Am. J. Gastroenterol. **97** (2002) 319.
19) Sawamoto N., Honda M., Okada T., et al., J. Neurosci. **20** (2000) 7438.
20) Augustine J.R.., Brain Res. Rev. **22** (1996) 229.

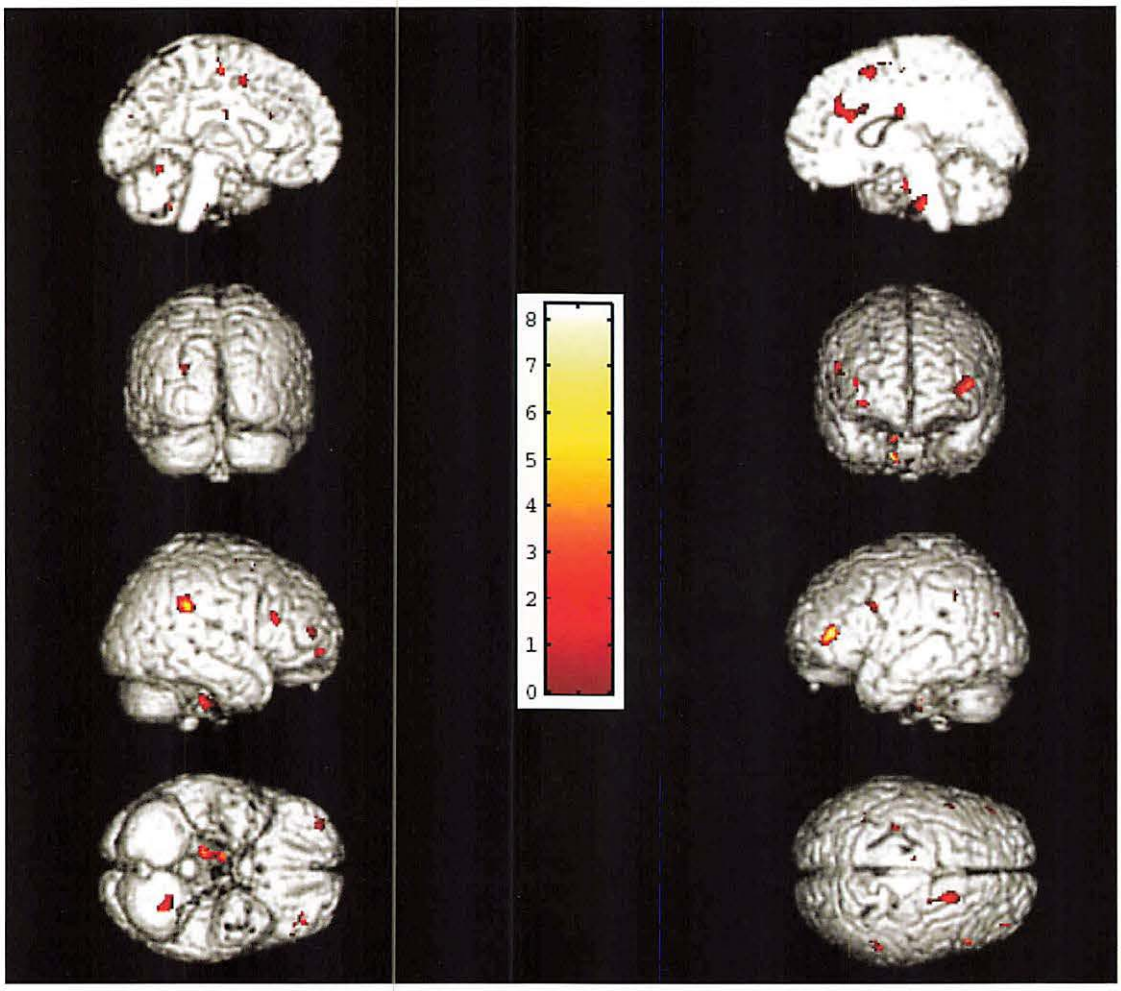

Figure 1. Conditioning effects on regional cerebral blood flow.

VIII. 4. Neural Correlates of Deception

Abe N.[*], *Suzuki M.*[*,**], *Tsukiura T.*[***], *Mori E.*[*], *Yamaguchi K.*[**], *Itoh M.*[**], *and Fujii T.*[*]

[*]*Department of Behavioral Neurology and Cognitive Neuroscience, Tohoku University Graduate School of Medicine*
[**]*Division of Cyclotron Nuclear Medicine, Cyclotron and Radioisotope Center, Tohoku University*
[***]*Cognitive and Behavioral Sciences Group, Neuroscience Research Institute, National Institute of Advanced Industrial Science and Technology (AIST)*

So far, several neuroimaging studies using functional magnetic resonance imaging (fMRI) on deception have reported the involvement of the prefrontal cortex (PFC)[1-6], which has an indispensable role for executive function. Activation of the anterior cingulate cortex (ACC), which has been regarded as a substantial area for conflict monitoring, has also often been reported[4-6]. Although these previous studies indicate crucial roles of the PFC and ACC in human deception, the specific role of each region during deception is still unclear.

In the present PET study, we examined brain activity focusing on two types of deception for past episodes: deception for experienced events (pretending not to know) and deception for un-experienced events (pretending to know). During two deception conditions and two truth conditions, subjects were presented with old photographs related to experienced events in one and new photographs related to un-experienced events in the other. We expected the PFC to be active during the two deception conditions compared to the two truth conditions, because the former necessitate executive functions. In contrast, we anticipated that the ACC would be active only during the deception condition in which subjects were asked to tell lies in response to the old photographs (pretending not to know). The old photographs, compared with the new ones, would elicit stronger conflict for the inhibition of true answers during deception because the memory of experienced events would be vividly recovered by recognition of the old photographs, but not by the new photographs.

Before PET scanning, subjects experienced 20 real-world events. During PET,

they were presented with either old photographs related to experienced events or new photographs related to un-experienced events and were instructed to tell either truths or lies orally in four conditions: (1) a Truth-Old (TO) task, in which they were instructed to tell truths about experienced events, (2) a Lie-Old (LO) task, in which they had to tell lies about experienced events, (3) a Truth-New (TN) task, in which they had to tell truths about un-experienced events, and (4) a Lie-New (LN) task, in which they had to tell lies about un-experienced events.

To identify the neural correlates of deception, the functional imaging data were first analyzed for the main effect of deception [(LO–TO) + (LN–TN)]. This analysis revealed significant activations in the left middle frontal gyrus (BA 10/46; the most anterior part of the dorsolateral PFC), right inferior frontal gyrus (BA 45; ventrolateral PFC), right ACC (BA 24/32), and right medial prefrontal cortex (BA 9; medial PFC). Table 1 summarizes these data for anatomical structures and Brodmann's area, MNI coordinates, Z-values, and cluster size of peak activations. Second, to examine the influence of the familiarity of stimuli on regional cerebral blood flows (rCBFs) in each activated region and whether or not an interaction occurred, the rCBF values measured at each maximum were analyzed using two-way ANOVA with the response to stimuli (Truth, Lie) and the familiarity of stimuli (Old, New) as factors. The results are illustrated in Fig. 1. Results of the ANOVA for the left dorsolateral PFC showed a significant main effect of the "Lie" [$F(1, 13) = 23.470$, $p < 0.001$], but showed neither a main effect of the familiarity of stimuli [$F(1, 13) = 0.172$, $p = 0.685$, ns] nor an interaction between the two factors [$F(1, 13) = 0.173$, $p = 0.684$, ns]. ANOVA for the right ventrolateral PFC yielded similar results: a significant main effect of the "Lie" [$F(1, 13) = 24.857$, $p < 0.001$], without a main effect of the familiarity of stimuli [$F(1, 13) = 1.879$, $p = 0.194$, ns] or an interaction [$F(1, 13) = 1.087$, $p = 0.316$, ns]. Results for the right ACC showed a significant main effect of the "Lie" [$F(1, 13) = 20.895$, $p < 0.001$], without a main effect of the familiarity of stimuli [$F(1, 13) = 1.301$, $p = 0.275$, ns]. In this region, interaction between the two factors was significant [$F(1, 13) = 14.828$, $p < 0.005$]. Post-hoc test (Scheffe) revealed that in the right ACC the effect of "Lie" was significant between the LO tasks and TO tasks (LO > TO, $p < 0.001$), but was not significant between the LN tasks and TN tasks ($p = 0.756$, ns), and the effect of "Old" was significant between the LO tasks and LN tasks (LO > LN, $p < 0.05$), but not between the TO tasks and TN tasks ($p = 0.631$, ns). Results for the right medial PFC showed a significant main effect of "Lie" [$F(1, 13) = 16.336$, $p < 0.005$] and a main effect of "Old" [$F(1, 13) = 18.692$, $p < 0.001$], without an interaction [$F(1, 13) = 0.404$, $p = 0.536$,

ns].

Our results demonstrate the possibility of dissociable roles of the prefrontal and anterior cingulate cortices in human deception. The prefrontal cortices, including the dorsolateral PFC, ventrolateral PFC, and medial PFC, were associated with giving deceptive responses regardless of the familiarity of the stimuli, although the precise role of each prefrontal cortex needs to be clarified in future studies. The ACC was associated only with giving deceptive responses to old (experienced) stimuli. When individuals have to give deceptive responses to experienced events, the ACC probably detects strong cognitive conflict and may have a specific role in the inhibition of memories about experienced events.

There are limitations of the present study that should be borne in mind for future studies into the brain mechanisms underlying deception. Although we employed real-world event tasks, simulated deception in laboratory experiments cannot be viewed as being the same as deception in real life. In particular, tasks dealing with deception are often not emotional enough to allow one to investigate the effect of emotion during deception. A further refined experimental design is needed to deal with this problem and to enable us to understand the complex biological mechanisms of human social interactions.

References

1) Spence SA., Farrow TF., Herford AE., Wilkinson ID., Zheng Y., Woodruff PW. Neuroreport **12** (2001) 2849.
2) Langleben DD., Schroeder L., Maldjian JA., Gur RC., McDonald S., Ragland JD., O'Brien CP., Childress AR. Neuroimage **15** (2002) 727.
3) Lee TMC., Liu HL., Tan LH., Chan CCH., Mahankali S., Feng CM., Hou J., Fox PT., Gao JH. Hum Brain Mapp **15** (2002) 157.
4) Ganis G., Kosslyn SM., Stose S., Thompson WL., Yurgelun-Todd DA. Cereb Cortex 13 (2003) 830.
5) Kozel FA., Padgett TM., George MS. Behav Neurosci **118** (2004) 852.
6) Kozel FA., Revell LJ., Lorberbaum JP., Shastri A., Elhai JD., Horner MD., Smith A., Nahas Z., Bohning DE., George MS. J Neuropsychiatry Clin Neurosci **16** (2004) 295.

Table 1. Brain regions showing activation in a main effect of deception.

Region (Brodmann's Area)	MNI coordinates			Z value	Cluster size
	x	y	z		
Lt middle frontal gyrus (10/46)	-26	54	14	4.39	51
Rt inferior frontal gyrus (45)	52	18	12	4.07	22
Rt anterior cingulate cortex (24/32)	10	16	32	4.16	34
Rt medial prefrontal cortex (9)	10	56	24	4.04	26

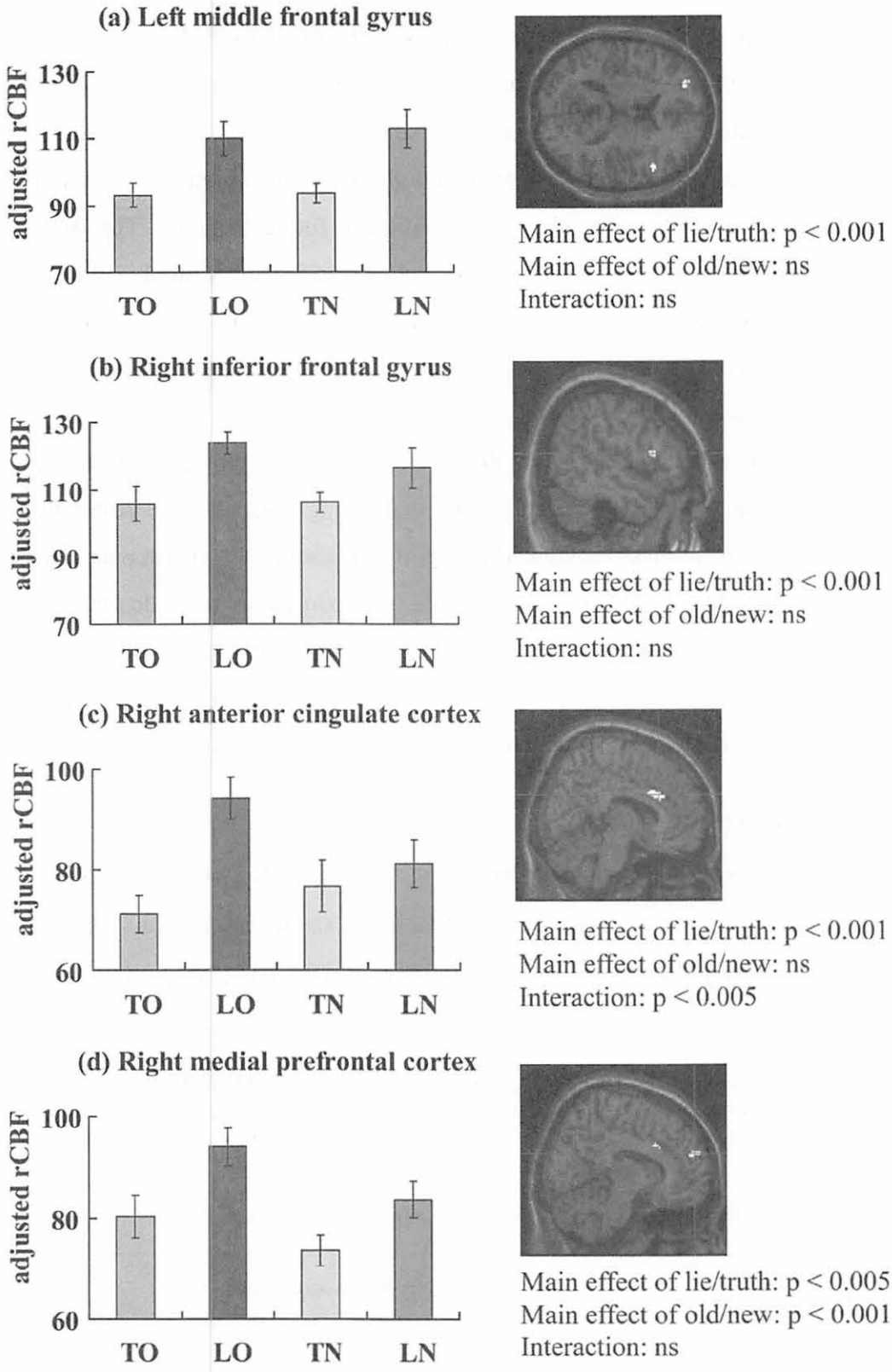

Fig. 1. Four regions showing a significant main effect of deception. The activations are superimposed onto MRIs of Montreal Neurological Institute (MNI) templates.

IX. RADIATION PROTECTION AND TRAINING OF SAFETY HANDLING

IX. 1. Beginners Training for Safe Handling of Radiation and Radioisotopes in Tohoku University

Baba M., Miyata T., Iwata R., and Nakamura T.

Cyclotron and Radioisotope Center, Tohoku University

During 2004, the beginners training for safe handling of radiation and radioisotopes in Tohoku University was conducted in three courses as usual;
1) Radiation and Isotopes, 2) X-ray Machines and Electron Microscope, and 3) Synchrotron Radiation (SOR). The training was held twice a year, May and November, under the help for lectures and practice from various departments and research institutes of the university.

Lectures in English which were started in November of 2002 were continued for students and/or researchers who are not so familiar with Japanese language, by using PC projector and text of copies of view graphs (English class). The number of English class is steady.

The training for "Radiation and Radioisotopes" is for persons who use unshielded radioisotopes and accelerators, and has been conducted from 1977. The contents of lectures and practices are shown in Table 1. In the fiscal year of 2004, the training was performed for 623 persons (27 persons in the English class). The departments or institutes to which they belong are given in Table 2.

The training for "X-ray machines and electron microscopes" started at the end of 1983. The training is scheduled twice a year at the same time as that for "Radiation and Radioisotopes". In this course, only lectures are given with no practice. The contents of the lectures and the distributions of trainees are shown in Table 3 and Table 4, respectively. The number of trainees was 411 (30 in the English class).

The training for the "Synchrotron Radiation" began at the end of 1995. The contents of the lectures are the same as those of the radiation and radioisotopes but no practice. In 2004, the number of trainees of the SOR course was 89 (2 in the English class).

Table 1. Contents of the lectures and practices for safe handling of radiation and radioisotopes in 2004.

Lectures (one day)	Hours
Radiation physics and measurements	1.5
Chemistry of radioisotopes	1.0
Effects of radiation on human	1.5
Radiological protection ordinance	1.0
Safe handling of radioisotopes	1.5

Practices (one day)	Hours
Treatment of unsealed radioactive solution	4.0
Measurement of surface contamination and decontamination	1.0
Measurement of gamma-rays and beta-rays	2.0

Table 2. Distribution of trainees for "radiation and radioisotopes" in 2004.

Department	Staff	Student	Total	English class
Medicine	21	83	104	6
Dentistry	1	19	20	0
Pharmacy	2	87	89	5
Science	7	67	74	3
Engineering	4	98	102	0
Agriculture	0	71	71	0
Research Institutes	12	69	81	10
The others	10	54	55	3
Total	48	548	597	27

Table 3. Contents of the lectures for "X-ray machines and electron microscopes" in 2004.
(same for both Japanese and English class)

Lectures (one day)	Hours
Safe handling of X-ray machines	1.5
Radiological protection ordinance	0.5
VTR for safe handling of radiation and radioisotopes	0.5

Table 4. Distribution of trainees for "X-ray machines and electron microscopes" in 2004.

Department	Staff	Student	Total	English class
Medicine	4	1	5	
Dentistry	1	0	1	
Science	3	30	33	4
Engineering	16	165	181	13
Research Institutes	40	86	126	10
The others	3	32	35	3
Total	67	314	381	30

Table 5. Distribution of trainees for "synchrotron radiation" in 2004.

Department	Staff	Student	Total	English Class
Medicine	2	0	2	
Dentistry	1	4	5	
Pharmacy	1	0	1	
Science	2	11	13	
Engineering	0	28	28	1
Research Institutes	6	32	38	1
Total	12	75	87	2

IX. 2. Radiation Protection and Management

*Miyata T., Baba M. and Watanabe N.**

Cyclotron and Radioisotope Center, Tohoku University
**Japan Radiation Protection Co., Ltd.*

(1) Overview

During the fiscal year of 2004, research and education in the center were conducted as active as usual.

New ^{7}Li(p,n) neutron source was installed at the 3-2 course of CYRIC. This source was designed to achieve a highest level neutron flux over the world by enabling short distance between target and sample or detector. The inspection of the facility for radiation licensing was done at the end of August and approval was provided by the Monbu-kagakusho. Now the source is served to experiments using mono-energy neutrons and semiconductor test experiments.

The new online radiation protection and management system of CYRIC which was installed in 2002 worked fairly reliably except for some problems slowing down of the system response when the data transfer rate is so high. The radiation detectors connected with the monitoring system performed reliably too while one gamma detector should be repaired.

Along with the change of organization of the university, measurement of radioactivity concentration is continued periodically but the observed level was low enough generally. Devices and gas counters with automatic sample changer for radioactivity concentration measurement (samplers, α-β automatic counters) were routinely used without serious problems by several radiation facilities in Tohoku University.

(2) Unsealed radio nuclides used in CYRIC

The species and amounts of unsealed radio nuclides handled in CYRIC during the fiscal year of 2003 are summarized in Table 1. The table includes the isotopes produced by the cyclotron as well as those purchased from the Japan Radio Isotope Association or

taken over from other radioisotope institutes.

(3) Radiation exposure dose of individual worker

The exposure doses of the workers in CYRIC during 2004 are given in Table 2. The doses were sufficiently lower than the legal dose limits.

(4) Radiation monitoring of the workplace

Radiation dose rates inside and outside of the controlled areas in CYRIC were monitored periodically and occasionally when needed. They were generally below the legal dose limits although there are several "hot spots" in mSv/hr range like slits or beam stopper and d so on. Surface contamination levels of the floors inside the controlled areas were also measured with a smear method and a survey meter method. They were under the legal regulation levels.

(5) Wastes management

The radioactive wastes were delivered to the Japan Radio Isotope Association twice in the fiscal year of 2004.

The concentration of radioisotopes in the air released from the stack after filtration was monitored with stack gas monitors. The values on concentration were lower than the legal regulation levels. The radioactive water was stocked in the tanks at least for 3 days and then released to the sewerage after confirming that the concentration was lower than the legal regulation levels.

Radioactive organic scintillator waste of 800 litter was treated by incinerator provided by Fuji-kogyo Co.Ltd. The incinerator was overhauled last year.

Table 1. Unsealed radioisotopes used in each building of CYRIC during 2004.

(a) Cyclotron Building (kBq)

Group1,2		Group3		Group4	
^{42}Ar	6.000	^{11}C	1,083,866,900.000	^{18}F	813,706,180.000
				^{7}Be	987.070
Total	6.000	Total	1,083,866,900.000	Total	813,706,180.000

(b) Radio-isotope Building (kBq)

Group1,2		Group3		Group4	
^{90}Sr	60.000	^{11}C	1,191,400.000	^{14}C	36,553.480
^{57}Co	1,853.180	^{99}Mo	2,915,500.000	^{51}Cr	11,243,300
^{60}Co	541.740	^{32}P	945,777.600	^{18}F	12,471,590.000
^{137}Cs	5,786.000			^{3}H	265,111.530
^{68}Ge	133,858.000				
^{125}I	47,165.908				
Total	189,205.138	Total	5,052,677.600	Total	12,784,498.310

* Including the use in the "β -ray analysis" room

(c) Research Building (kBq)

Group1,2		Group3		Group4	
		^{15}O	11,285,000.000	^{18}F	5,069,000.000
Total	0	Total	11,285,000.000	Total	5,069,000.000

Table 2. Occupational radiation exposures at CYRIC during the fiscal year of 2004.

Dose range (mSv)	Number of individuals
No measurable exposure	38
Less than 1.0	13
1.0 to 2.0	2
2.0 to 3.2	2
Total number of persons monitored	55

X. PUBLICATIONS

X. PUBLICATIONS

(January 2003 ~December 2004)

[597] Specific brain processing of emotion by facial expressions in people with alexithymia: an $H_2{}^{15}O$-PET study.
M. Kano, S. Fukudo, J. Gyoba, K. Miyuki, M. Tagawa, H. Mochizuki, M. Itoh, M. Hongo, K. Yanai.
Brain, 126 (2003) 1474-1484.

[598] Imaging of central itch modulation in the human brain using positron emission tomography.
H. Mochizuki, M. Tashiro, M. Kano, Y. Sakurada, M. Itoh, K. Yanai.
Pain, **105** (2003) 339-46.

[599] Quantitative measurement of histamine H_1 receptors in human brains by PET and [^{11}C]doxepin.
H. Mochizuki, Y. Kimura, K. Ishii, K. Oda, T. Sasaki, M. Tashiro, K. Yanai, K. Ishiwata.
Nucl Med Biol., 31 (2004) 165-171.

[600] Evaluation of *O*-[^{11}C]metyl-L-tyrosine and *O*-[^{18}F]fluoromethyl-L-tyrosine as tumor imaging tracers by PET.
Kiichi Ishiwata, Kazunori Kawamura, Wei-Fang Wang, Shozo Furumoto, Kazuo Kubota, Claudio Pascali, Anna Bogni, Ren Iwata.
Nucl. Med. Biol., **31** (2004) 191-198.

[601] Evaluation of in vivo selective binding of [^{11}C]doxepin to histamine H_1 receptors in five animal species.
Kiichi Ishiwata, Kazunori Kawamura, Wei-Fang Wang, Hideo Tsukada, Norihiro Harada, Hideki Mochizuki, Yuichi Kimura, Kenji Ishii, Ren Iwata, Kazuhiko Yanai.
Nucl. Med. Biol., **31** (2004) 493-502.

[602] Simplified PET measurement for evaluating histamine H_1 receptors in human brains using [^{11}C]doxepin.
H. Mochizuki, Y. Kimura, K. Ishii, K. Oda, T. Sasaki, M. Tashiro, K. Yanai, K. Ishiwata.
Nucl. Med. Biol., **31** (2004) 1005-1011.

[603] Aspiration pneumonia and insular hypoperfusion in patients with cerebrovascular disease.
N. Okamura, M. Maruyama, T. Ebihara, T. Matsui, M. Nemoto, H. Arai, H. Sasaki, K. Yanai.
J. Am. Geriatr. Soc., **52** (2004) 645-646

[604] Central effects of fexofenadine and cetirizine: Measurement of psychomotor performance, subjective sleepiness and brain histamine H_1-receptor occupancy using [^{11}C]doxepin PET.
M. Tashiro, Y. Sakurada, K. Iwabuchi, H. Mochizuki, M. Kato, M. Aoki, Y. Funaki, M. Itoh, R. Iwata, D.F. Wong, K. Yanai.
J. Clin. Pharmacol., **44** (2004) 890-900.

[605] Decreased histamine H_1 receptor binding in the brain of depressed patients.
M. Kano, S. Fukudo, A. Tashiro, A. Utsumi, D. Tamaru, M. Itoh, R. Iwata, M. Tashiro, H. Mochizuki, Y. Funaki, M. Kato, M. Hongo, K. Yanai.
Eur. J. Neurosci., **20** (2004) 803-810.

[606] Neural correlates of context memory with real-world events.
Toshikatsu Fujii, Maki Suzuki, Jiro Okuda, Hiroya Ohtake, Kazuyo Tanji, Keiichiro Yamaguchi, Masatoshi Itoh, and Atsushi Yamadori.
NeuroImage, **21** (2004) 1596-1603.

[607] Polarization transfer and spin response functions of the ^{2}H($\vec{p},\vec{n}$) reaction at 345 MeV.
T. Wakasa, H. Sakai, M. Ichimura, K. Hatanaka, M. B. Greenfield, M. Hatano, J. Kamiya, H. Kato, Y. Maeda, H. Okamura, T. Ohnishi, H. Otsu, K. Sekiguchi, K. Suda, A. Tamii, T. Uesaka, T. Yagita, and K. Yako.
Phys. Rev., C **69** (2004) 044602-1-7.

[608] Total Spin Transfer in Continuum for ^{90}Zr(p,n) Reaction at 295MeV.
Tomotsugu Watasa, Hideyuki Sakai, Hiroyuki Okamura, Hideaki OTsu, Takamasa Nonaka, Tetsuya Ohnishi, Kentaro Yako, Kimiko Sekigucgi, Satoshi Fujita, Tomohiro Uesaka, Yoshiteru Satou, Satoru Ishida, Naruhiko Sakamoto, Mark B. Greenfield, Kichiji Hatanaka.
J. Phys. Soc. Japan, **73** (2004) 1611-1614.

[609] Polarization transfer measurement for ^{1}H($\vec{d},\vec{p}$)^{2}H elastic scattering at 135 MeV/nucleon and three-nucleon force effects.
K. Sekiguchi, H. Sakai, H. Witala, K. Ermisch, W. Glöckle, J. Golak, M. Hatano, H. Kamada, N. Kalantar-Nayestanaki, H. Kato, Y. Maeda, J. Nishikawa, A. Nogga, T. Ohnishi, H. Okamura, T. Saito, N. Sakamoto, S. Sakoda, Y. Satou, K. Suda, A. Tamii, T. Uchigashima, T. Uesaka, T. Wakasa, K. Yako.
Phys. Rev., C **70** (2004) 014001-1-17.

[610] Pionic enhancement in quasielastic ($\vec{p},\vec{n}$) reactions at 345 MeV.
T. Wakasa, H. Sakai, M. Ichimura, K. Hatanaka, M. B. Greenfield, M. Hatano, J. Kamiya, H. Kato, K. Kawahigashi, Y. Maeda, Y. Nakaoka, H. Okamura, T, Ohnishi, H. Otsu, K. Sekiguchi, K. Suda, A. Tamii, T. Uesaka, T. Yagita, K. Yako.
Phys. Rev., C **69** (2004) 054609-1-10.

[611] The Role of σ-Receptors in Levodopa- Induced Dyskinesia in Patients With Advanced Parkinson Disease: A Position Emission Tomography Study.
Taro Nimura, Tadashi Ando, Keiichiro Yamaguchi, Takeshi Nakajima, Reizo Shirane, Masatoshi Itoh, Teiji Tominaga.
J. Neurosurg., **100** (2004) 606-610.

[612] Brain activity during distention of the descending colon in humans.
T. Hamaguchi, M. Kano, H. Rikimaru, M. Kanazawa, M. Itoh, K. Yanai, S. Fukudo.
Neurogastroenterol Motil, **16**,(2004)2 99-309.

[613] Mapping of Heavy Metals Accumulated in Plants Using Submilli-PIXE Camera.
R. Watanabe, J. Hara, C. Inoue, T. Chida, Ts. Amartaivan, S. Matsuyama, H. Yamazaki, K. Ishii.
Int. J. PIXE, **14** (2004) 35-41.

[614] Beam Damage of Cellular Samples in In-Air Micro PIXE Analysis.
H. Komori, K. Mizuma, K. Ishii, H. Yamazaki, S. Matsuyama, Ts. Amartaivan, Y. Ohishi, M. Rodriguez, T. Yamaguchi, A.S uzuki.
Int. J. PIXE, 14 (2004) 75-81.

[615] Mothod for Determining the Localization of Trace Elements Observed by the Micro PIXE Camera.
S. Harada, K. Ishii, A. Tanaka, T. Satoh, S. Matsuyama, H. Yamazaki, T. Kamiya, T. Sakai, K. Arakawa, S. Oikawa, K. Sera.
Int. J. PIXE, **14** (2004) 83-88.

[616] Microbeam Analysis System at Tohoku University.
S. Matusyama, K. Ishii, H. Yamazaki, Y. Barbotteau, Ts. Amartaivan, D. Izukawa, H. Hotta, K. Mizuma, S. Abe, Y. Ohishi, M. Rodriguez, A. Suzuki, R. Sakamoto, M. Fujisawa, T. Kamiya, M. Oikawa, K. Arakawa, H. Imazaki, N. Matsumoto.
Int. J. PIXE, **14** (2004) 1-8.

[617] Behavior of Pet Foil Used as Beam Extraction Window During Irradiation at Atmospheric Pressure.
Y. Barbotteau, K. Ishii, K. Mizuma, H. Yamazaki, S. Matsuyama, T. Sakai, T. Satoh, T. Kamiya . International
Int. J. PIXE, **14** (2004) 19-26.

[618] The Elemental Analysis of IgE-Sensitized RBL-2H3 Cells Using In-Air Micro PIXE.
K. Mizuma, K. Ishii, Y. Barbotteau, S. Abe, H. Yamazaki, S. Matsuyama, E. Sakurai, K. Yanai, T. Kamiya, T. Sakai, T. Satoh, M. Oikawa, K. Arakawa.
Int. J. PIXE, **14** (2004) 27-34.

[619] Enhanced Electron-capture Decay Rate of ^{7}Be Encapsulated in C_{60} Cages.
T. Ohtsuki, H. Yuki, M. Muto, J. Kasagi, K. Ohno.
Phys. Rev. Lett., **93** (2004) 112501-1-4.

[620] PIXE Analysis of Water Leakage from a Landfill Site of Industrial Waste-Generationg Hydrogen Sulfide.
H. Yamazaki, K. Ishii, S. Matsuyama, Ts. Amartaivan, A. Suzuki, T. Yamaguchi, G. Momose, K. Hotta, K. Mizuma, T. Izukawa, S. Abe, T. Sasaki.
Int. J. PIXE, **14** (2004) 57-66.

[621] FDG PET and Gallium Scintigraphy for Diagnosis of An Advanced Jejunal Adenocarcinoma With Distant Metastases.
Gengo Yamaura, Takashi Yoshioka, Kazuo Kubota, Keiichirou Yamaguchi, Ren Iwata, Tadayoshi Abe, Yasushi Kitagawa, Ryunosuke Kanamaru, Hiroshi Fukuda, Chikashi Ishioka.
Clin. Nucl. Med., **29** (2004) 825-827.

[622] New radiopharmaceuticals for cancer imaging and biological characterization using PET.
Hiroshi Fukuda, Shozo Furumoto, Ren Iwata, Kazuo Kubota.
Int. Congress Ser., **1264** (2004) 158-165.

[623] Experimental studies on the neutron emission spectrum and activation cross-section for 40 MeV deuterons in IFMIF accelerator structural elements.

M. Hagiwara, T. Itoga, M. Baba, M.S. Uddin, N. Hirabayashi, T. Oishi, T. Yamauchi.
J. Nucl. Materials, **329-333** (2004) 218-222

[624] Effect of He pre-implantation and neutron irradiation on mechanical properties of SiC/SiC composite.
S. Nogami, A. Hasegawa, L.L. Snead, R.H. Jones, K. Abe.
J. Nucl. Materials, **329-333** (2004) 577-581.

[625] Measurement of the tensor analyzing power T_{20} in the *dd* → ^{3}He*n* and dd → ^{3}H*p* at intermediate energies and at zero degree.
V.P. Ladygin, T. Uesaka, T. Saito, M. Hatano, A.Yu. Isupov, H. Kato, N.B. Ladygina, Y. Maeda, A.I.Malakhov, J. Nishikawa, T. Ohnishi, H. Okamura, S.G. Reznikov, H. Sakai, N. Sakamoto, S. Sakoda, Y. Satou, K. Sekiguchi, K. Suda, A. Tamii, N. Uchigashima, K. Yako.
Phys. Lett., **B 598** (2004) 47-54.

[626] Impacts of neuroimaging on psycho-oncology.
M.Tashiro.
Psychooncology, **13** (2004) 486-489.

[627] Measurement of Differential Thick Target Neutron Yields and ^{7}Be production in the Li, ^{9}Be(d,n) Reactions for 25 MeV Deuterons.
T. Aoki, M. Hagiwara, M. Baba, M. Sugimoto, T. Miura, N. Kawata, A. Yamadera.
J. Nucl. Sci. Tech., **41** (2004) 399–405.

[628] Measurement of neutron activation cross sections for major elements of water, air and soil between 30 and 70 MeV.
H. Yashima, K. Terunuma, T. Nakamura, M. Hagiwara, N. Kawata, M. Baba.
J. Nucl. Sci. Tech., **Suppl.–4** (2004) 70-73.

[629] Measurement of excitation function of the proton-induced activation reactions on tantalum in the energy range 28–67MeV.
M.S. Uddin, M. Hagiwara, N. Kawata, T. Itoga, N. Hirabayashi, M. Baba, F. Tarkanyi, F. Ditroi, d.J. Csikai.
J. Nucl. Sci. Tech., **Suppl.–4** (2004) 160-163.

[630] Application of Imaging Plate to Measurement of Radiation Spatial Distribution.
M. Hagiwara, A. Yamadera, N. Hirabayashi, T. Aoki, M. Baba, Y.S.Lee.
J. Nucl. Sci. Tech., **Suppl.–4** (2004) 267-271.

[631] Development of thermal neutron profiling method using an optical fiber.
T. Itoga, N. Kawata, M. Hagiwara, N. Hirabayashi, M. Baba, T.Nishitani, K. Ochiai.
J. Nucl. Sci. Tech., **Suppl.–4** (2004) 403-406.

[632] Development of a New Multi-Moderator Spectrometer for Epithermal Neutron.
S. Yonai, T. Itoga, T. Nakamura, M. Baba.
J. Nucl. Sci. Tech., **Suppl.–4** (2004) 415-417.

[633] Experimental studies on the proton-induced activation reactions of molybdenum in the energy range 22–67MeV.
M.S. Uddin, M. Hagiwara, F. Tarkanyi, F. Ditroi, M. Baba.

Appl. Radiat. Isot., **60** (2004) 911–920.

[634] Benchmark Experiment for Cyclotron-Based Neutron Source for BNCT.
S. Yonai, T. Itoga, M. Baba, T. Nakamura, H. Yokohori, Y. Tahara.
Appl. Radiat. Isot., **61** (2004) 997-1001.

[635] Measurement of Differential Thick Target Neutron Yields of C, Al, Ta, W(*p,xn*) Reactions for 50-MeV Protons.
T. Aoki, M. Baba, S. Yonai, N. Kawata, M. Hagiwara, T. Miura, T. Nakamura.
Nucl. Sci. Eng., **146** (2004) 200.

XI. MEMBERS OF COMMITTEE

XI. MEMBERS OF COMMITTEE (as of Jan. 1, 2005)

General

(Chairman)	Keizo	Ishii	(Graduate School of Engineering)
	Katsuto	Nakatsuka	(Vise President)
	Osamu	Hashimoto	(Graduate School of Science)
	Hiroshi	Kudo	(Graduate School of Science)
	Akira	Takahashi	(Graduate School of Medicine)
	Keiichi	Sasaki	(Graduate School of Dentistry)
	Yasushi	Ohizumi	(Faculty of Pharmaceutical Sciences)
	Katsunori	Abe	(Graduate School of Engineering)
	Ryoichi	Katsumata	(Graduate School of Agricultural Science)
	Kazuhiko	Nishitani	(Graduate School of Life Science)
	Isamu	Sato	(Institute for Materials Research)
	Hiroshi	Fukuda	(Institute for Development, Aging and Cancer)
	Tanetoshi	Koyama	(Institute of Multidisciplinary Research for advanced Materials)
	Syoki	Takahashi	(University Hospital)
	Jirohta	Kasagi	(Laboratory of Nuclear Science)
	Tatsuo	Ido	(CYRIC)
	Masatoshi	Itoh	(CYRIC)
	Mamoru	Baba	(CYRIC)
	Ren	Iwata	(CYRIC)
	Hiroyuki	Okamura	(CYRIC)
	Tsutomu	Shinozuka	(CYRIC)
	Toshio	Kobayashi	(Graduate School of Science)
	Kazuhiko	Yanai	(Graduate School of Medicine)
	Tetsuya	Ono	(Radiation Safety Committee, Research Promotion Council)

	Ryuko	Yoshida	(Head of Administration Office, Graduate School of Information Science: Observer)

Research Program

(Chairman)	Mamoru	Baba	(CYRIC)
	Tatsuo	Ido	(CYRIC)
	Masatoshi	Itoh	(CYRIC)
	Ren	Iwata	(CYRIC)
	Hiroyuki	Okamura	(CYRIC)
	Tsutomu	Shinozuka	(CYRIC)
	Osamu	Hashimoto	(Graduate School of Science)
	Tsutomu	Sekine	(Graduate School of Science)
	Kazuhiko	Yanai	(Graduate School of Medicine)
	Akira	Takahashi	(Graduate School of Medicine)
	Katsunori	Abe	(Graduate School of Engineering)
	Hiromichi	Yamazaki	(Graduate School of Engineering)
	Isamu	Sato	(Institute for Materials Research)
	Hiroshi	Fukuda	(Institute for Development, Aging and Cancer)
	Syoki	Takahashi	(University Hospital)
	Jirohta	Kasagi	(Laboratory of Nuclear Science)

Cyclotron

(Chairman)	Osamu	Hashimoto	(Graduate School of Science)
	Toshio	Kobayashi	(Graduate School of Science)
	Naoki	Toyota	(Graduate School of Science)
	Tsutomu	Sekine	(Graduate School of Science)
	Kazushige	Maeda	(Graduate School of Science)
	Hirokazu	Tamura	(Graduate School of Science)
	Keizo	Ishii	(Graduate School of Engineering)
	Akira	Hasegawa	(Graduate School of Engineering)
	Isamu	Sato	(Institute for Materials Research)

	Masao	Saitoh	(Institute of Multidisciplinary Research for advanced Materials)
	Tsutomu	Otsuki	(Laboratory of Nuclear Science)
	Tatsuo	Ido	(CYRIC)
	Masatoshi	Itoh	(CYRIC)
	Mamoru	Baba	(CYRIC)
	Ren	Iwata	(CYRIC)
	Hiroyuki	Okamura	(CYRIC)
	Tsutomu	Shinozuka	(CYRIC)
	Mashiro	Fijita	(CYRIC)

Radiation Protection and Training of Safe Handling

(Chairman)	Mamoru	Baba	(CYRIC)
	Hiroshi	Kudo	(Graduate School of Science)
	Yoshihiko	Uehara	(Graduate School of Medicine)
	Yasushi	Yamazoe	(Graduate School of Pharmaceutical Sciences)
	Keizo	Ishii	(Graduate School of Engineering)
	Toshiyasu	Yamaguchi	(Graduate School of Agricultural Science)
	Kazuhiro	Sogawa	(Graduate School of Agricultural Science)
	Masayuki	Hasegawa	(Institute for Materials Research)
	Hiroshi	Fukuda	(Institute for Development, Aging and Cancer)
	Yoshihiro	Takai	(University Hospital)
	Tatsuo	Ido	(CYRIC)
	Tsutomu	Shinozuka	(CYRIC))

Life Science

(Chairman)	Tatsuo	Ido	(CYRIC)
	Yasuhito	Itoyama	(Graduate School of Medicine)
	Kazuie	Iinuma	(Graduate School of Medicine)
	Syoki	Takahashi	(Graduate School of Medicine)
	Reizo	Shirane	(Graduate School of Medicine)
	Masahiko	Yamamoto	(Graduate School of Medicine)
	Makoto	Watanabe	(Graduate School of Dentistry)
	Sumio	Ohtuki	(Graduate School, Division of Pharmaceutical Sciences)
	Keizo	Ishii	(Graduate School of Engineering)
	Kazuo	Yamamoto	(Graduate School of Life Science)
	Hiroshi	Fukuda	(Institute for Development, Aging and Cancer)
	Junichi	Gotoh	(University Hospital)
	Shin	Maruoka	(College of Medical Sciences)
	Masatoshi	Itoh	(CYRIC)
	Ren	Iwata	(CYRIC)
	Kei-ichiro	Yamaguchi	(CYRIC)
	Yoshihito	Funaki	(CYRIC)

Prevention of Radiation Hazards

(Chairman)	Mamoru	Baba	(CYRIC)
	Osamu	Hashimoto	(Graduate School of Science)
	Tsutomu	Sekine	(Graduate School of Science)
	Keizo	Ishii	(Graduate School of Engineering)
	Tatsuo	Ido	(CYRIC)
	Tsutomu	Shinozuka	(CYRIC)
	Masashi	Koseki	(CYRIC)
	Takamoto	Miyata	(CYRIC)

XII. STAFF

XII. STAFF (as of Jan. 1, 2005)

Director Keizo Ishii

Division of Accelerator

Osamu	Hashimoto[1)]
Tsutomu	Shinozuka
Masahiro	Fujita
Takuya	Endo
Tetsu	Sonoda
Akiyoshi	Yamazaki
Eiji	Tanaka
Shizuo	Chiba[4)]
Yasuaki	Ohmiya[4)]
Naoto	Takahashi[4)]
Shigenaga	Yokokawa[4)]
Akihiko	Matsumura[4)]

Division of Instrumentations

Hiroyuki	Okamura
Toshio	Kobayashi[1)]
Hikonojo	Orihara[3)]
Atsuki	Terakawa
Sho-ichi	Watanuki
Ryuuji	Maruyama

Division of Radiopharmaceutical Chemistry

Tatsuo	Ido
Ren	Iwata
Yoshihito	Funaki
Yo-ichi	Ishikawa
Tania	Valdes-Gonzales

Hideo	Takahashi

Division of Cyclotron Nuclear Medicine

Masatoshi	Itoh
Kazuhiko	Yanai[2)]
Keiichiro	Yamaguchi
Maki	Suzuki
Kazuaki	Kumagai
Hiroomi	Sensui
Mehedi	Masud
Takehisa	Sasaki
Masayasu	Miyake
Laxmi N.	Singh
Targino RodriguesDosSantos	

Division of Radiation Protection and Safety Control

Mamoru	Baba
Takashi	Nakamura[3)]
Takamoto	Miyata
Noboru	Watanabe[5)]

Graduate Student and Researcher

Tomokazu	Suzuki	(Graduate School of Science)
Yu-ji	Miyashita	(Graduate School of Science)
Nozomi	Satoh	(Graduate School of Science)
Naoya	Sugimoto	(Graduate School of Science)
Takashi	Hasegawa	(Graduate School of Science)
Shingo	Fukushima	(Graduate School of Science)
Kimihiko	Satoh	(Graduate School, Division of Pharmaceutical Sciences)
Sabina Khond	Kar	(Graduate School, Division of Medicine)
Manami	Suzuki	(Graduate School, Division of Medicine)
Honda	Goh	(Graduate School, Division of Medicine)
Tetushi	Yamaguchi	(Graduate School, Division of Medicine)
Syunsuke	Yonai	(Graduate School of Engineering)

Md Shuza	Uddin	(Graduate School of Engineering)
Masayuki	Hagiwara	(Graduate School of Engineering)
Toshiro	Itoga	(Graduate School of Engineering)
Takeshi	Yamauchi	(Graduate School of Engineering)
Takuji	Oishi	(Graduate School of Engineering)
Takeshi	Yamauchi	(Graduate School of Engineering)
Takashi	Sasaki	(Graduate School of Engineering)
Takahiro	Makino	(Graduate School of Engineering)

Office Staff

Ryuko	Yoshida
Masashi	Koseki
Akihiro	Matsuya
Kyoko	Fujisawa
Junko	Matsuno
Fumiko	Mayama
Mitsuko	Endo
Yu-ko	Yamashita
Masakatsu	Ito
Kietu	Takahashi
Yuri	Okumura
Kimiko	Abe
Hitomi	Horigome

1) Graduate School of Science
2) Graduate School of Medicine
3) Visiting Professor
4) SUMI-JU Accelerator Service Ltd.
5) Japan Radiation Protection Co., Ltd.